Summer 2024

Efficient Modeling and Simulation for the Aerothermal Analysis of Particle-Laden Hypersonic Flows

Andrew Hinkle
Missouri University of Science and Technology

Department: Mechanical and Aerospace Engineering

Recommended Citation
Hinkle, Andrew, "Efficient Modeling and Simulation for the Aerothermal Analysis of Particle-Laden Hypersonic Flows" (2024). *Doctoral Dissertations*. 3335.
https://scholarsmine.mst.edu/doctoral_dissertations/3335

EFFICIENT MODELING AND SIMULATION FOR THE AEROTHERMAL ANALYSIS OF PARTICLE-LADEN HYPERSONIC FLOWS

by

ANDREW DALE HINKLE

A DISSERTATION

Presented to the Graduate Faculty of the

MISSOURI UNIVERSITY OF SCIENCE AND TECHNOLOGY

In Partial Fulfillment of the Requirements for the Degree

DOCTOR OF PHILOSOPHY

in

AEROSPACE ENGINEERING

May 2024

Approved by:

Dr. Serhat Hosder, Advisor
Dr. David Bayless
Dr. Daoru Han
Dr. Christopher Johnston
Dr. David Riggins
Dr. Davide Viganò

ABSTRACT

Standard approaches for simulating hypersonic flows in particle-laden environments have key limitations in practice, such as high cost and numerical noise. In this work, efficient solution strategies for particle-laden hypersonic flows were developed using both Lagrangian and Eulerian models for the particle phase with the focus on investigating spacecraft surface erosion, as well as convective and radiative heat flux augmentation due to atmospheric particulate encountered during planetary entry.

First, an efficient integration strategy for Lagrangian methods, the Trajectory Control Volume (TCV) method, was developed for steady analysis of dilute particle phase problems on general geometries. The TCV method was shown to produce accurate dust impact surface erosion distributions with three orders of magnitude fewer particle samples as compared with Monte Carlo techniques. The TCV approach also enabled the uncertainty quantification of heat-shield dust impact erosion during Mars entry with the non-intrusive polynomial chaos method. The TCV method was extended for analysis of two-way coupled problems and verified for hypersonic flow problems. Application of the technique to a Mars entry case showed that convective heat flux augmentation was insignificant.

Besides the TCV approach, a particle phase solver based on an Eulerian model was developed for hypersonic flow problems and used to predict radiation scattering properties for a Mars entry flowfield. A radiation solver based on the P_1 spherical harmonics method was used to predict radiative heat flux augmentation due to scattering, which showed little effect for nominal dust loading conditions. Additional augmentation mechanisms were shown to be insignificant for representative Mars and Titan problems.

The methods developed in this work provided valuable insight into the aerothermodynamic interactions between the gas and the particle phase for planetary entry missions and are expected to contribute to efficient analysis of particle-laden flows for general hypersonic applications in the future.

ACKNOWLEDGMENTS

I would like to express my gratitude to my advisor, Dr. Serhat Hosder, for his guidance and the opportunities he has given me. From early in my time at Missouri S&T, he has dedicated significant time and effort to my development as a student, researcher, and professional. Without his patient, committed support, I would have not reached the success I have today.

I would like to thank my committee members, Dr. David Bayless, Dr. Daoru Han, Dr. Christopher Johnston, Dr. David Riggins, and Dr. Davide Viganò for their time commitment and support of this research. I also wish to thank Dr. Christopher Johnston, and Dr. Thomas West for mentoring me at NASA Langley Research Center as an intern and fellow. Their mentoring has enriched me as an engineer.

I would like to thank Dr. Kyle Thompson, Dr. Matthew O'Connell, and the HyperSolve development team for their invaluable support, discussions, and troubleshooting efforts. I would also like to thank my fellow graduate students Mario Santos, Martin Di Stefano, and Kyle Worden for many great discussions and collaborations through the years.

I would like to acknowledge the Missouri S&T Mechanical and Aerospace Engineering department for the excellent education and oppportunities I received during my time there. Funding for this work was provided by NASA Space Technology Research Fellowship grant no. NSSC19K1150. I wish to also acknowledge the support of the NASA-Missouri Space Grant Consortium.

Finally, I want to thank my Family, friends, and wife, Anna, for their love and support which have blessed me through the years of my education. Without their support, I would not have been capable of persevering through the difficult parts of this journey.

TABLE OF CONTENTS

Page

SECTION

LIST OF ILLUSTRATIONS

LIST OF TABLES

Table Page

1. INTRODUCTION

1.1. MOTIVATION FOR THE CURRENT STUDY

Hypersonic flight in dusty environments poses numerous challenges for vehicle design. Particulates can impact vehicle surfaces at hypervelocity conditions, causing significant damage and erosion through a trajectory. In addition to surface effects, the particulate presence can couple with the gas phase and affect the flowfield similar to having a higher freestream total enthalpy. This interphase coupling can result in higher heating and shear to vehicles than a pure gas environment. In planetary entry scenarios, the particulate can further interact with the gas phase through radiation mechanisms such as emission by particle surfaces and ablation products, absorption, and scattering. The ability to model these effect in the context of entry, descent, and landing (EDL), as demonstrated in Figure 1.1, provides mission planners with the capability to margin vehicles for potential effects of particles in a physics-based manner.

A number of scenarios exist in which particle-laden hypersonic flows can occur, such as encountering ice crystals and water droplets in Earth atmospheric flight, or retropropulsive plume-surface interaction in Lunar and Mars landings. The major motivation for the current study however is entry into the Mars atmosphere during global dust storms. These global dust storms occur on a semi-regular period of approximately 5-6 earth years but can't be accurately predicted far in advance [1]. As the storms can't be planned around with certainty, it is important to understand the degree to which the high atmospheric dust content during a storm can affect a vehicle during entry to be able to design reasonable margin policies for thermal protection systems (TPS). This becomes increasingly important for future human flight missions, as excessive margins can restrict overall payload capacity. Future vehicles will have increasingly more difficult geometry to analyze, having non-axisymmetric or non-trivial shapes as is seen with the hypersonic inflatable aerodynamic decelerator (HIAD)

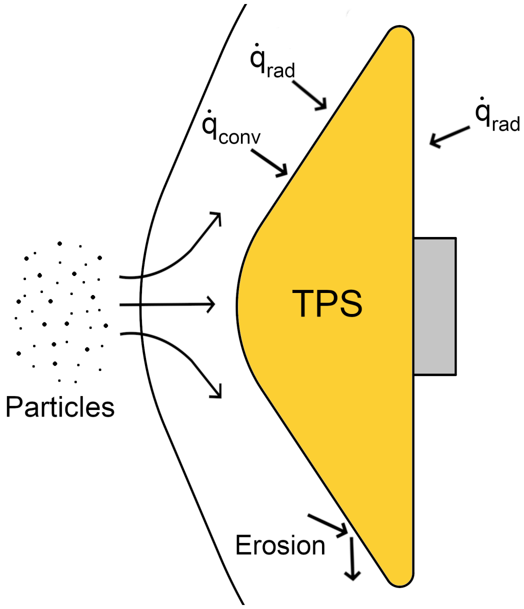

Figure 1.1. Various physical mechanisms which can affect vehicles in high speed particle-laden flow scenarios.

[2, 3] and adaptive deployable entry and placement technology (ADEPT) concepts [4, 5]. The geometry of these vehicles pose a geometric challenge that can necessitate the use of higher cost methods for analysis as will be discussed in the literature review presented in the following section. These motivations lead to the following overall goal of the current work: to advance the modeling of dusty hypersonic aerothermal environments towards efficient, production ready tools which can be utilized earlier in the design phase to account for particle effects in high energy flows. These capabilities will also provide the ability to perform uncertainty quantification and sensitivity analysis with tractible computational costs.

1.2. LITERATURE REVIEW

The literature review discusses the previous studies on particle-laden hypersonic flow modeling, covering early foundational works utilizing Lagrangian techniques, as well as a survey of more recent works which have advanced the state of the art. While the

Lagrangian approaches are discussed primarily, works using different solution methods are covered to discuss their contributions and contrast with the approach taken in the current study.

1.2.1. Early Lagrangian Modeling in Hypersonic Flowfields. Early works seeking to model high-speed particle-laden flows used various assumptions to treat the problem, as techniques which modeled large numbers of particles were intractible. Many early works sought to simulate individual particle trajectories to quantify the impact kinetic energy of particles colliding with different parts of a vehicle [6, 7]. These works primarily focused on ice crystals and rain droplets in Earth atmospheric flight scenarios, using simple approximate gas phase flowfields to evaluate drag and heating on the particles. Later studies built upon these works by utilizing high fidelity computational fluid dynamics (CFD) techniques to model the gas phase surrounding particles in hypersonic flight environments. A series of studies [8, 9] investigated the effect of Mars dust on entry vehicles using a combination of CFD gas phase solvers and Lagrangian particle simulation. They focused on TPS erosion induced by dust particle impacts [8, 9] by utilizing basic descriptions of the Martian atmospheric dust loading. These studies, despite their limited scope and modeling, established that erosion effects are more significant for aero-capture missions. It was also shown that the way in which the dust size and dust mass loading are modeled can have a significant impact on the predicted erosion augmentation. More recently, Palmer et al. [10] revisited an earlier study with improved modeling of Mars atmospheric dust loading, analyzing both dust and thermochemical erosion of a vehicle TPS over an entire planetary entry trajectory.

1.2.2. Lagrangian Models Based on Monte Carlo Techniques. The current state of the art for dusty hypersonic flow problems is the use of Monte Carlo (MC) techniques where a large number of randomly seeded particles are simulated through the flowfield [11, 12, 13]. This approach allows full surface erosion to be computed on arbitrary vehicle geometries, which removes the geometric limitations of previous works [10]. A deficiency of the MC approach is the trade-off between cost and solution quality; at low sample counts the solution exhibits noise, while smooth solutions require high cost. In practical applications where uncertainty quantification (UQ) is needed, this deficiency presents a problem as smooth solutions and subsequently high computational costs are required. In addition to surface interaction problems like TPS erosion, coupled analysis has been performed in previous studies [11]

Other works have also considered the effects of coupling between the gas and particle phases, and have shown that the presence of particles near the vehicle can alter the boundary layer characteristics, which may result in increased convective heat flux to the vehicle [11, 14]. These works compared two-way coupling, in which the effect of the particle phase on the gas is considered, with one-way coupling, in which the gas phase is solved as if no particles are present. Ching et al. [11] have also investigated the degree to which different particle drag coefficient and Nusselt number models affect coupled surface heat flux predictions, showing that specific models can have a measurable impact on the magnitude and distribution of heating over the surface.

Another aspect of EDL aerothermodynamic environments is that of radiative heating due to high temperature and ionized gases. Radiating gas environments may be augmentated due to scattering, absorption, and emission by small particles, resulting in changes to the radiative heat flux to a vehicle. A vast body of work studying the interaction of particles with radiation is available across many fields, including geophysics, astronomy, and mechanical engineering, as discussed in various texts on radiative heat transfer [15, 16]. In constrast, relatively little work is observed in hypersonic and EDL applications. One notable study considered the effect of scattering in radiative heating due to emission from high temperature particles in solid rocket plumes [17]. This work only considered emission and absorption from the particles, neglecting any interaction with the gas phase itself.

1.2.3. Alternative Solution Approaches to Lagrangian Modeling. While mixed Eulerian-Lagrangian techniques are the most commonly used approach for solving particle-laden hypersonic flow problems, other techniques are present in the literature. An early work studying the effect of a highly dust loaded flow over a flat plate on surface heating and shear stress utilized a boundary-layer solution to solve the coupled problem [18]. With this approach, a simple set of closure models for particle heating and drag, based on a constant Nusselt number and Stokes' drag, resulted in a continuum model for the particle phase which could augment a standard boundary-layer equation set and be solved with both similarity solutions and finite differencing. Wang and Glass [18] found that for high dust loading levels a significant augmentation in the surface shear and heating is observed near the leading edge region of the plate. The solutions of Wang and Glass [18] provide a high quality semi-analytical reference with which coupled analysis can be verified. A similar approach was taken by Ben-Dor and Igra [19] to study the post-shock relaxation regime of suspended particles in argon gas at high Mach numbers. The interchange of energy between the phases through convective and radiative exchange was shown to significantly affect the post-shock relaxation characteristics. Later studies by Mirzaei et al. [14], Padmapriya and Reddy [20] also utilized a continuum model for the particle phase with finite volume techniques to solve the resulting equations more generally. These works reproduced the results of Wang and Glass [18] without relying on boundary layer assumptions and demonstrated a simple but effective coupled solution approach.

While not entirely related to the regime of problems considered in this work, it is important to mention the signficant body of work which has studied the problem of retro-propulsive plume-surface-interation (PSI). This body of work includes both computational and experimental studies, with a large focus on lunar landing scenarios. Some noteable works are given here to indicate broadly where similar modeling challenges are observed. In PSI problems, the entire spectrum of particle flow regimes is observed, from dilute to densly packed fluidized beds. In the high-volume fraction regions, where the effect of the particles on the gas phase is non-negligible, volume filtering of the fluid governing equations is required. Anderson and Jackson [21] presented a volume filtered formulation of the Navier-Stokes equations, which were extended by Shallcross et al. [22] to the compressible regime.

In lunar PSI problems, another challenge is the rarefied gas regime which is present outside of the core plume region. In addition to the large range of particle phase volume fractions in the domain, the gas flow transitions from continuum in the plume core to a collisionless flow as distance from the plume increases. For problems in which detailed ejecta kinetic energy predictions are desired, the increasing rarefaction compounds the challenges associated with the particle phase modeling significantly. Morris et al. [23] models this problem using a hybrid continuum-DSMC model, utilizing an Eulerian CFD solution in the core plume and impingement region and a DSMC solution in the rest of the domain. As the gas becomes less rarefied, the CFD solution in the plume core makes the problem tractible as compared with an all-DSMC solution. Further work with DSMC and particle-laden flows is observed in the work of Gallis et al. [24], Burt and Boyd [25], in which particles are simulated in the same manner as the gas computational particles. Collisions between gas particles and solid particles are resolved directly, with the collisions being used to evaluate drag and heating effects. This makes the addition of the solid phase a natural extension of the DSMC method, and is an effective way to model rarefied gases with suspended particulates. Another application of the DSMC technique which is of great importance to this area of research is in particle scale resolved solutions of the gas flow around individual particles. This approach has been used by Loth [26], Loth et al. [27] to improve drag correlations for spheres in rarefied flows, and have found use in numerous works in this area.

1.3. OBJECTIVES OF THE CURRENT STUDY

The overall objective of the current study is to investigate computationally tractible techniques for the analysis of particle laden hypersonic flows, particularly in entry, descent, and landing (EDL) scenarios. The first sub-objective of this study is to develop tools and techniques for the analysis of surface erosion in EDL scenarios, and utilize uncertainty quantification and sensitivity analysis to identify modelling parameters which drive uncertainty in surface recession predictions. The second sub-objective of this study is to investigate the impact of particulates on aeroheating in hypersonic flows through coupling of the particle phase aerothermodynamics back to the gas phase. The last sub-objective of this study is to investigate radiation interaction in particle-laden hypersonic flows, particularly through emission and scattering by particulates.

1.4. CONTRIBUTIONS OF THIS DISSERTATION

The current study has resulted in a series of contributions to the state-of-the-art, which are outlined here:

- An efficient direct solution approach, the trajectory control volume (TCV) method was developed for the solution of surface erosion due to particle impacts in planetary entry scenarios. The TCV method was applied to dust-induced TPS erosion in Mars entry during a global dust storm condition, resulting in the first full TPS surface erosion solutions on general vehicles at angle of attack. In addition, the TCV method produced noise-free solutions with more than 3 orders of magnitude reduction in simulated particles as compared with a reference Monte Carlo technique.

- The smooth solutions produced by the TCV method made it possible to apply efficient uncertainty quantification and nonlinear global sensitivity analysis to dust-induced TPS erosion solutions. A first-of-its-kind UQ analysis was performed on dust-induced surface erosion in Mars entry using a UQ framework based on Point-Collocation Non-intrusive Polynomial Chaos. The analysis, which was previously infeasible, was used to identify key modeling parameters which affect surface erosion solutions, and rank their contributions.

- The TCV method was extended to enable two-way coupled analysis with a CFD gas-phase solver. Coupled analysis allows the simulation of scenarios in which the back-coupling of momentum and energy exchange to the surrounding gas results in augmentation to the gas phase solution. The technique was applied to a series of verification and validation cases involving the augmentation of surface heat flux due to particle presence, and was shown to provide high-quality solutions at a similar cost reduction as observed in surface erosion problems. The two-way coupled analysis was applied to a dusty Mars entry scenario, demonstrating that the effect is minimal near the peak heating point in a trajectory.

- A continuum particle phase solver was developed for hypersonic vehicle problems involving large wake regions and verified against a Lagrangian solver and the TCV method. The continuum solver was used to produce high-quality particle phase solutions enabling the analysis of radiation interactions involving blackbody radiation and scattering by particulates.

- A radiation transport solver based on the P_1 spherical-harmonics approximation was developed for use with the NASA HARA radiation code, in order to study the interaction between particles and high temperature shock-layer radiation via scattering. The combined continuum particle solver and radiation transport solver suite was applied to EDL scenarios relevant to Mars entry during global dust storms, where it was found that scattering is not likely to affect radiative heat flux significantly under extreme dust loading conditions.

1.5. OUTLINE OF THE DISSERTATION

The remainder of the dissertation is structured as follows: Section 2 provides an overview of the first of two techniques for particle-laden hypersonic flow, the Lagrangian technique, starting with the Lagrangian governing equations and closure models for dilute particle phases in hypersonic environments, as well as solution techniques for individual particle simulation and Monte Carlo techniques for multi-particle scenarios. In Section 3 the TCV method, an efficient direct solution approach for particle-laden hypersonic flows, is presented for both one-way and two-way coupled analysis using the Lagrangian technique. Section 4 presents the second technique used in the current work, the Eulerian technique, starting with the Eulerian form of the particle phase governing equations, and discusses their equivalence with the Lagrangian form. A solution approach for solving the continuum particle phase PDE system and verification against the Lagrangian approach are presented. In Section 5, the radiative transport equation (RTE) and particle-radiation interaction mechanisms like scattering are discussed. Solution techniques for both non-scattering and scattering forms of the RTE are presented. Section 6 presents the results of the study, broken into three sections. In section 6.1, the TCV method is applied to surface erosion prediction in Mars EDL during a global dust storm, presenting for the first time full TPS surface erosion solution, uncertainty quantification, and nonlinear global sensitivity analysis of such a scenario. Section 6.2 presents the extension of the TCV method to coupled analysis and application of the technique to efficient prediction of surface heating augmentation in dusty high speed flows. Section 6.3 presents an analysis of radiation interaction between particles and high-temperature shock layers in planetary entry flows, with applications to Mars and Titan. Lastly, overall conclusions of the study and the future work are given in Section 7.

2. DILUTE PARTICLE PHASE MODELING IN HYPERSONIC FLIGHT

One of the primary computational techniques used in this work is the mixed Eulerian-Lagrangian modeling approach, where the gas phase is modeled with a traditional Eulerian CFD solver, and the particle phase is treated as a collection of Lagrangian point masses. This section discusses the basic mechanisms necessary to perform Lagrangian particle solutions on a CFD background solution, starting with an overview of the governing equations and closure models used. Next, the mechanics of one-way coupling of the gas phase solution to the particle phase is discussed, including sampling a piecewise continuous CFD solution, time integration of the particle governing equations, and a simple verification problem for the methodology. Lastly, two-way coupling of the gas and particle phases is discussed, with some discussion of the application of Monte Carlo (MC) techniques to the computation of sources terms.

2.1. LAGRANGIAN DESCRIPTION OF THE PARTICLE PHASE

The Lagrangian modeling approach used in this work and much of the literature seeks to simplify the modeling of the motion and physical interaction of particles. In reality, the flow around a particle is complex, and like in direct numerical simulation (DNS) of turbulence, the difference in scale between the overall problem domain and the particle surface is far too large to perform scale-resolved simulations directly in most cases. For realistic problems, with cell sizes much larger than the particle diameter, the assumption is made that the effect on the surrounding gas is small. The particle is then assumed to be a point mass, with governing equations derived around the evolution of the momentum, energy and mass of the point-particle. This simplification, when supplemented with appropriate closure models, results in a tractible overall solution process which can be applied to a

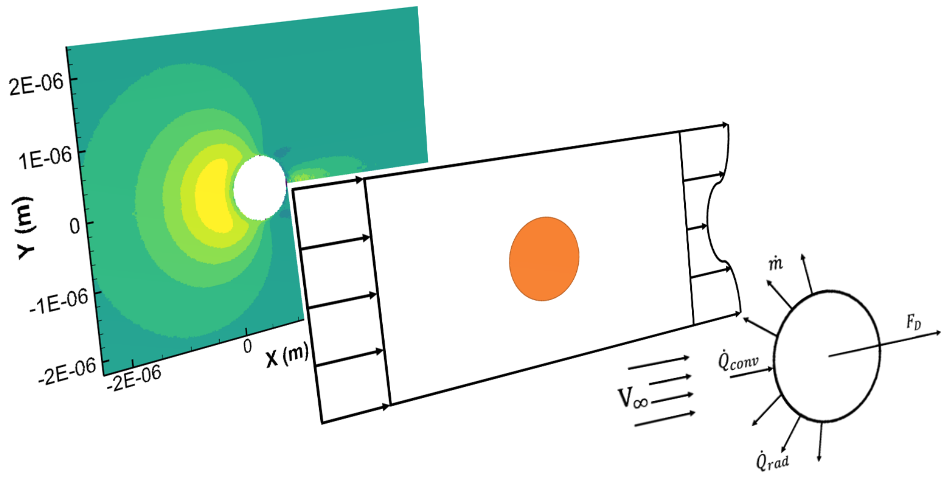

Figure 2.1. Lagrangian particle modeling trades the full detail of the flow around a particle for correlations describing the various forces and exchanges with the surrounding gas, such as the convective and radiative heat fluxes.

large number of computational particles. The introduction of physical closure models for the surrounding gas effect on a particle's drag, heating, and mass change result in the approximation of the complex flowfield as a simple point quantity as shown in Figure 2.1.

2.1.1. Particle Governing Equations. The most important governing equation for a particle is that of it's translational motion. This governing equation is derived by applying Newton's law of motion to a particle with a mass, m_p, velocity, $\vec{u}_p$, and force applied, $\vec{F}_p$:

$$\frac{d}{dt}\left(m_p\vec{u}_p\right) = \vec{F}_p. \tag{2.1}$$

For a simple point mass with known forces, this expression is exact. In practice, when determining the forces on particle using closure models, some error and uncertainty is introduced due to the assumptions made in the respective force models. For non-vaporizing/ablating particles or particles in which the mass loss rate is quite small, a simplification is often made. The product rule is applied to Eqn. (2.1), and the mass exchange rate, $\frac{d}{dt}(m_p)$ is assumed small:

$$\frac{d}{dt}\left(m_p\vec{u}_p\right) = \cancelto{0}{\frac{dm_p}{dt}}\vec{u}_p + m_p\frac{d\vec{u}_p}{dt} = \vec{F}_p, \tag{2.2}$$

resulting in the simple constant mass expression:

$$m_p\frac{d}{dt}\left(\vec{u}_p\right) = \vec{F}_p. \tag{2.3}$$

Equation (2.1) represents the conservative form of the governing equation of a particle's momentum, while Eqn. (2.3) represents the non-conservative form. The difference in this governing equation is small, but the choice of conservative or non-conservative formulation impacts other governing equations significantly. This is similar to the choice of primitive or conservative variables in CFD, in which the choice affects the form of the governing equations, and can impact the solution depending on the flight regime [28]. The primitive formulation is commonly used in the literature, such as in the work of Palmer et al. [10] and others. The conservative formulation however is much less commonly used. An example of its use is given by Davuluri et al. [29], where it is applied to spalled TPS particles in a vehicle forebody shock layer.

Next, the thermal energy of the particle is considered. In a conservative formulation, the total energy of the particle, E_p, is considered as the variable, with the first law of thermodynamics being applied:

$$\frac{d}{dt}\left(E_p\right) = \dot{Q}_p + \dot{W}_p = \dot{Q}_p + \vec{u}_p \cdot \vec{F}_p, \tag{2.4}$$

where Q_p is the thermal energy exchanged at the particle's surface, and W_p is the work applied to the particle. The total energy can be decomposed into the internal energy, e_p, and the kinetic energy:

$$E_p = e_p + \frac{1}{2}m_p\left|\vec{u}_p\right|^2. \tag{2.5}$$

Again, these expressions are exact for a point mass problem. An assumption is introduced in order to represent the internal energy as a function of a single particle temperature, T_p. Assuming no spatial variation of temperature within the particle, and a constant specific heat, the following expression for the internal energy is written:

$$e_p = m_p c_p T_p. \tag{2.6}$$

For a nonconservative system in which the temperature is tracked, a governing equation is derived by balancing the time derivative of the thermal energy with the heating rate to the particle. Again, assuming a small mass change rate, the following expression is obtained:

$$\frac{de_p}{dt} = m_p c_p \frac{dT_p}{dt} = \dot{Q}_p. \tag{2.7}$$

The change in mass of the particle is trivial for a conservative system, where the rate of change of mass is simply balanced by the vaporization rate:

$$\frac{dm_p}{dt} = \dot{m}. \tag{2.8}$$

For a non-conservative system however, the derivation is more complicated as the particle radius is the typical state variable. First, the mass is assumed to be a function of the radius of a sphere with constant density, ρ_m:

$$m_p = \frac{4}{3}\pi\rho_m r_p^3. \tag{2.9}$$

Taking the time derivative of the mass and using the chain rule, the following is obtained as discussed by Palmer et al. [10]:

$$\frac{dm_p}{dt} = \frac{4}{3}\pi\rho_m \frac{dr_p^3}{dr}\frac{dr}{dt} = 4\pi\rho_m r_p^2 \frac{dr_p}{dt}. \tag{2.10}$$

Substituting Eqn. (2.9) in to Eqn. (2.10) and rearranging yields an expression for the change in radius of a spherical particle given a mass-loss rate:

$$\frac{dr_p}{dt} = \frac{\dot{m}}{4\pi\rho_m r_p^2}. \tag{2.11}$$

Lastly, the rate of change in the particle's position is equal to its velocity vector:

$$\frac{d\vec{x}_p}{dt} = \vec{u}_p. \tag{2.12}$$

2.1.2. Summary of Lagrangian Particle Governing Equations. Here the conservative and primitive formulations of the governing equations are summarized in vector form for clarity. Denoting the vector of conserved variables as $\mathbf{U}_{\text{cons}}$, the conservative formulation takes the following form:

$$\frac{d}{dt}\mathbf{U}_{\text{cons}} = \begin{bmatrix} \vec{u}_p \\ \dot{m}_p \\ \vec{F}_p \\ \dot{Q} + \vec{u}_p \cdot \vec{F}_p \end{bmatrix}, \tag{2.13}$$

where $\mathbf{U}_{\text{cons}}$ is defined as:

$$\mathbf{U}_{\text{cons}} = \begin{bmatrix} \vec{x}_p & m_p & m_p\vec{u}_p & E_p \end{bmatrix}. \tag{2.14}$$

Similarly, the nonconservative formulation is given as follows:

$$\frac{d}{dt}\mathbf{U}_{\text{prim}} = \begin{bmatrix} \vec{u}_p \\ \frac{\dot{m}}{4\pi\rho_m r_p^2} \\ \frac{\vec{F}_p}{m_p} \\ \frac{\dot{Q}_p}{m_p c_p} \end{bmatrix}, \tag{2.15}$$

where the vector of primative variables, $\mathbf{U}_{\text{prim}}$, is defined as:

$$\mathbf{U}_{\text{prim}} = \begin{bmatrix} \vec{x}_p & r_p & \vec{x}_p & T_p \end{bmatrix}. \tag{2.16}$$

2.2. PHYSICAL CLOSURE MODELS FOR HYPERSONIC PROBLEMS

In this section, the physical closure models that specify the generic terms in the governing equations in the last section are presented and discussed. Specifically, the mass-exchange rate, $\dot{m}$, forces, $\vec{F}_p$, and heating rate to the particle, $\dot{Q}$, are given. As this work is concerned with dilute particle-laden flows in the hypersonic regime, some mechanisms which are important for low-speed particle flows or fluidized beds are neglected and may not be discussed here.

2.2.1. Drag Modeling. The forces on a particle, $\vec{F}_p$ in Eqns. (2.1-2.3), is simply the integral of the pressure and shear over the particle surface. With a resolved flowfield this can be computed directly, but for a Lagrangian particle insufficient flowfield detail is available to do this. Instead, the force is typically divided into a series of forces which can be computed using correlations or other reduced order models based on the particle and surrounding gas state. Commonly, particle forces are subdivided into the following:

$$\vec{F}_p = \vec{F}_{\text{qs}} + \vec{F}_{\text{M}} + \vec{F}_{\text{thermo}} + \vec{F}_{\text{us}}, \tag{2.17}$$

where the terms are respectively the quasi-steady drag, $\vec{F}_{\text{qs}}$, Magnus force, $\vec{F}_{\text{M}}$, thermophoretic force, $\vec{F}_{\text{thermo}}$, and unsteady drag effects, $\vec{F}_{\text{us}}$. The quasi-steady drag is the most commonly referred to term in this set, and is typically all that is modeled in hypersonic particle trajectories. This drag is the drag a particle would experience if the surrounding gas conditions were held constant and no transients were present in the solution. The Magnus force is the force on a particle which has both rotational and translational velocities, in which a differential pressure arises normal to the axis of rotation. Thermophoretic force is a force which arises due to a differential temperature on each side of a particle [26]. For hypersonic cases, the magnus force is small relative to the quasi-steady drag, and is therefore neglected in this work. For scenarios in which inter-particle collision is modeled, the magnus force can have a larger impact due to rotational velocities imparted by contact with other particles.

In the current work, only the quasi-steady drag force is considered. A variety of models exist which correlate quasi-steady drag with quantities like Mach number, Reynolds number, and the ratio of specific heats, γ. Capecelatro [30] summarizes a collection of quasi-steady drag models along with the range of validity for various conditions. In the current work the particle phase is in the dilute regime in which the volume fraction of particles is negligibly small. The most commonly used model in this regime is that of Henderson [31], with the models of Loth [26, 27] finding more common use recently. Each of these models incorporate non-continuum flow effects on the particle drag, which is critical for many particle-laden hypersonic flow problems. The quasi-steady drag force vector assuming a drag coefficient, C_D, is given is defined as follows:

$$\vec{F} = \frac{\pi}{2}\rho_g r_p^2 C_D \left\|\Delta\vec{v}\right\| \left(\vec{u}_g - \vec{u}_p\right). \tag{2.18}$$

In the current work, unless otherwise noted, the model of Henderson [31] is used with the subsonic modification presented by Majid et al. [32] to compute the quasi-steady drag coefficient of particles. This formulation alters the subsonic portion of the correlation to remove a singularity which occurs at zero relative velocity to the flow, improving its numerical stability for particles which equilibrate with the gas phase. The general form of the correlation is:

$$C_D = \begin{cases} C_D^1 & M \leq 1 \\ C_D^{12} & 1 < M \leq 1.75 \\ C_D^2 & 1.75 < M \end{cases} \tag{2.19}$$

where M is the relative Mach number of the particle with respect to the local gas velocity, C_D^1 is the subsonic portion of the model, C_D^2 is the supersonic portion of the model, and C_D^{12} is a transition region given by the following linear interpolation between C_D^1 and C_D^2 evaluated at their bounding Mach numbers:

$$C_D^{12}\left(Re_p, M, \frac{T_p}{T_g}\right) = C_D^1\left(Re_p, 1, \frac{T_p}{T_g}\right) + \frac{4}{3}(M-1)\left(C_D^2\left(Re_p, 1.75, \frac{T_p}{T_g}\right) - C_D^1\left(Re, 1, \frac{T_p}{T_g}\right)\right), \tag{2.20}$$

where Re_p is the Reynolds number of the gas flow around the particle defined by the particle diameter, d_p, gas density and viscosity, ρ_g and μ_g, and relative velocity magnitude between the gas and particle:

$$Re_p = \frac{\rho_g \left\|\Delta\vec{v}\right\| d_p}{\mu_g}. \tag{2.21}$$

The subsonic region is modeled as follows:

$$C_D^1 \left\|\Delta\vec{v}_p\right\| = 24/A + (B + C)\left\|\Delta\vec{v}_p\right\|, \tag{2.22}$$

where the terms A, B, and C are given as follows (subscripts denoting gas phase properties are dropped for brevity) [32]:

$$A = \frac{2\rho r_p}{\mu} + \frac{\sqrt{\gamma/2}}{a}\left\{4.33 + \frac{3.65 - 1.53T_p/T}{1 + 0.353T_p/T}\exp\left[-0.247\frac{2r_p\rho a}{\mu\sqrt{\gamma/2}}\right]\right\} \tag{2.23}$$

$$B = \exp\left[-0.5\frac{\sqrt{\mu\left\|\Delta\vec{v}_p\right\| 2r_p\rho}}{a}\right]\left(0.1M^2 + 0.2M^8 + \frac{4.5 + 0.38\left(0.03Re + 0.48\sqrt{Re_p}\right)}{1 + 0.03Re_p + 0.048\sqrt{Re_p}}\right) \tag{2.24}$$

$$C = 0.6M\sqrt{\gamma/2}\left[1 - \exp\left(\frac{-\mu}{2a\rho r_p}\right)\right], \tag{2.25}$$

where a is the local frozen speed of sound and γ is the frozen ratio of specific heats. The supersonic portion of the model is given as follows:

$$C_D^2 = \frac{0.9 + \frac{0.34}{M^2} + 1.86\sqrt{\frac{M}{Re_p}}\left[2 + \frac{1.058}{M}\sqrt{\frac{2T_p}{T\gamma}} + \frac{4}{M^2\gamma} - \frac{4}{M^4\gamma^2}\right]}{1 + 1.86\sqrt{\frac{M}{Re_p}}} \tag{2.26}$$

2.2.2. Heat Transfer Modeling. The Nusselt number, Nu, is used to model the heat flux to the particle as a function of temperature difference with the surrounding gas. In this work, the heating correlation of Fox et al. [33] is used following discussion in Ref. [10] where various models are compared:

$$Nu = \frac{2}{1 + 17\frac{M}{Re}}\exp(-M) + 0.459Re^{0.55}Pr^{0.333}\left[\frac{2 + \exp\left(-17\frac{M}{Re}\right)}{3}\right], \tag{2.27}$$

where Pr is the Prandtl number of the gas:

$$Pr = \frac{\mu_g c_{P_g}}{\kappa_g}. \tag{2.28}$$

The Nusselt number is then used to compute the heat rate to the particle based on the gas thermal conductivity, κ_g, and temperature difference between the gas and particle [29]:

$$\dot{Q} = \frac{Nu A_s}{d_p}\left[\kappa_{tr}\left(T_{tr} - T_p\right) + \kappa_{ve}\left(T_{ve} - T_p\right)\right], \tag{2.29}$$

where A_s is the surface area of the particle, and d_p is the diameter of the particle. Equation (2.29) is valid for a two-temperature thermal nonequilibrium model [34], where the a separate temperature tracks the translational-rotational energy modes, T_{tr}, and a second models the vibrational-electronic energy modes, T_{ve}. The thermal conductivities, κ_{tr}, and κ_{ve}, represent the contribution from the translational-rotational and vibrational-electronic modes respectively.

2.2.3. Vaporization Modeling. In this work, a simple approach for modeling the ablation of the particle is used similarly to previous studies [10, 35], which assumes that all heat flux to the particle past a vaporization temperature results in mass loss rather than temperature increase.

$$\dot{m} = -\frac{\dot{Q}}{\zeta} \tag{2.30}$$

where ζ is the latent heat of vaporization for the particle material. Based on the discussion in [10], the vaporization temperature model of Schaefer and Fegley [36] is used:

$$T_{vapor} = 270\log_{10}(P) + 3181, K \tag{2.31}$$

where P is the pressure on the particle surface in units of *bar*.

As simply applying this model with a step function results in a discontinuity in the mass and energy governing equations, it is necessary to either include an event location approach in the time integration scheme or utilize a smooth approximation of the step function. Purely integrating the governing equations with a forward Euler scheme results in unphysical overshoots and oscillations in the particle temperature after reaching the vaporization temperature. In this work the right hand side of the governing equations is smoothed using the following sigmoid function:

$$f(T) = \left\{1 + \exp\left[\frac{14\left(T_{\text{vapor}} - T\right)}{dT}\right]\right\}^{-1}, \tag{2.32}$$

where dT is the interval over which the smooth stepping happens. As the function uses an exponential, it never reaches 0 or 1 exactly. The value of 14 causes f to have the values of approximately 0.9991 and 0.0009 at temperatures of $T_{\text{vapor}} - dT/2$ and $T_{\text{vapor}} + dT/2$ respectively. A dT value of 20 was found to be adequate for the problems examined in this work. The resulting vaporization model is implemented by multiplying the heat flux, $\dot{Q}$, and mass loss, $\dot{m}$, in Eqs. (2.13) and (2.15) by $f(T_p)$ and $(1 - f(T_p))$ respectively. This has the effect of smoothly ‘switching off’ the model at temperatures lower than the vaporization temperature, such that the resulting governing equations do not have a discontinuity at this temperature, which causes ringing of the particle temperature along the trajectory.

2.3. SOLUTION OF THE PARTICLE GOVERNING EQUATIONS

This section describes the overall solution process of the previously described particle governing equations. First, the gas phase solution sampling process is described, including the cell determination and interpolation steps. Then, the time integration scheme and time step sizing is presented.

2.3.1. Gas Phase Solution Sampling. As mentioned in the literature review, early works used approximate gas phase properties for the shock-layer [6, 7] which were simple to evaluate. Recent studies, however, use high-fidelity CFD solutions, which are generally piecewise continuous polynomial solutions. With the large number of cells in a gas phase solution, the evaluation of this piecewise solution can be complicated and expensive to perform. The first difficulty in sampling the solution is in the determination of the cell to sample from. In one-dimensional piecewise continuous solution evaluation, such as a cubic spline, it is a trivial task to find the interval containing the sampling point. This is not the case in a two or three-dimensional domain however, except in the simplest case of regular cartesian grids. For the most common case of irregular grids, this cell determination process requires a more involved algorithm to test whether a point is inside a given cell. Various algorithms were investigated, with varying levels of robustness observed on typical grids for hypersonic problems. One such algorithm was based on the point-in-polyhedra test proposed by Lane et al. [37]. The test of Lane et al. [37] compares the signed solid angle swept by each face of the polyhedra and the point in question with 4π. Points inside the cell will have a swept solid angle equal to 4π, while points outside the cell will have less. This algorithm was found to low cost, but not completely robust in extremely high aspect ratio cells near vehicle surfaces on structured grids.

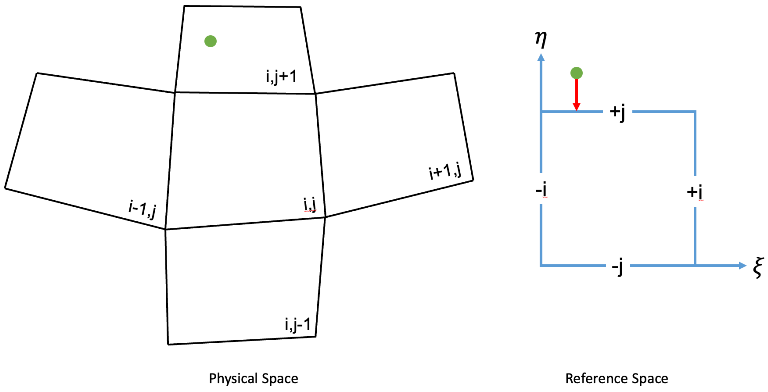

Physical Space

Reference Space

Figure 2.2. Example of cell determination using reference cell mapping.

The method which was found to be robust and efficient is a mapping approach with a similar cell neighbor traversal to the ray tracing approach. In the mapping approach, a cell is tested for containing the unknown point by transforming the cell vertices to a reference cell, and using the mapping to perform the same transformation to the unknown point. In this reference space the particle can be trivially tested against the bounds of the reference cell. The result of this test is then used to determine the closest cell face and associated face neighbor for the next test. Repeating this as in the ray-tracing approach allows for walking from a starting cell to the containing cell efficiently. Like the ray-tracing approach, this method doesn't become more expensive for large meshes. The robustness of the method in boundary-layer cells is much higher however, making the approach well suited for hypersonic problems. Ths approach is similar to the search-locate approach of Allievi and Bermejo [38]. An example of this approach is shown in Figure 2.2. Next, the reference cell mapping used in this work is presented.

In the current work structured-grids were the only type of mesh used, so the only mapping needed was for hexahedra. The trilinear interpolation technique presented by Yoder [39] was used for this purpose, which is summarized here. For trilinear interpolation, a linear interpolant is made for each reference axis at the 8 corners of the hexahedron. The product of these interpolants forms a shape function for each of the corners. A function of the corner point physical coordinates is defined such that when the parameterized coordinates, a, b, and g, are correctly located the root of the function is found. Newton's method is then used to find the parameterized coordinates. As the parameterized coordinates have values of ± 1 at each corner, the point-in-cell test is performed by simply taking the absolute value of each a, b, and g value, and comparing with one. If any is greater than one, then the point is not in the cell. If the point is not in the cell, the parameterized coordinate with the largest value is used to select the next search cell. For example, if the largest value was a, the new i index of the mesh is taken to be:

$$i_{\text{new}} = i_{\text{current}} + \text{sign}(a). \tag{2.33}$$

The b and g values map to the j and k directions, respectively. Following this process with the search-locate procedure mentioned before, a containing cell can be found if the point is within the domain. With the cell containing the particle found, the solution can then be sampled. The simplest approach is to use the cell average value, particularly when the solver produces cell centered data, though in practice using the same basis as the flow solver is the best option. For second order solvers, a linear basis is simple and effective. In the current work a structured second order finite volume solver is used to predict the gas phase, so a trilinear interpolation approach is used. As the trilinear mapping is used to find the parameterized coordinates within the containing cell, the values are re-used to evaluate the interpolation function as described by Yoder [39]:

$$f(\vec{x}) = \sum_{i=1}^{8} \phi_i(\vec{x}) f_i, \tag{2.34}$$

where $\phi(\vec{x})$ are the trilinear basis functions. These basis functions are as follows [39]:

$$\phi_1(\vec{x}) = (1 - g(\vec{x}))(1 - b(\vec{x}))(1 - a(\vec{x})) \tag{2.35a}$$

$$\phi_2(\vec{x}) = (1 - g(\vec{x}))(1 - b(\vec{x}))(1 + a(\vec{x})) \tag{2.35b}$$

$$\phi_3(\vec{x}) = (1 - g(\vec{x}))(1 + b(\vec{x}))(1 - a(\vec{x})) \tag{2.35c}$$

$$\phi_4(\vec{x}) = (1 - g(\vec{x}))(1 + b(\vec{x}))(1 + a(\vec{x})) \tag{2.35d}$$

$$\phi_5(\vec{x}) = (1 + g(\vec{x}))(1 - b(\vec{x}))(1 - a(\vec{x})) \tag{2.35e}$$

$$\phi_6(\vec{x}) = (1 + g(\vec{x}))(1 - b(\vec{x}))(1 + a(\vec{x})) \tag{2.35f}$$

$$\phi_7(\vec{x}) = (1 + g(\vec{x}))(1 + b(\vec{x}))(1 - a(\vec{x})) \tag{2.35g}$$

$$\phi_8(\vec{x}) = (1 + g(\vec{x}))(1 + b(\vec{x}))(1 + a(\vec{x})), \tag{2.35h}$$

where a, b, and g are the parameter space coodinates of the trilinear mapping from before. The approach is also applicable to Lagrangian basis functions used in discontinuous Galerkin (DG) solvers, with the mapping used for the discretization being used for cell determination and solution sampling, as described by Ching et al. [40]. An alternative solution not explored here is to reconstruct the solution using a radial basis function or polynomial least squares interpolant. With such an approach, cell determination becomes less important, though the determination of the interpolation stencil may be more complicated and costly than the approaches discussed here for structured-grid solutions. The resulting gas phase solution primitives interpolated to the particle location are used to evaluate the closure models and governing equations.

2.3.2. Time Integration. With the governing equations evaluated by sampling the gas phase solution at the particle location, the next step is to discretize and solve the governing equations, Eqns. (2.13) or (2.15), in time. In this work, integration of Eqns. (2.13) or (2.15) in time is achieved with the forward Euler method:

$$\mathbf{U}^{n+1} = \mathbf{U}^{n} + \left.\frac{\partial \mathbf{U}}{\partial t}\right|_{t=t_n} \Delta t, \tag{2.36}$$

where the state vector, $\mathbf{U} = [\, x_p \; y_p \; z_p \; u_p \; v_p \; w_p \; T_p \; r_p \,]^T$, is advanced from time t_n to t_{n+1}. For high speed cases, where particle velocity generally does not equilibrate fully with the gas phase, Euler explicit integration is generally sufficient. Implicit methods may provide better solution stability when this isn't the case. For some scenarios, higher order schemes such as Runge-Kutta or Adams-Bashforth methods may result in overall lower cost due to larger timestep limits, but add complexity to the overall solution process. Sizing of the timestep, Δt, is important to ensure stability of the integration scheme, as well as to enforce that the particles do not skip any grid cells along their trajectories. For stability, the timestep is chosen to be smaller than the particle momentum relaxation time:

$$\Delta t \leq \tau_m. \tag{2.37}$$

Following discussion in Ching et al. [40], the momentum relaxation time is:

$$\tau_m = \frac{16\rho_m r_p^2}{3C_D Re_p \mu_g}. \tag{2.38}$$

Assuming the drag coefficient to be $24/Re_p$, as in Stokes' solution of drag on a spherical particle, the momentum relaxation time is [40]:

$$\tau_m = \frac{2\rho_m r_p^2}{9\mu_g}. \tag{2.39}$$

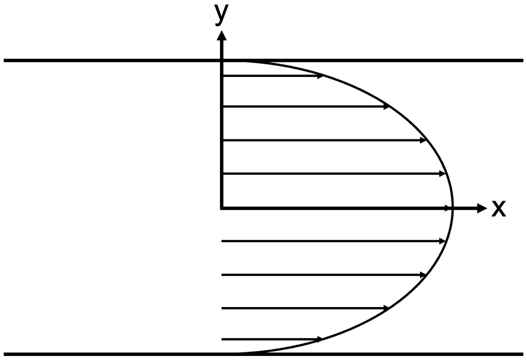

Figure 2.3. Poiseuille flow diagram.

Using the actual drag coefficient of the particle would provide a better estimate of the stability limit, but in practice this relaxation time provides a suitable timestep reference when multiplied by a factor less than 1. A factor of 50% was found to be sufficient in the current work.

2.3.3. Verification of Lagrangian Particle Tracing Methodology. To verify that the basic Lagrangian solution process is implemented correctly, a simple case in which an analytical solution can be computed was compared with the current approach. For this case the gas phase was described by Poiseuille flow, which is pressure-driven flow between parallel plates as shown in Figure 2.3. The fully developed flow profile is described by the x-direction velocity given as a function of the y coordinate:

$$u_g(y) = \frac{1}{4\mu}\left(-\frac{dp}{dx}\right)\left(h^2 - y^2\right), \tag{2.40}$$

where h is half the spacing between the plates, and $\frac{dp}{dx}$ is the pressure gradient in the flow direction. To verify the current approach, a structured grid of dimensions 250 by 50 cells was associated with a field having an x-velocity defined by Eqn. (2.40) at each grid point. A single particle was seeded within the channel with initial position and velocity as defined in Table 2.1. The conditions are consistent with the verification case demonstrated by Ching et al. [40].

Table 2.1. Conditions for the particle tracing verification case of Ching et al. [11].

μ (Pa·s)	$\frac{dp}{dx}$ (Pa/m)	h (m)	τ_m (s)	$\vec{x}_p^i$ (m)	$\vec{u}_p^i$ (m/s)
10^{-4}	-8 x 10^{-4}	1	1	$[0.45, 0.35]$	$[0, 0.2]$

The particle drag model for this case is modeled with Stoke's drag formula:

$$C_D = \frac{24}{Re_p}, \tag{2.41}$$

where the particle Reynolds number is described by Eqn. (2.21). Substituting Eqn. (2.41) into Eqn. (2.15) and simplifying admits the following ODEs which can be solved analytically to compute the particle position and velocity at a given time, t:

$$\frac{d}{dt}\left(\begin{bmatrix} \vec{x}_p \\ u_p \\ v_p \end{bmatrix}\right) = \begin{bmatrix} \vec{u}_p \\ \frac{u_g(y_p)-u_p}{\tau_m} \\ \frac{-v_p}{\tau_m} \end{bmatrix}. \tag{2.42}$$

The term τ_m refers to the particle momentum relaxation time scale, which for a drag coefficient defined by Eqn. (2.41) is defined as:

$$\tau_m = \frac{2\rho_m r_p^2}{9\mu_g}. \tag{2.43}$$

In Eqn. (2.43), ρ_m refers to the particle material density, and μ_g is the gas phase thermal conductivity. The current modeling approach is compared with the analytical result of Eqn. (2.42) in Figure 2.4. The comparison shows that the current gas-phase sampling and solution process is able to accurately solve the particle governing equations on a discrete mesh and solution.

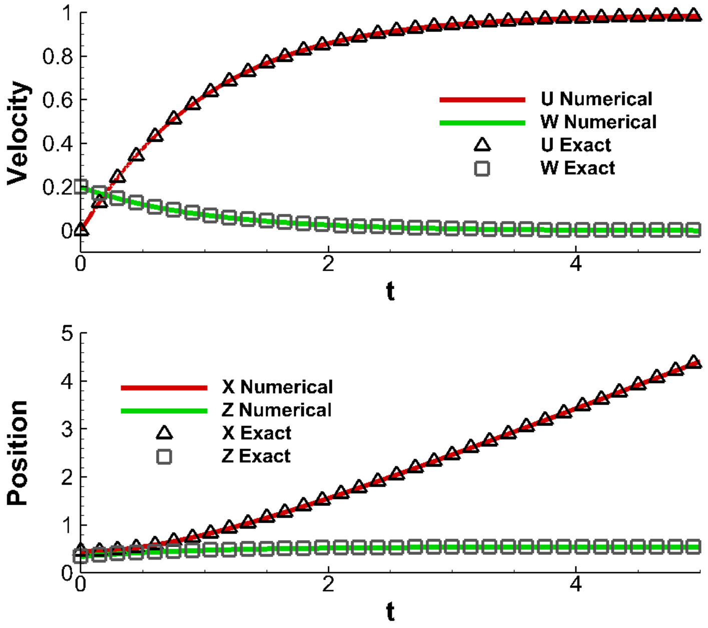

Figure 2.4. Verification of basic Lagrangian solution process.

3. THE TRAJECTORY CONTROL VOLUME METHOD

In nearly every hypersonic particle-laden flow problem, the effect of a large number of particles is desired. As discussed in the literature review, the most common technique for predicting the aggregate effect of a large number of particles is the MC technique, in which a large number of computational particles are simulated within the domain after being introduced randomly at the inflow. While the technique is simple to implement and is highly flexible, it has two key drawbacks. The first is that the results of a MC solution are inherently noisy, which can be seen in surface erosion predictions in the literature [11, 12]. Noisy solutions are not necessarily an issue in every context, but analysis which relies on smooth solutions will be difficult, such as uncertainty quantification techniques which utilize surrogate models for efficient uncertainty propagation through the model [41]. The second drawback of MC methods is the high computational cost, which is linked to the noise issue. As the noise in an MC solution is reduced by increasing the number of samples, the cost is directly linked to the level of noise required. As will be shown in Ch. 6, the sample count required for nearly noise-free surface erosion predictions can be quite high.

The drawbacks of the MC method motivate the use of solution techniques which can give smooth results at a lower cost with desired accuracy, so that analyses like uncertainty quantification can be performed without numerical issues related to noisy data. In this section, the TCV method, which utilizes particle trajectory information to efficiently infer the aggregate effects of a dilute particle phase in a hypersonic environment, will be presented. The TCV method can be viewed as a generalization of the 2D capture area technique presented by Ruff and Berkowitz [42] for airfoil icing problems. Figure 3.1 demonstrates the key difference between the MC and TCV techniques. The foundations and assumptions of the technique, methodology, and extension to two-way coupled analysis will be discussed.

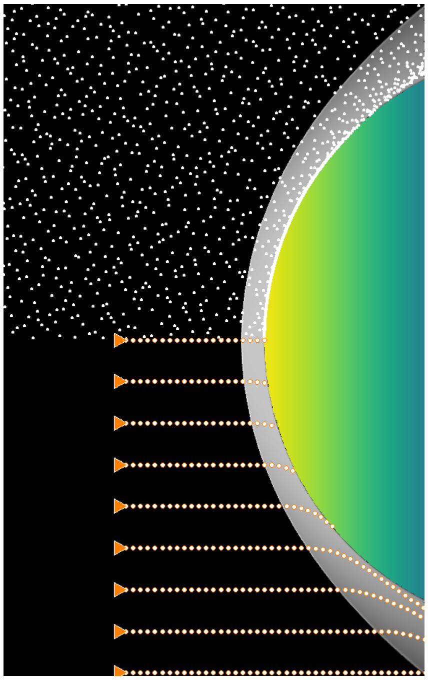

Figure 3.1. Diagram of solution processes for Monte Carlo (MC), top, and Trajectory Control Volume (TCV) method, bottom, showing the reduction in particle samples required for smooth solutions with TCV by reconstructing the surface impact rate using a sparse set of particle trajectories.

3.1. THEORETICAL FOUNDATIONS AND ASSUMPTIONS

The TCV method is formulated by tracking specific particles through the solution domain, and then using their trajectories to form a 'logical' grid upon which the problem is solved. This logical grid is separate from the physical grid used to solve the gas phase, and varies as the particle trajectories vary. For a well behaved problem like dust erosion of a vehicle TPS in the Mars atmosphere, the steady-state trajectories of individual particles vary smoothly with the starting location and size, generally resulting in a 1-to-1 mapping between upstream location and downstream/impact location for a constant initial particle size. Problems in which a polydisperse particle phase is modeled can be treated by solving each initial particle size separately and integrating over a size distribution, which will

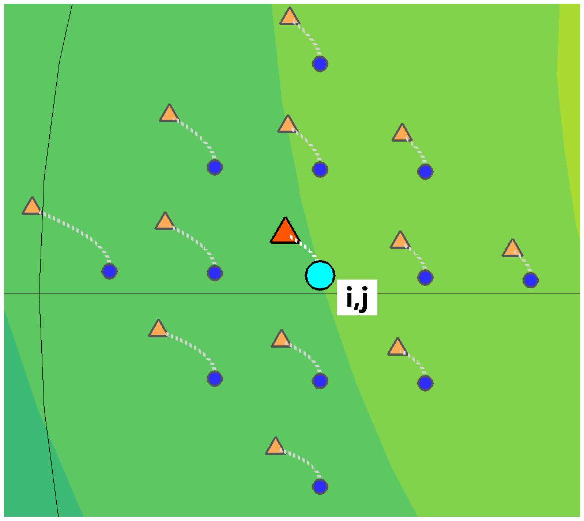

Figure 3.2. Particle trajectories viewed from the freestream flight direction.

be described later in Section 6. Since this mapping exists, it is then possible to use this trajectory information to determine physical particle impact rate at each point on the surface, along with the resulting surface recession.

An early form of the technique was formulated by comparing the spatial distribution of particles on a vehicle surface with the spatial distribution of particles at their initial locations. The spatial density is estimated by computing using the same techniques as utilized in the smoothed particle hydrodynamics (SPH) technique [43]. The convolution of distance between neighboring particles and a compact support kernel results in a spatial density estimate for scattered points. This density comparison is demonstrated in Figure 3.2, where particles spread apart due to the influence of the gas phase, reducing the impact rate on the surface as compared with the case of straight particle paths.

The TCV method differs from Monte Carlo approaches where the number of impacts that occur within an area are divided by a selected time period to yield the impact rate. This requires a large number of sample evaluations to find the true impact rate, and a noisy

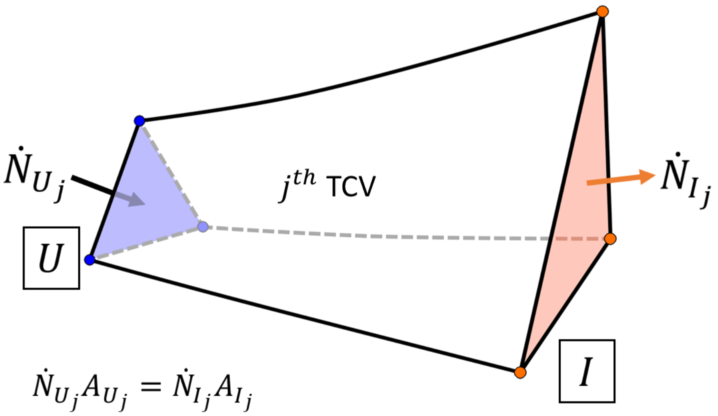

Figure 3.3. Diagram of a typical TCV formed from three particle trajectories. The blue face marked ‘U’ is the upstream face, while the orange face marked ‘I’ is the impact face. The number flux of particles entering the blue face and exiting the orange face is balanced.

distribution may result without implementing steps to smooth the data. The impact rate determination is the core of the TCV method, and will be presented for a simple 1D scenario and a full TPS surface.

The first step in constructing a TCV is to solve for the trajectories of a selection of particles using one-way coupling to the gas phase as described in Section 2. After solving the trajectory of each particle, TCVs can be formed from them. Figure 3.3 shows a representative TCV formed by three particle trajectories. The basic concept of a TCV is similar to that of a streamtube [44]; here being defined by the region of space swept by a collection of particle trajectories. As it is assumed that two neighboring trajectories don’t cross there can be no particle flux through lateral faces of a TCV (denoted by the white faces in Figure 3.3). This results in the balance of particle number flux between the upstream and impact faces (denoted blue and orange, respectively in Figure 3.3), which is the basis of the TCV method. Because there is no particle flux through the white faces, they serve as a logical construct and are ignored from an implementation standpoint.

The method of selection of particles for a given TCV is a matter of implementation, and has significant effects on the other parts of Algorithm 1 given in Sec. 3.2.2. For this study, an unstructured approach is taken by applying Delaunay triangulation [45] to the initial locations of particles. Using Delaunay triangulation results in TCVs with minimum skewness and no overlapping, leading to a simple and robust implementation. The particle group for a set of TCVs is stored and used to identify the positions and areas for both the upstream and impact faces.

3.2. THE DILATION FACTOR AND PREDICTION OF SURFACE IMPACT RATE

After forming the TCVs, their upstream and impact face areas (A_U and A_I in Figure 3.3) are used to determine the impact rate per unit area over the impact face. As discussed in the previous section, the flux of particles is balanced by only the upstream and impact faces, resulting in a simple expression:

$$\dot{N}_U A_U = \dot{N}_I A_I, \tag{3.1}$$

where $\dot{N}_U$ and $\dot{N}_I$ are the particle fluxes through faces U and I, respectively. Using this flux balance it is then possible to compute the actual particle impact rate per unit area over the impact face, accounting for surface inclination and the effect of the gas phase solution on the particle phase. This can be expressed as a correction term multiplied by the upstream particle flux, which is the rate of particles encountered by a unit of area ahead of the shock-layer:

$$\dot{N}_I = \dot{N}_U f_D, \tag{3.2}$$

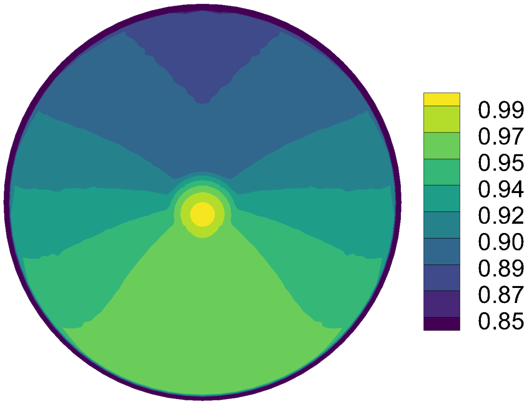

Figure 3.4. Normal view of ExoMars TPS with 2 μm radius dust particle dilation factor contours.

where the correction factor is named the dilation factor, f_D. The dilation factor (named as such because it is a measure of the degree to which two or more particle trajectories spread apart, or dilate, from each other) is formulated as the ratio of TCV face areas:

$$f_D = \frac{A_U}{A_I}. \tag{3.3}$$

By formulating the impact rate this way, the particle encounter rate can be precomputed and multiplied by the dilation factor of each individual TCV. In addition to this, insights about the effect of the gas phase on the particle phase can be derived. Figure 3.4 shows the variation in the dilation factor over the surface of the ExoMars TPS for 2 μm radius particles.

To demonstrate the computation of dilation factor, a simplified one dimensional example of the TCV method is presented here with Figure 3.5 given as a diagram for the problem. A series of particles are seeded along a line and their trajectories are traced to impact. The particles start with an upstream spacing, h_1, of 0.1 meters. Taking a TCV to be defined by the particles in orange, their impact spacing, h_2, is 0.119 meters, which results in a dilation factor of 84.2% using Eq. (3.3). This value means that the number of particles

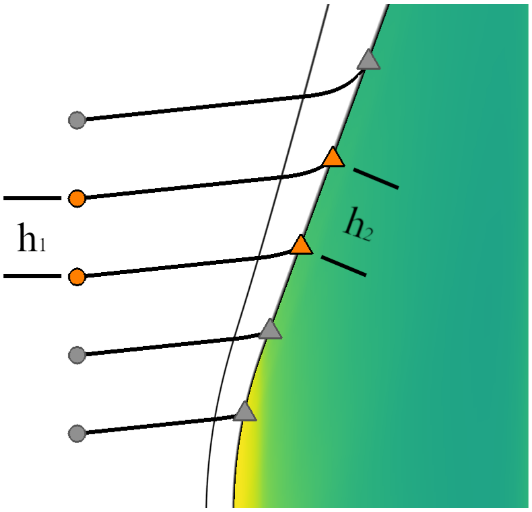

Figure 3.5. Simple 1D TCV example, showing how the diverging impact locations reduce the impact rate over the surface compared to the upstream particle encounter rate.

per unit area impacting the region between the particles' impact points is on average 84.2% of the upstream value. Therefore if 100 particles per meter per second are seeded between the 2 probe particles, the resulting impact density between the probe impact points would average 84.2 particles per meter per second. An example of how this differs from a simple inclination-based approach is given in Ref. [46].

As a comparison, the dilation factor is estimated using the Newtonian pressure distribution divided by two. The purpose of this comparison is to show that under certain conditions the impact rate can be estimated using local surface inclination methods. The approximate dilation factor is:

$$f_D \approx sin^2(\theta), \tag{3.4}$$

where θ is the angle between the flow direction and surface. In this case, the flow has an angle of 6.0 degrees, and the surface has an angle of 70 degrees, resulting in an approximate dilation factor of 0.941. This approach over-predicts the value computed with TCV by about 10%. While this approximation is reasonably accurate near the stagnation point, it deteriorates away from this region as the flow velocity tangent to the surface increases, which causes particle trajectories to drift further downstream. In the limit of increasing particle diameter the particle trajectories remain perfectly straight, resulting in the Newtonian approximation recovering the exact dilation factor. This means that for heavy particles, or regions near the stagnation point the true impact rate can be approximated with reasonable accuracy using the Newtonian approximation, demonstrating that it may be possible to develop a simple engineering correlation based on a dilation factor correction term that provides erosion estimation without high-fidelity simulation. For complicated vehicles the TCV method provides a much more accurate result since it considers the full effect of the gas phase on the trajectories of particles.

For the computation of surface impact rate, the upstream particle encounter rate per unit area (also referred to here as the upstream particle flux), $\dot{N}_U$ must first be computed. The upstream particle flux is problem dependent, and will be presented in the following sections where relevant. Applying Eqn. (3.2) with this upstream particle flux will result in the particle flux at the TCV impact face, which will be the surface impact rate for TCV impact faces which coincide with the surface of a vehicle. After computing the dilation factor and impact rate for each TCV, it is then useful to reconstruct the impact rate at the particle locations. This results in a C_1 continuous erosion solution over the TPS surface. For this study, the impact rate over each TCV shared by a particle are averaged with area weighting to compute the local impact rate per unit area at that location. This *node centered* impact rate data is then used to compute the recession rate.

3.2.1. Resampling the TCV Solution. As particles of different sizes starting at the same location will shift their impact point based on their initial radius, quantities which are a function of the impact rate of particles of a given size will not be collocated at this step. To simplify the integration of quantities over the particle radii at a given point, the data is resampled to surface grid point locations specified by the CFD grid.

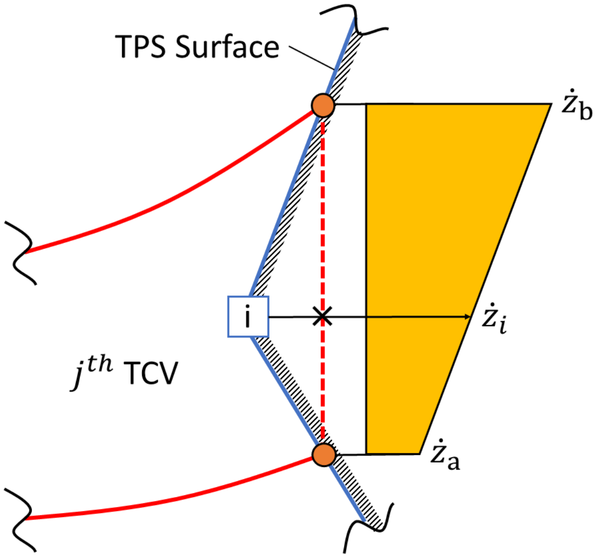

Figure 3.6. Diagram showing the resampling process for a TCV. Linear interpolation is used to sample the recession rate between particle impact locations.

To resample the solution within a TCV, the first step is to project the grid point to the impact plane of the TCV. This is necessary because grid points will not be perfectly coplanar with the TCV exit plane. Projecting the point also simplifies the interpolation process. In this study, as triangular TCVs are used, a simple projection based point-in-triangle test is used to find the projected location in terms of the barycentric coordinates [47]. The interpolated value is found by simply multiplying the barycentric coordinates (γ_a, γ_b and γ_c) by their corresponding impact point quantities, such as impact crater volume, as will be seen in the Section 6.1 which studies mechanical surface erosion. For example, assuming a quantity Z is defined at the TCV particle impact points, the following barycentric interpolation is used:

$$Z_i = \gamma_a Z_a + \gamma_b Z_b + \gamma_c Z_c. \tag{3.5}$$

Figure 3.6 demonstrates an example TCV being resampled to a point which doesn't lie exactly in the plane swept by the particle impact locations. After resampling the erosion solution for all particle radii, the total recession rate is found by numerically integrating the

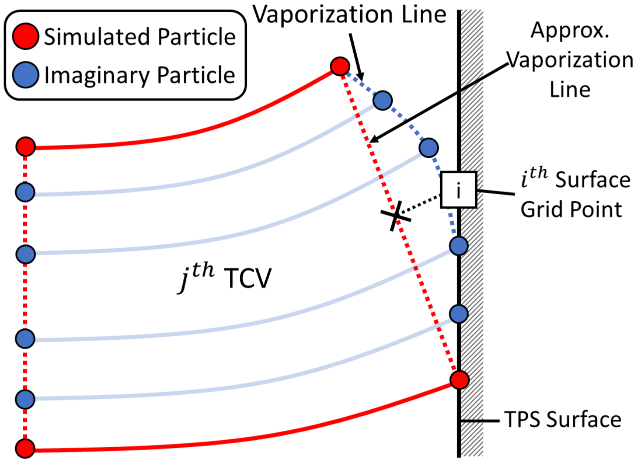

Figure 3.7. Diagram showing the resampling process for a TCV built with an evaporated particle.

mass fraction weighted erosion as a function of particle radius:

$$\dot{Z}_T \approx \sum_{k=1}^{N_{radii}} \frac{\Delta r_p}{2} \left[\dot{Z}(r_k) + \dot{Z}(r_{k+1}) \right] . \tag{3.6}$$

For small particle radii, it is possible that some of the particles may evaporate before reaching the vehicle surface. TCVs formed using these particles are processed the same as described above, with the exception that crater volume is evaluated to zero for these particles. Figure 3.7 shows a common scenario in which a TCV consists of both evaporated and impacting particles. The blue particles represent imaginary trajectories between the real TCV boundaries, showing that the TCV exit face approximates the true vaporization surface. Under refinement, the TCV exit faces will better approximate this vaporization surface where particles have a mass of zero. Grid points which sample from these TCVs then evaluate to a recession rate of zero.

Another edge case which can occur is when one or more particles, which make up a TCV, do not impact the vehicle but rather pass around it. In this scenario, the exit face of the TCV can become skewed and underpredict the impact rate over the region swept by this area. For legacy scale vehicles this effect is localized near the shoulder of a vehicle where it begins to turn towards the afterbody, as particles which are small enough to lose sufficient momentum to be carried around the vehicle are vaporized instead. For larger vehicles, however, such as HIAD or ADEPT, some particle sizes are large enough not to vaporize but small enough to lose momentum and be carried around the vehicle, resulting in the skewed TCV scenario occurring on regions of the flank just before the shoulder. For legacy scale vehicles, such as the case studied in this work, TCVs which are near the vehicle shoulder are limited by the choice of grid topology used, in which an outflow boundary is placed at the edge of the shoulder just before the shadow region. Particles which would have been carried past the vehicle are stopped at this boundary, and the resulting skewness error is limited. Under refinement of the TCVs by increasing the particle count, the skewness of the TCVs are reduced, and the resulting error becomes negligible. For larger vehicles where this scenario can occur further in to the forebody region, an artificial limiter scheme may be necessary to prevent undesirable skewness of the TCVs.

3.2.2. Algorithm Overview. The full approach of the TCV method applied to surface erosion by dust impact is given in Algorithm 1, making use of the equations and description given previously in this section. Starting with a given set of particle initial locations and trajectories (including aerothermal history), as well as a surface grid and upstream gas flow and atmospheric dust conditions, particles are grouped in to a set of TCVs using their upstream positions using Delaunay triangulation. This results in a collection of TCVs of total N_{TCV}. For each particle radii from 1 to N_{radii}, start by computing the dilation factor and impact rate per unit area of each TCV using Eq. (3.3). Next, convert the cell averaged impact rate per unit area to nodal values. Next, for each particle from 1 to $N_{\text{particles}}$, compute the impact crater volume using Eq. (6.14) for the corresponding impact conditions, and subsequently the surface recession rate at the impact location using Eq. (6.15). Then for each surface grid point, resample the recession rate information from the containing TCV region as described in Section 3.2.1. Finally, integrate the recession rate over particle radius using the trapezoidal rule to compute the total erosion at each surface grid point, $\dot{Z}_T$.

Algorithm 1: Solution of surface erosion with the Trajectory Control Method

```
Input: Particle seed locations and impact data (position, mass, velocity) and
       surface grid
Input: Upstream flow properties
Output: Recession rate evaluated at surface grid points [mm/s]

group particles into TCVs using their upstream starting positions, $\text{TCV}_j \leftarrow$
  $\text{Delaunay}(\text{x}_u, \text{y}_u, \text{z}_u)$;
for $i \leftarrow 1$ to $N_{radii}$ do
    for $j \leftarrow 1$ to $N_{TCV}$ do
        compute the dilation factor, $f_D[i,j] \leftarrow \frac{A_U[i,j]}{A_I[i,j]}$;
        compute impact rate over TCV impact face, $\dot{N}[i,j] \leftarrow \dot{N}_\infty f_D[i,j]$;
    end
    convert cell average impact rate to nodal impact rate, $\dot{N}[i,k] \leftarrow \dot{N}[i,j]$;
    for $k \leftarrow 1$ to $N_{Particles}$ do
        compute impact cratering for each particle,
          $\forall_c[i,k] \leftarrow \forall_c(x,y,z,u,v,w,m)$;
        compute surface erosion for radius $r[i]$ at TCV node positions,
          $\dot{Z}(r[i])[k] \leftarrow \dot{N}[i,k]\forall_c$;
    end
    resample erosion information to surface grid points;
    integrate $\dot{Z}(r[i])$ to total erosion solution, $\dot{Z}_T \leftarrow \dot{Z}_T + \frac{1}{2}\Delta r[i]\,\dot{Z}(r[i])$;
end
```

3.3. NONCONTIGUOUS TCV FORMATION

As the flux between neighboring TCVs is assumed to be zero, an improvement to the approach are possible. This improvement is the relaxation of the requirement that TCVs are contiguous in space. This allows for groups of particles to be seeded very close to each other near where a sample is desired, and assembled into small TCVs, which do not share boundaries with one another. The primary benefit of this concept is that high accuracy can be achieved by using closely spaced particles that capture only the local effect

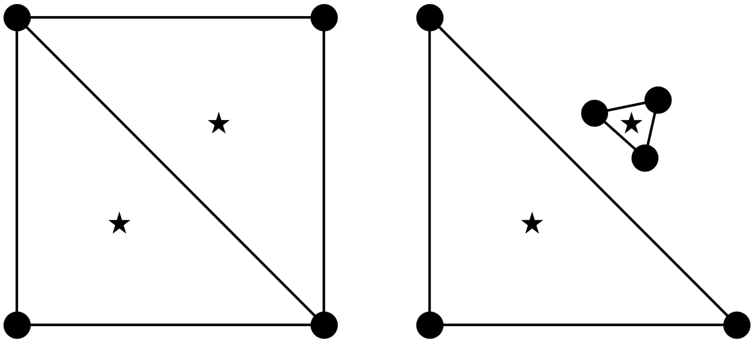

Figure 3.8. Comparison of (left) contiguous and (right) noncontiguous TCV configurations.

of the gas phase on particles near the mean trajectory, without requiring the large increase in total particle count that would come from contiguous TCVs having the same relative refinement level. In addition, this makes the analysis process simpler, as TCVs formed in this way do not have particle trajectories that diverge from each other significantly, such as in the case of a TCV that contains particles that contact a vehicle surface and particles that pass a vehicle and move far downstream. The downside of this approach is that a noncontiguous configuration has a larger particle count for the same number of TCVs arranged contiguously. A combination of contiguous and noncontiguous TCVs could be used to minimize this increase in particle count if necessary. Figure 3.8 shows an example of contiguous and noncontiguous configurations with the same upstream face centroids. While not employed in the present work, the Appendix presents a differential limit formulation of the TCV method which takes advantage of the non-contiguous TCV formation concept.

3.4. TWO-WAY COUPLING

In a two-way coupled solution, information is exchanged between the gas and particle phases symmetrically unlike the one-way coupled results presented in Sec. 6.1. Cumulative information about the particle phase is injected to the gas phase governing equations as source terms, and the solution of both phases are progressed together or in an alternating, or loosely-coupled fashion. For hypersonic problems, the governing equations of species continuity, momentum, vibrational-electronic energy, and total energy are as follows [34]:

$$\frac{\partial \rho_s}{\partial t} + \frac{\partial \rho_s u^j}{\partial x^j} = \frac{\partial}{\partial x^j}\left(\rho D_s \frac{\partial y_s}{\partial x^j}\right) + \dot{w}_s + S_{\rho,s} \tag{3.7a}$$

$$\frac{\partial \rho u^i}{\partial t} + \frac{\partial \rho u^i u^j}{\partial x^j} = -\frac{\partial p}{\partial x^i} + \frac{\partial}{\partial x^j}\left[\mu\left(\frac{\partial u^i}{\partial x^j} + \frac{\partial u^j}{\partial x^i}\right) - \frac{2}{3}\mu\frac{\partial u^k}{\partial x^k}\delta^{ij}\right] + S_m^i \tag{3.7b}$$

$$\begin{aligned}\frac{\partial \rho e_e}{\partial t} + \frac{\partial}{\partial x^j}\left[u^j(\rho e_e + p_e)\right] &= u^j\frac{\partial p_e}{\partial x^j} + \frac{\partial}{\partial x^j}\left(\eta_e\frac{\partial T_{ve}}{\partial x^j}\right)\\ &+ \frac{\partial}{\partial x^j}\left(\rho\sum_{s=1} N_s h_{e,s} D_s \frac{\partial y_s}{\partial x^j}\right) + 3\rho_e \bar{R}(T - T_{ve})\sum_{s=1}^{N_s-1}\frac{\nu_{es}}{M_s}\\ &- \sum_{\text{ions}}\dot{n}_{e,s}\hat{I}_s - \sum_{\text{molecules}}\rho_s\frac{(e_{v,s}^{**} - e_{v,s})}{\langle\tau_{es}\rangle} - Q_{\text{rad}}\end{aligned} \tag{3.7c}$$

$$\begin{aligned}\frac{\partial \rho E}{\partial t} + \frac{\partial \rho H u^j}{\partial x^j} &= \frac{\partial}{\partial x^j}\left(\eta_{tr}\frac{\partial T_{tr}}{\partial x^j} + \eta_{ve}\frac{\partial T_{ve}}{\partial x^j}\right) + \frac{\partial}{\partial x^j}\left(\rho\sum_{s=1}^{N_s} h_s D_s\frac{\partial y_s}{\partial x^j}\right)\\ &+ \frac{\partial}{\partial x^j}\left[u^i\mu\left(\frac{\partial u^i}{\partial x^j} + \frac{\partial y^j}{\partial x^i}\right) - \frac{2}{3}u^i\mu\frac{\partial u^k}{\partial x^k}\delta^{ij}\right] - Q_{\text{rad}} + S_E,\end{aligned} \tag{3.7d}$$

where s refers to a species in $\{1, 2, ..., N_s\}$, and i refers to the momentum in $i = \{x, y, z\}$ directions. Further details of the notation used here are given in Ref. [34]. The added source terms for two-way coupling are highlighted in red. The contributions of $S_{\rho,s}$, S_{m^i}, and S_E, represent the transfer rate of species mass, directional momentum, and total energy, respectively, from the particle phase to the gas phase within a computational cell. The radiative flux divergence, shown in blue, is only indirectly affected by the particle phase due to interaction with the radiative transport. In this work, particles are assumed to only directly exchange energy with the gas phase total energy field.

3.4.1. Coupled Analysis with Monte Carlo Techniques. The most general way to compute coupling source terms for the particle phase is to sum the instantaneous effect of each particle on the gas phase. Two key simplifications are necessary however using an Eulerian CFD approach for the gas phase. The first simplification is the rectification of the continuum nature of the gas phase with the Lagrangian nature of the particle phase. This is performed by averaging the effect of particles within a region of space. The second simplification is that of the total particle count. As simulating the true number of particles in a computational domain is not feasible, computational particles are typically assumed to represent a large number of physical particles. For the MC solution strategy, such as that presented by Ching et al. [40], the source terms for species mass, directional momentum, and total energy are computed in an instantaneous sense as the following:

$$S_{\rho,s} = -\sum_{n=1}^{N_p} \dot{w}_{s,n} X\left(\vec{x} - \vec{x_{p,n}}\right) \tag{3.8a}$$

$$S_{m^i} = -\sum_{n=1}^{N_p} \vec{F}_n X\left(\vec{x} - \vec{x_{p,n}}\right) \tag{3.8b}$$

$$S_E = -\sum_{n=1}^{N_p} \left(\dot{Q}_n + \vec{u}_{p,n} \cdot \vec{F}_n\right) X\left(\vec{x} - \vec{x_{p,n}}\right), \tag{3.8c}$$

where N_p is total number of particles in the domain and $X\left(\vec{x} - \vec{x}_{p,n}\right)$ is a kernel function for partitioning the effect of each particle spatially. The most commonly used kernel is the dirac function, which deposits the particles effect to the cell it is currently contained within, though smooth projection kernels can improve solution quality for some scenarios [40].

For steady solutions, such as what is presented in the current work, a time averaged source term is necessary rather than the instantaneous effect of the particles at each timestep. The steady MC source term was computed in the present work by summing the steady source term contribution of each simulated particle. The steady source term contribution for the particle phase was found by following this procedure:

- Find the intersections of the particle trajectory with the boundaries of each computational cell it passes through.
- Integrate the contribution to a field over the period of time the particle spends within a given cell.
- After summing the contribution of each particle, scale the source field by the time required to encounter the total number of particles simulated.

Figure 3.9 demonstrates the determination of cell intersections for a particle trajectory. The simulated trajectory is represented by the black circles, while the red triangles represent the intersections of the trajectory with cell boundaries. In the current work a piecewise linear trajectory was assumed and bisection was used to find the intersection points. Then, the instantaneous source term for a given field was integrated between each intersection time using a two point Gauss quadrature rule:

$$S_{i,a\to b} = S_i\left(\frac{t_a+t_b}{2} - \frac{t_b-t_a}{\sqrt{3}}\right) + S_i\left(\frac{t_a+t_b}{2} + \frac{t_b-t_a}{\sqrt{3}}\right). \tag{3.9}$$

The instantaneous source term for a field, $S_i(t)$, at time t was computed by interpolating the particle state from the piecewise linear trajectory as a function of time, and evaluting the source term for the given fields. In the present work only momentum and energy source terms were considered. The instantaneous source terms for momentum and energy are given as:

$$\vec{s}_{\text{momentum}} = -\vec{F}_p \tag{3.10a}$$

$$s_{\text{energy}} = -(\dot{Q}_p + \vec{F}_p \cdot \vec{u}_p), \tag{3.10b}$$

where $\vec{F}_p$, $\dot{Q}_p$, and $\vec{u}_p$ are the particle force vector, convective heat transfer, and velocity vector as described in Sec. 2.2. After summing the contribution of each simulated particle, the source fields are scaled by the time required to encounter the total number of simulated particles, t_{seed}, as described in Sec. 6.1.4.

3.4.2. Extension of the TCV Method for Coupled Analysis. The TCV method was extended to two-way coupling by subdividing TCVs along the mean trajectory and using the particle transit rate to formulate the volumetric source term in each subdivision. Figure 3.10 demonstrates the subdivision of the simple two-dimensional TCV shown in Figure 3.3, with indices ’j-1’, ’j’, and ’j+1’ referring to neighboring sub-regions of the TCV.

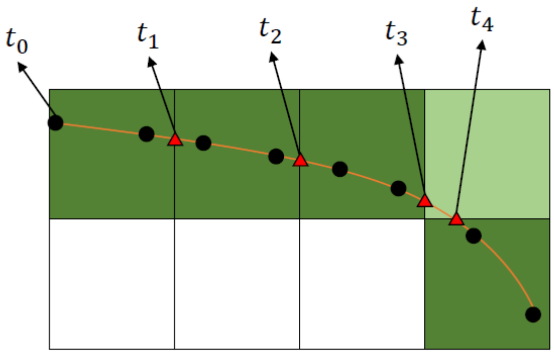

Figure 3.9. Diagram of a particle trajectory through a computational grid, subdivided at cell boundaries for source term deposition.

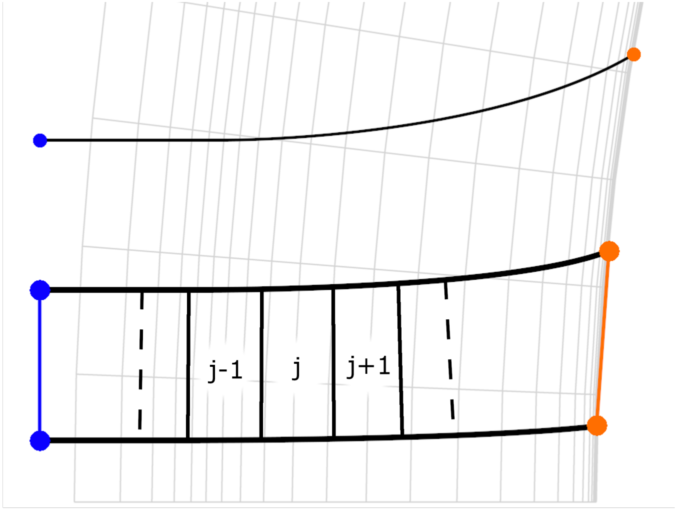

Figure 3.10. Subdivision of a TCV for coupling.

Figure 3.11 shows the 'j^{th}' subdivision of the 'i^{th}' TCV. Particle trajectories 'k' and 'k+1' of the 'i^{th}' TCV are shown with their respective states 'j' and 'j+1' forming the TCV subdivision 'j'. The particle transit rate, or number of particles passing through the TCV per unit time, for the 'i^{th}' TCV, $\dot{N}_{T,i}$, is indicated at the inflow of the subdivision, as it is constant through the TCV. Recall that the surfaces of the TCV are defined by the particle trajectories (horizontal lines in Figure 3.11), so flux is only considered across the subdivisions within the TCV (vertical lines in Figure 3.11).

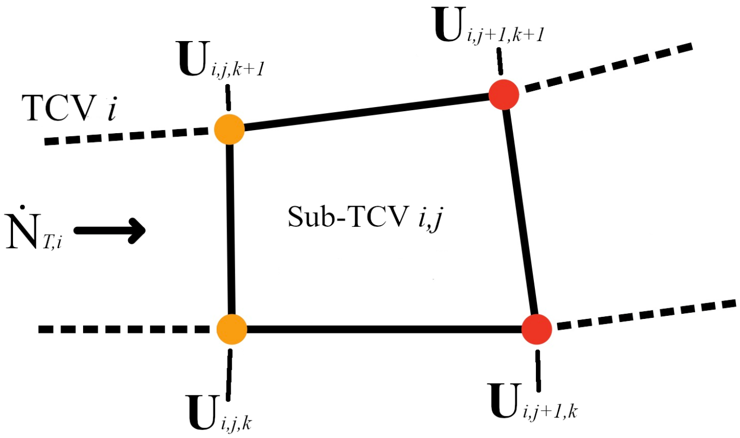

Figure 3.11. Diagram showing a region of a TCV which has been subdivided.

Defining a flux function for the particle state allows the source term to be solved in terms of a difference of fluxes across the sub-TCV's inlet and outlet faces. The flux function is defined as:

$$\mathbf{F}(\mathbf{U}) = \begin{bmatrix} m_p \\ m_p \vec{u}_p \\ Q_p + \frac{1}{2} m_p \left| \vec{u}_p \right|^2 \end{bmatrix}. \tag{3.11}$$

The rate of change in the flux function represents the instantaneous effect of a particle on the surrounding gas:

$$\frac{\partial \mathbf{F}(\mathbf{U})}{\partial t} = - \begin{bmatrix} \dot{m}_p \\ \vec{F}_p \\ \dot{Q} + \vec{u}_p \cdot \vec{F}_p \end{bmatrix}, \tag{3.12}$$

while the difference of flux functions between two points represents its integral in time:

$$\int_{t_1}^{t_2} \frac{\partial \mathbf{F}(\mathbf{U})}{\partial t} dt = \mathbf{F}(U_2) - \mathbf{F}(U_1). \tag{3.13}$$

Using this, the cumulative effect of all particles passing through the region of space bounded by the sub-TCV on the gas phase is the average flux difference multiplied by the particle transit rate, after which it is made volumetric by dividing by the sub-TCV volume, $\forall$,

$$\mathbf{S}_{i,j} = \frac{\dot{N}_{T,i}}{N_{p,i}\forall_{i,j}} \sum_{k=1}^{N_{p,i}} \Delta\mathbf{F}(\mathbf{U})_{i,j,k} = \frac{\dot{N}_{T,i}}{N_{p,i}\forall_{i,j}} \sum_{k=1}^{N_{p,i}} \left[\mathbf{F}(\mathbf{U})_{i,j+1,k} - \mathbf{F}(\mathbf{U})_{i,j,k}\right], \tag{3.14}$$

where $N_{p,j}$ is the number of particle trajectories forming the 'j^{th}' TCV. Repeating this process for every TCV results in a source term field in which the data is located at sub-TCV centroids. Much like in the original TCV formulation for surface erosion [35], the next step is to resample the data to the gas-phase grid using a suitable interpolation technique. In this study, the function 'interp2d' in the 'SciPy' python library is used with a linear type interpolant [48]. This function triangulates the scattered data to build the piecewise interpolant. For 3D cases a radial-basis-function (RBF) based interpolant would likely provide more flexibility. Algorithm 2 details the full process of creating two-way coupling source fields using the TCV method.

Algorithm 2: Solution of source fields using the Trajectory Control Volume Method.

```
Input: Particle trajectory data (position, mass, velocity) and computational grid
Input: Upstream flow properties
Output: Volumetric particle two-way coupling source field [kg/m$^3$s, N/m$^3$, W/m$^3$]

group particles into TCVs using their upstream starting positions, TCV$_j$ $\leftarrow$ formTCVs(x$_u$, y$_u$, z$_u$);
for $r \leftarrow 1$ to $N_{radii}$ do
    compute radius mass fraction, $X(r_p) \leftarrow$ MassFraction($r_p$);
    compute upstream particle flux, $\dot{N}_U \leftarrow \frac{\beta X(r_p)\rho_\infty U_\infty}{m_p(r_p)}$;
    for $i \leftarrow 1$ to $N_{TCV}$ do
        compute particle transit rate from upstream particle flux and TCV$_i$ upstream area, $\dot{N}_{T,i} \leftarrow \dot{N}_U A_{U,i}$;
        subdivide TCV$_i$ into $N_{\text{sub},i}$ sub-volumes;
        for $j \leftarrow 1$ to $N_{sub,i}$ do
            compute sub-TCV volume, $\cancel{V}_{i,j} \leftarrow$ computeVolume(tcv_mesh$_{i,j}$);
            for $k \leftarrow 1$ to $N_{p,i}$ do
                compute flux difference for sub-TCV, $\Delta\mathbf{F}_{i,j,k} \leftarrow$ fluxDiff(pstates$_{i,j,k}$,pstates$_{i,j+1,k}$);
            end
            average flux differences, $\Delta\bar{\mathbf{F}}_{i,j} \leftarrow \frac{1}{N_{p,i}} \sum_{k=1}^{N_{p,i}} \Delta\mathbf{F}_{i,j,k}$ ;
            compute source terms for sub-TCV, $\mathbf{S}_{r,i,j} \leftarrow \frac{\dot{N}_{T,i}\Delta\bar{\mathbf{F}}_{i,j}}{\cancel{V}_{i,j}}$ ;
        end
    end
    resample the source field from TCV grid to gas phase grid, $\mathbf{S}_{g,r} \leftarrow$ resample($\mathbf{S}_r$);
    integrate radius source field to total source field, $\mathbf{S}_{g,total} \leftarrow$ integrate($\mathbf{S}_{g,total}, \mathbf{S}_{g,r}, r_p(r)$);
end
```

4. THE CONTINUUM PARTICLE PHASE APPROACH

This section describes the formulation and implementation of a continuum particle phase solver for hypersonic dilute particle-laden flow problems. The continuum particle phase approach uses a fixed mesh to track the average state of the particle phase within each control volume. In contrast to the Lagrangian framework, where particles are tracked as point masses through a backgroun CFD solution, the continuum particle phase approach utilizes the same CFD mesh and solution to collocate data. As the continuum particle phase solution is a field on a mesh, many downstream analysis tasks are simplified by not requiring complicated interpolation steps. This simplification comes at the cost of solving a coupled PDE system, which is more complicated that simple Lagrangian particle tracking. In this section, an overview of the Eulerian form of the particle phase governing equations is derived, after which the details of the solution approach are given. Next, verification of the continuum particle phase solver against a Lagrangian solution is presented. Finally some discussion of the relative strengths and application differences of the approaches are given.

4.1. EULERIAN DESCRIPTION OF THE PARTICLE PHASE

With the same assumptions leading to Eqn. (2.13), it is possible to directly transform the particle phase governing equations from a Lagrangian frame to an Eulerian frame. For a dilute particle phase, in which it can be safely assumed that particles do not collide with one another, this equivalence can be established using the convective derivative similar to other transport problems. Utilizing a streamtube analogy [44, 49], it can be shown that the change in a property along a particle trajectory is balanced by the flux of that quantity across a fixed control volume's boundaries and rate of change of the average of the property within the control volume. Applying this to the mass density of the particle phase, ρ_p, results in the following expression:

$$\frac{D\rho_p}{Dt} = \frac{\partial \rho_p}{\partial t} + \nabla \cdot \left(\rho_p \vec{u}_p\right) = 0, \tag{4.1}$$

where the divergence of the particle phase momentum vector field, $\rho_p \vec{u}_p$, is balanced by the time derivative of the density.

This expression shares the same form as the continuity equation in gas dynamics, and states that overall particle phase mass is conserved. Similarly, this approach can be applied to the momentum and energy along a particle trajectory. In the case of momentum, the convective derivative of particle momentum, $\rho_p \vec{u}_p$, is balanced by the forces on the particle, $\vec{F}_p$. In the case of energy, the convective derivative of particle phase total energy, $\rho_p E_p$, is balanced by heat transfer and work on the particle phase, $Q_p + \vec{u}_p \cdot \vec{F}_p$. This results in the following set of Eulerian particle phase equations:

$$\frac{\partial}{\partial t}\begin{bmatrix} \rho_p \\ \rho_p \vec{u}_p \\ \rho_p e_p \end{bmatrix} + \nabla \cdot \begin{bmatrix} \rho_p \vec{u}_p \\ \rho_p \vec{u}_p \vec{u}_p \\ \rho_p \vec{u}_p e_p \end{bmatrix} = \begin{bmatrix} 0 \\ \vec{F}_p \\ Q_p + \vec{u}_p \cdot \vec{F}_p \end{bmatrix}. \tag{4.2}$$

As the particle phase is assumed to be dilute, no pressure forces arise as a consequence of inter-particle collisions. The resulting equations, without the source terms, resemble the Euler equations with the pressure term missing from the momentum equation. These pressureless Euler equations have been the subject of numerous studies which seek to treat the complex mathematical nature which arises due to the absense of a pressure term [50, 51, 52].

Equation (4.2) is valid for particle phases in which no mass loss occurs during a particle's trajectory. In scenarios where particles can lose mass along their trajectory, a source term can be added to the particle continuity equation to account for effects like vaporization or surface chemistry:

$$\frac{\partial \rho_p}{\partial t} + \nabla \cdot \left(\rho_p \vec{u}_p\right) = n_p \dot{m}_p, \tag{4.3}$$

where n_p is the number density of particles, and $\dot{m}_p$ is the mass exchange rate for a single particle. Crowe [49] discusses the addition of a mass source term and demonstrates the validity of the assumption based on the conservation of particle number density along a streamline of the particle phase.

For problems in which particles experience strong mass loss rates and change radius significantly, it may be necessary to track the radius as a solution variable in order to accurately evaluate closure models like the drag coefficient and Nusselt number. In order to admit the changing of particle radius throughout the domain, it is necessary to add a PDE which can contribute information to the system about the particle radius. Because the particle phase density, ρ_p, is related to the radius, r_p, (assuming spherical particles) through the number density:

$$\rho_p = m_p n_p = \frac{4}{3}\pi \rho_m r_p^3 n_p, \tag{4.4}$$

it is possible to develop an additional conservation equation due to the observation that the number density along a trajectory is conserved [49]. By enforcing this condition, the loss in the density field then results in a smaller radius when computing r_p from ρ_p and n_p. Crowe [49] neglects to add this PDE and simply evaluates the drag coefficient and Nusselt number models using a constant particle radius instead. Masi et al. [53] utilize the additional number density PDE:

$$\frac{\partial n_p}{\partial t} + \nabla \cdot n_p \vec{u}_p = 0, \tag{4.5}$$

and recast the entire PDE system in terms of number density. The number density conservation system is written:

$$\frac{\partial}{\partial t}\begin{bmatrix} n_p \\ n_p m_p \\ n_p m_p \vec{u}_p \\ n_p m_p e_p \end{bmatrix} + \nabla \cdot \begin{bmatrix} n_p \vec{u}_p \\ n_p m_p \vec{u}_p \\ n_p m_p \vec{u}_p \vec{u}_p \\ n_p m_p \vec{u}_p e_p \end{bmatrix} = \begin{bmatrix} 0 \\ n_p \dot{m}_p \\ \vec{F}_p + n_p \vec{u}_p \dot{m} \\ Q_p + \vec{u}_p \cdot \vec{F}_p + n_p \dot{m}(\zeta + \vec{u}_p \cdot \vec{u}_p) \end{bmatrix}, \tag{4.6}$$

where ζ is the heat released per unit mass loss rate, $\dot{m}$. For scenarios where the mass loss rate is zero, Eqn. (4.6) reduces to Eqn. (4.2). As such, Eqn. (4.6) is used in the current work.

4.2. SOLUTION APPROACH

In the current work, the finite volume method is used to discretize the nonlinear system of partial differential equations (PDE) describing the Eulerian form of the particle phase governing equations given in Eqn. (4.6). The PDE system is first transformed into an integral form suitable for discretization:

$$\frac{\partial}{\partial t}\int_{\forall} \mathbf{U} d\forall + \int_{S} \mathbf{F}(\mathbf{U}) \cdot \hat{n} dS = \int_{\forall} \mathbf{S} d\forall, \tag{4.7}$$

where **U** is the vector of conserved variables, and **F(U)** is the flux vector given in Eqn. (4.6). In this form, the surface integral of the flux on a cell's boundaries is discretized using a suitable finite volume scheme. Due to the similarities to the Euler equations as discussed before, Eqn. (4.7) is treated as a modification to the Euler equations. As such, in the current work the continuum phase particle solver is implemented in an existing CFD code, the NASA HyperSolve CFD Solver [54], through a modified flux scheme and source term. HyperSolve is a node-centered, edge-based discretization utilizing a compact 3^{rd} order upwind finite volume scheme [54], which has been developed for use in aerothermodynamic problems in which accurate surface gradients on simplex meshes are required for the prediction of surface heat flux. HyperSolve utilizes the Jacobian-free Newton-Krylov technique for strong nonlinear convergence [55]. In the following sections, the details of the continuum phase particle phase solver implementation will be discussed.

4.2.1. Flux Scheme and Solution Stabilization. The discretized integral equations, Eqn. (4.7), requires the evaluation of the flux vector at each cell interface. The flux vector,

$$F(\mathbf{U}) = \begin{bmatrix} \rho_p \vec{u}_p \\ \rho_p \vec{u}_p \vec{u}_p \\ \rho_p \vec{u}_p E_p \end{bmatrix} \tag{4.8}$$

must be evaluated in such a way that both cells sharing the interface contribute information. The numerical flux is thus taken to be the average of the flux vector evaluated with both cells' reconstructed state at the interface. Additionally, a dissipation term is added to stabilize the numerical scheme. The numerical flux is expressed as:

$$F(\mathbf{U}) = \frac{1}{2}(F_L + F_R) + D, \tag{4.9}$$

where F_L and F_R are the fluxes evaluated using the solution state on each side of a cell interface, and D is the dissipation term. The interface fluxes, $F_{L/R}$, are expressed as:

$$F_{L/R}\left(\mathbf{U}_{L/R}\right) = u_p^{\perp} \begin{bmatrix} \rho_p \\ \rho_p \vec{u}_p \\ \rho_p E_p \end{bmatrix}, \tag{4.10}$$

where $u_p^{\perp}$ is the velocity normal to the cell interface. Some approaches found in the literature introduce a pseudo-pressure term in the flux balanced by a pressure gradient term in the source vector so that standard gas dynamic flux functions can be utilized without modification [52]. In the current work however, a simple dissipation term was found to provide suitable stabilization:

$$D = -\frac{A_F}{2} \left\| e_{\max} \right\| \left(U^{+} - U^{-} \right), \tag{4.11}$$

where A_F is the cell interface area, and $e_{\max}$ is the maximum eigenvalue of the system at the interface. The maximum eigenvalue of the system at the interface is taken to be the maximum of the interface normal velocity on each each side of the interface. A limiter was added that prevents the maximum eigenvalue from falling below a specified value, which was taken to be a nondimensional speed of 0.1 to 0.25 times the freestream value in this study. Harten's entropy fix is used to apply this limiting without introducing discontinuities in the flux evaluation [56].

4.2.2. Shadowing Wall Boundary Condition. Similar to Refs. [10, 35], particles are assumed to embed into the thermal protection system (TPS) of an entry vehicle. An extrapolation boundary condition can be used to model the assumption that particles leave the domain unaffected by solid surfaces. This boundary condition is incorrect for the wake of a vehicle, however, where the particle number density is zero due to the inability of particles to perfectly follow gas streamlines and recirculate into the wake. Regions where particles are not able to enter due to their momentum are referred to here as shadow regions. Jung and Myong [52] present a shadowing boundary condition that switches between extrapolation and a zero-valued Dirichlet boundary condition depending on the directionality of particles with respect to the wall. For particle velocities pointing into the wall, extrapolation is used, while a zero-valued Dirichlet condition is used otherwise:

$$\begin{aligned} \mathbf{U}_{\text{wall}} &= \mathbf{U}_{\text{interior}}, \\ \mathbf{U}_{\text{wall}} &= \mathbf{0} \text{ if } \vec{u}_p \cdot \hat{n} \geq 0. \end{aligned} \tag{4.12}$$

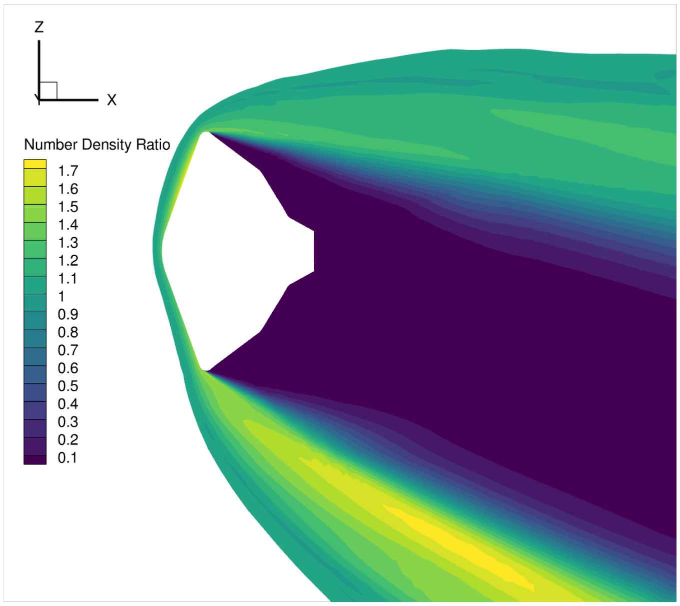

Figure 4.1. Wake shadow region forming in the particle phase around a Mars entry vehicle.

In the current work, it was found that better nonlinear solver stability was obtained by setting the density to a near-zero value and letting other fields extrapolate in shadow regions. A value of 1×10^{-12} was utilized for the density. The number density is also extrapolated, as opposed to setting a value explicitly. In practice, this change was found to be more stable for the cases considered. Figure 4.1 demonstrates a solution in which a shadow region has formed in the particle phase due to the application of the shadow wall boundary condition. Figure 4.2 demonstrates the application of this boundary condition at an point where the particle phase impinges on the vehicle surface and at a point where the surface is in the particle phase shadow. The interior velocity vector is compared with the surface normal vector using Eqn. (4.12) to determine the exterior state to be imposed in the boundary condition.

A challenge which arises when simulating flows in which the particles form a shadow is in nonlinear stability of the solver. The sharp change in particle phase density that occurs on the interface between shadowed and non-shadowed regions can lead to stiff numerics. In order to prevent these regions from slowing down convergence of the entire domain, the

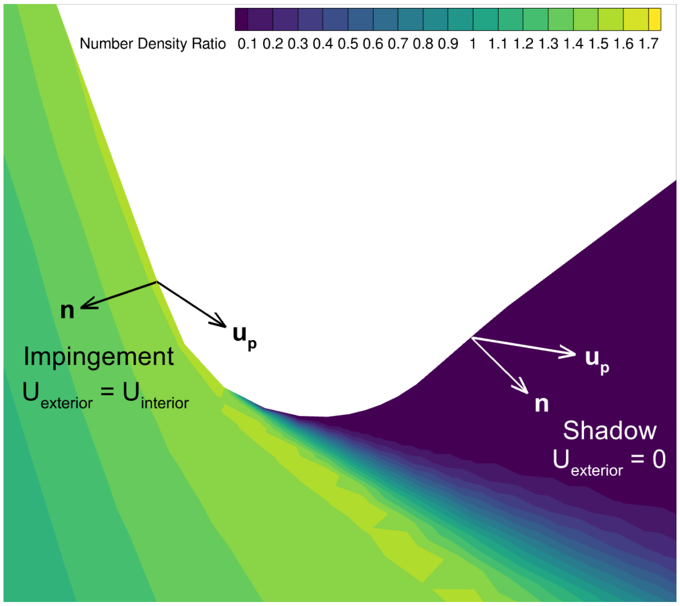

Figure 4.2. Diagram of the shadowing wall boundary condition in both extrapolation and shadowing regions.

timestep is locally reduced in regions of low particle phase density so that stability can be retained while the high density regions approach steady state. The timestep is multiplied at each unknown by the following factor:

$$\Delta t_{\text{augmented}} = \Delta t \left(\sqrt{\tanh(\rho_p)} + \epsilon \right), \tag{4.13}$$

where ϵ is a small value to place a floor on the timestep. The timestep augmentation factor smoothly reduces to a minimimum value of ϵ for regions with low particle phase density, while effectively making no change to the timestep in regions with densities at or above the freestream value. An ϵ value of 10^{-6} was used in the present work. For cases in which large regions of the domain are in shadow, augmenting the timestep in this way was found to provide stabilty and allow convergence to machine zero.

4.2.3. Source Vector. The source term vector in Eqn. (4.6) is evaluated using a fixed gas solution on the same grid as the particle phase solver. While the solution process could be performed tightly coupled with the gas phase, in the current work one-way coupling is used for two reasons. The first reason is that due to the low mass loading utilized in the application cases, which will be presented in Section 6.3, coupling effects with the gas phase are minimal. The second reason is that in the case of Mars, multiple particle sizes are necessary to treat the size distribution. Each particle size requires a unique set of 6 equations to close the system, therefore a tightly coupled solution process would greatly increase the equation count. Utilizing one-way coupling simplifies the solver implementation and convergence as the gas phase is constant and contributes no jacobian information. Recall the source vector:

$$\mathbf{S}(\mathbf{U},\mathbf{U}_{\text{gas}}) = \begin{bmatrix} 0 \\ n_p \dot{m}_p \\ \vec{F}_p + n_p \vec{u}_p \dot{m} \\ Q_p + \vec{u}_p \cdot \vec{F}_p + n_p \dot{m}(\zeta + \vec{u}_p \cdot \vec{u}_p) \end{bmatrix}. \tag{4.14}$$

The primary physical quantities of drag force, $\vec{F}_p$, heat flux, Q_p, and mass loss rate, $\dot{m}_p$ are modeled similarly to the Lagrangian solution process described in Sec. 2.2. For the continuum solver however, the drag coefficient model of Loth et al. [27], referred to here as the Loth 2021 model, is used. In the Loth 2021 model, a number of piecewise functions are utilized to tune the function to experimental and DSMC data. As these piecewise functions result in breaks in the derivatives of the drag coefficient at various Mach and Reynolds numbers, the nonlinear convergence of the particle solver is hampered. To alleviate these issues, all piecewise functions in the model were replaced with linear combinations of the states on either side of the junctions, weighted by a smooth switching function, w. The smooth switching function, commonly referred to as the SmootherStep function, is written [57]:

$$w(x) = 6x^5 - 15x^4 + 10x^3. \tag{4.15}$$

As an example, the following piecewise function:

$$f(x) = \begin{cases} f_a(x) & \text{if } x < x_{\text{junction}} \\ f_b(x) & \text{if } n \geq x_{\text{junction}} \end{cases}, \tag{4.16}$$

is replaced with the following smooth approximation:

$$f(x) \approx \left[1 - w\left(\frac{x_s + x - x_{\text{junction}}}{2x_s}\right)\right] f_a(x) + w\left(\frac{x_s + x - x_{\text{junction}}}{2x_s}\right) f_b(x), \tag{4.17}$$

where x_{junction} is the midpoint of the smooth crossover and x_s is the smoothing width. For the current study, switches based on Mach number are given a smoothing width, x_s, of 0.05, while switches based on Reynolds number are given an x_s value of 0.5. For some conditions near the various Mach and Reynolds numbers on which the terms in the model switch, nonlinear convergence of the solver was found to be improved by utilizing the switching function and parameters given here.

4.3. VERIFICATION

To demonstrate the equivalence of the continuum particle phase governing equations with the Lagrangian form, two verification cases are presented in this section. These cases show that the trajectory history of a single particle is equivalently represented in the Lagrangian and Eulerian solver for one-dimensional and three-dimensional scenarios. In both cases, which are based on Mars EDL scenarios, the particles are assumed to have a radius of 2 μm, a material density of 2940 kg/m^3, a material specific heat of 700 $J/kg/K$, a latent heat of vaporization of 8.6×10^6 J/kg, and a constant vaporization temperature of 2000 K.

4.3.1. One-dimensional Case. In this case, a rectangular domain is given a constant CO_2 gas phase condition based on a post shock state so that the solver can be tested in a typical hypersonic particle-laden flow scenario. The gas conditions for the test case

Table 4.1. Gas conditions for the one-dimensional continuum particle phase solver verification case.

U_∞ (m/s)	T_∞ (K)	U_{ps} (m/s)	T_{ps} (K)	ρ_{ps} (kg/m^3)
3210.88	188.79	392.684	5442.97	7.6398×10^{-4}

are given in Table 4.1 for both the pre-shock state, denoted by the ∞ subscript, and the post-shock state, denoted by the *ps* subscript. The gas is assumed to be a perfect gas with a ratio of specific heats, γ, of 1.29, and viscosity governed by Sutherland's viscosity law:

$$\mu(T) = S_1 \frac{T^{3/2}}{T + S_2}, \tag{4.18}$$

where S_1 and S_2 have values of 1.503519×10^{-6} and 222.22, respectively. The domain is a rectangle of dimensions $1m \times 1m \times 5m$, with the longest dimension being the flow direction. The gas state is defined to be a constant state at the post-shock conditions in Table 4.1, while the particles are introduced to the domain at the pre-shock temperature and velocity. Extrapolation is used on all other domain faces to produce a purely one-dimensional particle phase solution.

To verify the continuum solver, a single particle was traced through the rectangular domain using the same gas solution using the methodology detailed in Section 2. Both solvers utilized the Loth 2021 model for the particle drag coefficient [27], and the Fox model for the Nusselt number [33], and the same vaporization modeling strategy as described in Sec. 2.2.3 with a constant vaporization temperature of 2000 K. Figure 4.3 shows the comparison between the two solvers for this case, demonstrating that the Eulerian and Lagrangian forms of the particle phase governing equations are equivalent under the assumptions made in this work. Furthermore, the results validate that the additional number density PDE correctly tracks the radius change behavior.

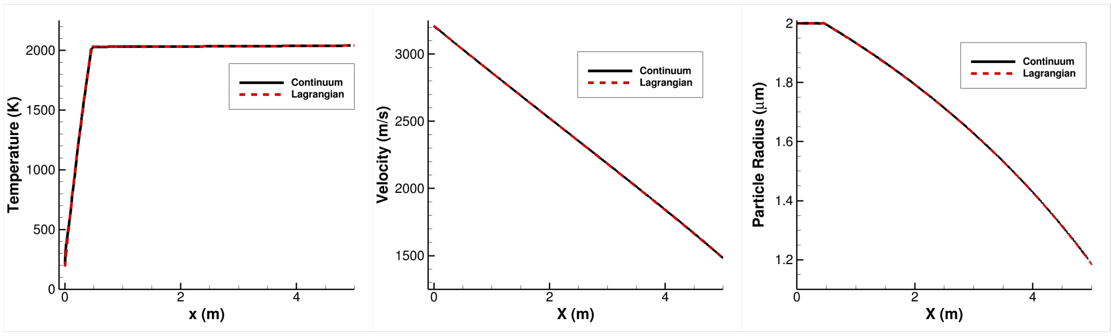

(a) Temperature (b) Velocity (c) Radius

Figure 4.3. Comparison between Lagrangian and continuum particle phase solution approaches for the one-dimensional test problem.

4.3.2. Three-dimensional Case. The three-dimensional verification case is based on the ExoMars Schiaparelli vehicle, which has been the subject of previous studies focused on the prediction of surface erosion by dust impacts in Mars EDL [10, 35]. The freestream conditions for the case are given in Table 4.2. The gas phase was modeled using HyperSolve as an 8 species mixture of perfect gases (CO_2, N_2, CO, NO, O_2, C, N, O) in chemical nonequilibrium. The thermal and transport properties of the gas are modeled according to the methodology of Gnoffo et al. [34] and Gupta et al. [58]. The particle phase was computed using the methodology discussed above, shown in Figure 4.4. In Figure 4.4, the x-component of the particle phase velocity field is shown on the symmetry plane of the domain, and on the surface of the ExoMars vehicle. A single Lagrangian particle was traced through the domain using the initial conditions given in Table 4.3, where the coordinate system is referenced to the apex of the vehicle's nose and oriented as shown in Figure 4.4.

Table 4.2. Gas conditions for the three-dimensional continuum particle phase solver verification case.

ρ_∞ (kg/m^3)	U_∞ (m/s)	T_∞ (K)	α (deg)	$C_{CO_2,\infty}$	$C_{N_2,\infty}$
7.7717×10^{-4}	4016.9	186.3	7.2	0.97	0.03

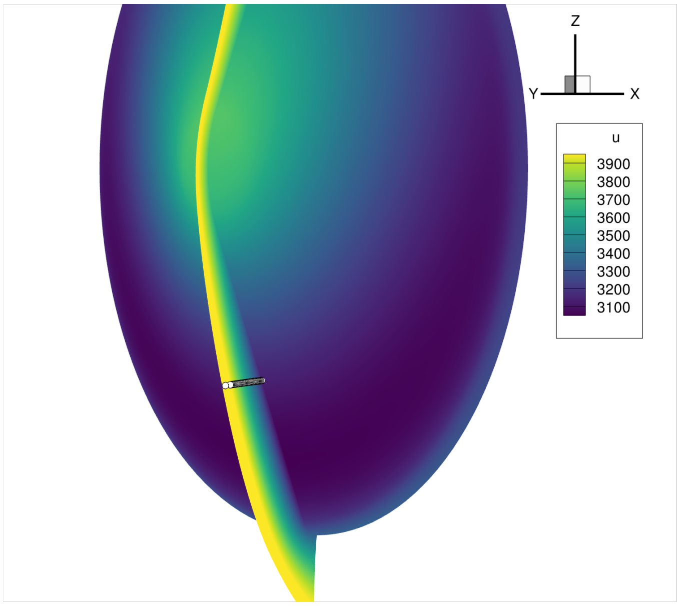

Figure 4.4. Symmetry plane and surface solution for x-component of particle phase velocity, with Lagrangian trace overlayed.

To compare the methodologies in detail, a streamline was traced through the continuum solution using the starting point given in Table 4.3 and compared with the Lagrangian particle's trajectory history in Figure 4.5. As evidenced in Figure 4.5, the techniques agree nearly exactly despite differences in the discretizations similar to the one-dimensional case. These cases furthermore verify that the continuum solver can correctly treat both perfect gas and multi-species nonequilibrium gas models correctly.

Table 4.3. Initial conditions for the Lagrangian particle trace for the three-dimensional verification problem.

x (m)	y (m)	z (m)	u (m/s)	v (m/s)	w (m/s)
0.069187	0	-0.710372	3985.23	0	503.451

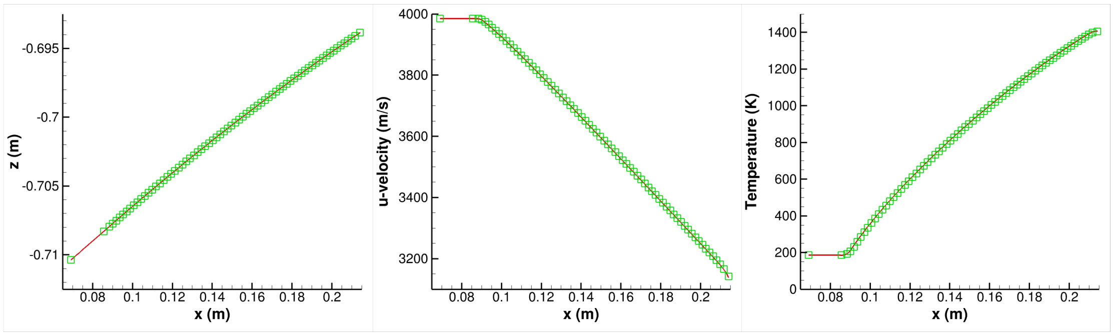

(a) Trajectory (b) X-velocity (c) Temperature

Figure 4.5. Comparison between Lagrangian and continuum particle phase solution approaches for the three-dimensional test problem.

4.4. COMPARISON OF METHODOLOGIES

As shown in the previous verification cases, the continuum solver demonstrates the functional equivalence of the Lagrangian and Eulerian forms of the particle phase governing equations under the assumptions made in this work. It is important however to discuss the practical implementation of both techniques and their relative strengths. For the Lagrangian technique, the following strengths are noted:

- The implementation is generally simple.
- Errors or implementation failures may be localized to a single particle, rather than polluting an entire simulation.
- Including more complicated physical mechanisms, such as inter-particle collisions or wall-rebounding of particles, is relatively simple.
- Multiple different particle sizes can be simulated simultaneously.

The following weaknesses of the technique are noted:

- Overall computational cost can be high if using MC techniques.

- Direct solution techniques like the TCV method are complicated for some scenarios where neighboring particles have significantly different trajectories.
- Interpolation is necessary to resample TCV solutions to a fixed set of locations which may not coincide with particle trajectories.

Conversely, for the continuum particle phase approach, the following strengths are noted:

- High accuracy and smooth solutions are obtained throughout the domain with no artifacts due to interpolating between particle trajectories.
- Easily applied to problems in which a vehicle wake is necessary.
- Computation of the particle phase density or number density is trivial as it is a solution variable of the continuum phase PDE set.

The following weaknesses of this technique are noted:

- The implementation is more complicated and thus more error-prone.
- Cases in which a single particle trajectory are desired are overly expensive as the entire particle phase is solved in concert.
- Simultaneous simulation of different particle sizes requires 6 coupled PDEs per particle size considered, increasing complexity for cases like Mars dust.
- For problems in which errors or nonlinear convergence issues arise, the entire solution may not be useable.
- Moderately higher cost than the TCV approach for simple problems like the forebody of an EDL vehicle.

5. RADIATION TRANSPORT MODELING

An important aspect of EDL is the heating experienced by capsules due to radiative transfer. This source of heating can be a significant contributor to a vehicle's heat load, particularly on the backshell [59]. This study is concerned with determining the extent to which radiation is affected by the presence of micron-scale particulates, as is the case in many atmospheres in our solar system such as that of Mars and Titan.

Prediction of energy transfer by radiation is a complex problem encountered in nearly every discipline of engineering, with many different analysis techniques and approaches applied depending on the radiative transfer regime in question. Due to the wave-particle duality of electro-magnetic radiation, treatment of the problem using an entirely wave- or particle-based nature will inherently not describe all aspects of the physics [15]. In practice, most solution techniques use the particle nature of radiation to solve the coupled transport of energy through the domain, while utilizing the wave nature and quantum mechanics to compute the local radiative properties (e.g. emission and absorption coefficients) resulting from the interaction between electrons and electro-magnetic waves [15]. Still, the integro-differential equations arising from this conceptual framework are difficult to treat as will be discussed in the following sections. The remainder of the section is as follows: First, the radiative transport equation is presented, along with a brief discussion of the computation scattering properties. Next, solution techniques used in the current work are presented. Finally, the verification of the primary radiation transport solver against reference solutions will be given.

5.1. THE RADIATIVE TRANSPORT EQUATION

Under the particle or ray assumption for radiative transfer, radiative energy is assumed to travel through the domain in straight lines in the form of energy packets known as ”photons” [15]. This allows the intensity of radiation to be treated as a function of space,

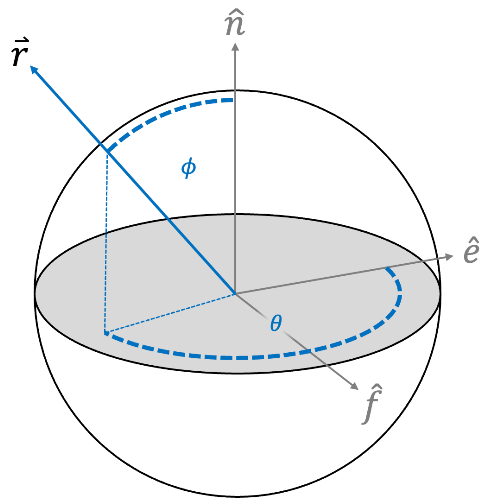

Figure 5.1. Spherical coordinate system oriented to a cartesian vector basis.

orientation, and wavelength:

$$I = I_\nu\left(\vec{x}, \Omega\right), \tag{5.1}$$

where $\vec{x}$ denotes position, Ω denotes an orientation vector, and the subscript ν denotes variation with the frequency of radiation. Intensity is the energy flux per unit solid angle incident on a point in space, and is integrated over all incoming solid angles to compute the radiative heat flux at a point. Radiative flux at a point in space is defined as the integral of radiative intensity over all incoming directions, Ω':

$$q_\nu\left(\vec{x}\right) = \int_{4\pi} I_\nu\left(\vec{x}, \Omega'\right) d\Omega'. \tag{5.2}$$

For a surface, the incoming intensity is weighted by the cosine of the angle formed by the surface normal vector and the incident direction. Generally, a polar coordinate system oriented to the surface normal is assumed, with ϕ being the polar angle, and θ being the azimuthal angle. This coordinate system is shown in Figure 5.1, where $\hat{n}$, $\hat{e}$, $\hat{f}$ are the normal and tangential vectors on a surface or the cartesian basis vectors.

Using this coordinate system, the radiative flux to a surface is written as follows:

$$q_\nu(\vec{x}) = \int_0^{2\pi} \int_0^{\pi/2} I_\nu(\vec{x}, \phi, \theta) \cos\phi \sin\phi d\theta d\phi. \tag{5.3}$$

Computation of radiative intensity is thus the primary challenge in prediction of radiative heating. Under the ray assumption, radiative intensity change through the domain is governed by the radiative transport equation (RTE), which states that the derivative of intensity along a line of sight is balanced by the net flux of photons in a control volume. Modest and Mazumder [15] and Howell et al. [16] both give a comprehensive review of the derivation of the RTE from basic principles, therefore only a brief review will be presented here for context. In one dimension, the frequency-varying RTE is as follows:

$$\begin{aligned} \frac{\partial I_\nu(s,\Omega)}{\partial s} + \{\kappa_\nu(s) + \sigma_\nu(s)\} I_\nu(s,\Omega) &= j_\nu(s) \\ &+ \frac{\sigma_\nu(s)}{4\pi} \int_{4\pi} I_\nu(s,\Omega')\Phi(\Omega,\Omega') d\Omega'. \end{aligned} \tag{5.4}$$

where s is the distance along the line of sight, Ω is the orientation vector, κ is the absorption or extinction coefficient, j_{em} is the gas emission coefficient, σ is the scattering coefficient, and $\Phi(\Omega, \Omega')$ denotes the amount of incoming intensity from the incident direction into the line of sight direction. The four terms of the RTE represent (left-to-right) the (i) change in radiative intensity along a ray, (ii) losses due to absorption and out-scattering (known as the extinction coefficient, $\beta = \kappa + \sigma$), (iii) gains due to emission, and (iv) gains due to in-scattering. The typical assumption of a nonscattering medium results in an RTE that is purely a function of distance along a given ray. This is important as each ray intensity can be solved in isolation of others, which is a key assumption necessary for many approaches implemented for radiative transfer in planetary entry problems. The addition of scattering breaks this assumption as each ray now depends on the incoming radiative flux at each point along the ray.

An important quantity which arises in radiation transport is the optical thickness, τ. Optical thickness is defined as:

$$\tau(a,b) = \int_a^b \kappa(s)ds, \tag{5.5}$$

where $\kappa(s)$ is the absorption coefficient, s is the length along a ray, a is the starting point along a ray, and b is the end point along a ray. For a constant absorption coefficient, the optical thickness is simply κL, where L is the thickness of the absorpting media. Optical thickness is an important measure as many assumptions in radiation transport are valid in either the optically thin limit ($\tau \rightarrow 0$) or the optically thick limit ($\tau \rightarrow \infty$). Because of this, many solution techniques are not universally applicable for all ranges of optical thickness [15].

5.2. SCATTERING

The two mechanisms of scattering are in-scattering and out-scattering, which are gains and losses to the intensity of a ray in a differential volume element due to deflection in and out of the ray direction. For particulate materials that are absorbing in nature, an additional loss term arises due to the absorption of intensity within the particle material. For a single particle, the scattering activity is a function of the size and material of the particle. In the case of Mars dust, which has a granite-like composition [60], some regions of the spectrum of interest have strong absorption. As shown in Figure 5.2, the optical properties for montmorillonite as measured by Querry [61] indicate two bands in which strong absorption occurs near wavenumbers of 500 cm^{-1} and 1000 cm^{-1}.

The coefficient of scattering represents the reciprocal of mean free path of light between interactions with scattering particles [62], and behaves the same as the gas absorption coefficient, κ_ν. The last term in Eqn. (5.4), the in-scattering term, is the product of this scattering coefficient and an integral over all incoming radiation multiplied by the scatter-

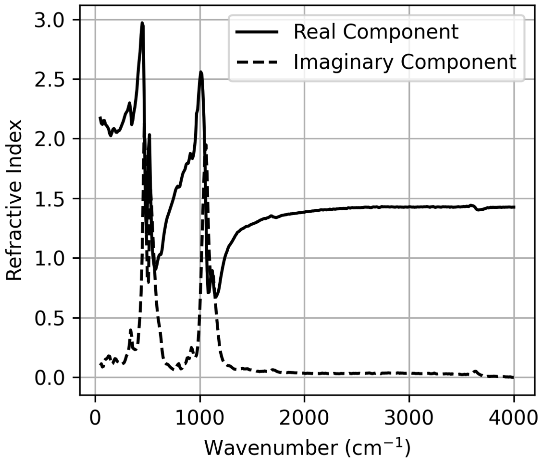

Figure 5.2. Complex index of refraction data for Mars dust analogue material montmorillonite over the wavenumber range of interest.

ing phase function, $\Phi(\Omega, \Omega')$, which is a normalized distribution function that describes the directional favorability of scattering. The scattering coefficient and phase function are complex due to their origination in electromagnetic wave propogation and can require expensive computational techniques for general scenarios. However, for the case of an isolated sphere of constant optical properties subjected to incident plane wave radiation (shown in Figure 5.3), the results can be obtained analytically using the results of Lorenz-Mie theory [63]. The Lorenz-Mie solution produces scattering and extinction (absorption + scattering) efficiency factors for individual particles:

$$Q_{\mathrm{sca},\nu}(r) = \frac{2}{x^2}\sum_{n=1}^{\infty}(2n+1)\left\{|a_n|^2 + |b_n|^2\right\} \tag{5.6a}$$

$$Q_{\mathrm{ext},\nu}(r) = \frac{2}{x^2}\sum_{n=1}^{\infty}(2n+1)\mathrm{Re}(a_n + b_n) \tag{5.6b}$$

where a_n and b_n are complex functions composed of Bessel functions evaluated based on the wavelength nondimensionalized particle diameter [63]. Multiplying the efficiency factors by the cross sectional area and number density of the particles results in the scattering and

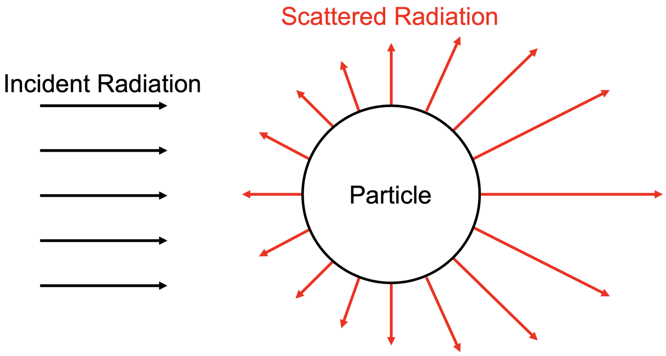

Figure 5.3. Diagram of incident radiation on a small spherical particle being scattered in various directions.

extinction coefficients:

$$\sigma_\nu = \pi r_p^2 n_p Q_{\text{sca},\nu}(r_p), \tag{5.7a}$$

$$\kappa_{\text{ext},\nu} = \pi r_p^2 n_p Q_{\text{ext},\nu}(r_p). \tag{5.7b}$$

Similarly, the rigorous phase function can be found in terms of the complex Lorenz-Mie coefficients, a_n and b_n, though this is not presented here for brevity. Often, approximate phase functions are used as they simplify analysis as compared with the true function. Aside from the isotropic phase function:

$$\Phi(\Omega, \Omega')_{\text{isotropic}} = 1, \tag{5.8}$$

the most commonly used approximation for scattering media is the linear-anisotropic phase function [16]:

$$\Phi(\Omega, \Omega')_{\text{linear-anisotropic}} = 1 + g\mu, \tag{5.9}$$

The value g is the asymmetry factor, which is the average amount of intensity scattered in the forward direction. Values of 0 correspond to an isotropic scattering phase function, and values of +1 and -1 corresponding to forward/backscattering phase functions, respectively.

A rigorous derivation of this quantity using the Lorenz-Mie coefficients is found in Bohren and Huffman [64]. The asymmetry factor is given as follows:

$$g_\nu = 2\sum_{n=1}^{\infty}\left[\frac{n(n+2)}{n+1}\mathrm{Re}(a_n a_{n+1}^* + b_n b_{n+1}^*) + \frac{2n+1}{n(n+1)}\mathrm{Re}(a_n + b_n^*)\right], \tag{5.10}$$

where x^* denotes the complex conjugate. For a cloud of different-sized particles described by a size distribution, $N(r_p)dr_p$, the scattering and extinction coefficients must be integrated over all possible particle sizes. Similarly, the asymmetry factor of the particle cloud is computed by integrating the radius dependent value, $g_\nu(r_p)$ weighted by the size distribution, $N(r_p)dr_p$:

$$\sigma_\nu = \int_0^\infty \pi r^2 Q_{\mathrm{sca},\nu}(r_p)N(r_p)dr_p, \tag{5.11a}$$

$$\kappa_{\mathrm{ext},\nu} = \int_0^\infty \pi r^2 Q_{\mathrm{ext},\nu}(r_p)N(r_p)dr_p, \tag{5.11b}$$

$$g_\nu = \int_0^\infty g_\nu(r_p)N(r_p)dr_p. \tag{5.11c}$$

5.3. RAY TRACING

Ray tracing is a technique in which the radiative flux at a point, given by either Eqn. (5.2) or (5.3), is computed numerically. The intensities for a number of ray orientations are sampled from the sphere/hemisphere of visibility at the point and integrated into flux according to the type of sampling performed. In the current work, the sampling methodology of Johnston and Mazaheri [65] is used. This sampling methodology retains the integration simplicity of a uniform angular grid, while sampling with near uniform solid angle divisions. Johnston and Mazaheri [65] report that this sampling scheme achieves the same accuracy as a uniform grid with a 36% reduction in samples and computational cost. The samples are produced by first dividing the polar angle, ϕ, evenly into N_ϕ points. Next, the number of desired azimuthal points at the equator ($\phi = \pi/2$), $\mathrm{N}_{\theta,\mathrm{max}}$, is modulated by the polar angle position:

$$N_\theta = N_{\theta,\max}\sin\phi. \tag{5.12}$$

Johnston and Mazaheri [65] remark that the value of N_θ is rounded to the nearest integer and a lower limit of 3 is applied. In the current work, The value of ϕ is spaced equally starting at 0 and ending at the maximum value. Because of this, a single azimuthal point is used at the pole ($\phi = 0$). Next, for each angle pair a ray is oriented in cartesian space based on the surface normal orientation:

$$\hat{r} = \cos\phi\hat{n} + \sin\phi\cos\theta\hat{e} + \sin\phi\sin\theta\hat{f}, \tag{5.13}$$

where $\hat{r}$ is the cartesian ray orientation, $\hat{n}$ is the surface unit normal vector, and $\hat{e}$ and $\hat{f}$ are the surface unit tangential vectors as shown in Figure 5.1. Next, the solution and mesh are sampled for each ray, which is clipped to the starting point and any solid surfaces which intersect the ray. Figure 5.4 demonstrates a set of rays cast in the hemisphere of visibility from a point on a representative Mars EDL vehicle backshell point. In Figure 5.4 the gray lines represent rays which traverse the full domain and red lines represent rays which are clipped by other surfaces.

After casting the rays from a surface point, the solution is sampled by testing each cell in the domain for face intersections with the ray. At each of these intersections, the solution state and distance from the ray origin is stored. After finding each cell's intersections, the resulting data is sorted by arc-length along the ray. As testing every cell in the domain is quite inefficient, acceleration is achieved by three techniques. First, the mesh and solution are partitioned in parallel, so that each process has only a subset of the cells to test. Second, an alternating digital tree (ADT) data structure [66] is built with the bounding box for each cell prior to ray tracing, and used to quickly rule out cells which don't intersect the bounding box of the ray. The ADT allows the search space on each mesh partition to be reduced significantly for rays which are nearly oriented to the cartesian axes.

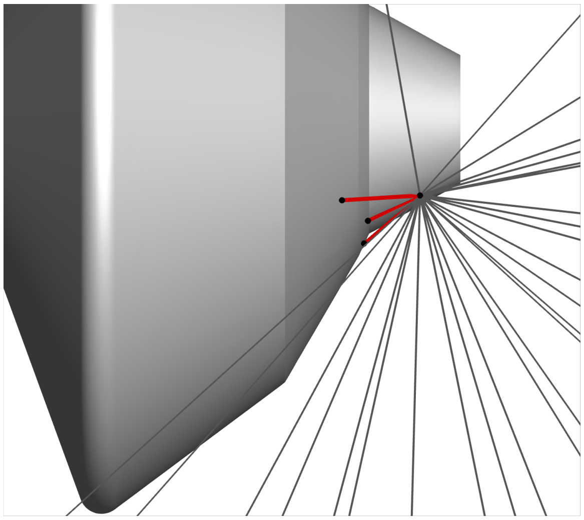

Figure 5.4. Rays cast from a surface location. Gray lines are unbroken, while red lines have visibility of other surface points.

One limitation however is that for rays which are diagonal to the cartesian axes the bounding box can intersect with much of the mesh, reducing the benefit of the ADT. This leads to the third improvement, in which the ray is subdivided into N pieces before using the ADT. As the total bounding box volume of the subdivisions of a diagonal ray are smaller than the unbroken ray's bounding volume, the search set returned from the ADT will be smaller. For the case of a cube domain and a ray which spans the farthest pair of corners of the cube, the search volume by subdividing the ray into N pieces will be 1/N^2 times the domain volume. Using a subdivision count of 100 results in uniform ADT acceleration performance for all ray samples in practice.

After sampling the solution for each ray, the intensity at the integration point is computed by integrating the non-scattering ($\sigma_\nu(s)$) form of Eqn. (5.4) from the farthest point along the ray inward. Assuming an intensity of zero at the starting point and no absorption ($\kappa_\nu(s)$), the ray's intensity is the integral of the emission coefficient ($j_\nu(s)$). For absorbing cases, Eqn. (5.4) is solved using an integrating factor approach [67]. Once the intensity at each ray's origin is computed, the Eqn. (5.3) is solved by integrating first in the azimuthal direction and then the polar direction using trapezoidal rule instead of interpolating the intensity to a uniform $\Delta\theta\Delta\phi$ grid as employed by Johnston and Mazaheri [65]. The naive approach for the discretization of Eqn. (5.3) begins by first separating the integrals:

$$q_\nu(\vec{x}) = \int_0^{\pi/2} \left\{ \int_0^{2\pi} I_\nu(\theta,\phi) d\theta \right\} \cos\phi \sin\phi d\phi. \tag{5.14}$$

In this form, the interior integral can be replaced by a function of the polar angle, ϕ:

$$q_\nu(\vec{x}) = \int_0^{\pi/2} F_\theta(\phi) \cos\phi \sin\phi d\phi, \tag{5.15}$$

where $F_\theta(\phi)$ is the integral of the intensity over the azimuthal direction, evaluated at a given polar angle, ϕ. As the ray orientations are sampled such that groups of rays are given the same polar angle, ϕ, this split-integral form demonstrates that the two angular directions can be treated separately, not requiring a constant $\Delta\theta\Delta\phi$ grid to be employed. In practice, the integrals over the azimuthal angle direction include the $\cos\phi\sin\phi$ term for simpler notation and implementation. The integrals over the azimuthal angle direction are discretized using trapezoidal rule, assuming periodicity at $\theta = 0$ and $\theta = 2\pi$:

$$F_\theta(\phi_i) = \int_0^{2\pi} I_\nu(\theta,\phi_i) \cos\phi \sin\phi d\theta \approx \frac{2\pi}{N_{\theta_i}} \sum_{j=1}^{N_{\theta_i}-1} f(\theta_{i,j},\phi_i) + f(\theta_{i,j+1},\phi_i), \tag{5.16}$$

where $f(\theta,\phi)$ is the integrand, and N_{θ_i} is the number of equally spaced azimuthal angles at polar angle station i:

$$f(\theta,\phi) = I_\nu(\theta,\phi) \cos\phi \sin\phi. \tag{5.17}$$

Next, the flux is computed by integrating the azimuthal integrals:

$$q_\nu(\vec{x}) \approx \frac{\pi}{2N_\phi} \sum_{i=1}^{N_\phi-1} F_\theta(\phi_i) + F_\theta(\phi_{i+1}). \tag{5.18}$$

If the intensity is pre-integrated over the frequency range, then the flux is the total radiative heat flux. Otherwise, the frequency-dependent heat flux must be integrated:

$$q(\vec{x}) = \int_0^\infty q_\nu(\vec{x}) d\nu. \tag{5.19}$$

The previous scheme is consistent and converges to the correct solution, but due to the cosϕsinϕ term in the integrand, a large number of rays is required to resolve the variation over the polar angle, ϕ, even for constant valued intensity distributions. Using the modification suggested by Johnston and Mazaheri [65], in which the integral is treated semi-analytically, reduces the necessary ray count drastically for a given level of accuracy by integrating the cosϕsinϕ term exactly over a given interval. The semi-analytic modification is applied to the present scheme by first computing the azimuthal integral of the intensity alone:

$$F_{\theta,\mathrm{SA}}(\phi_i) = \int_0^{2\pi} I_\nu(\theta,\phi)\mathrm{cos}\phi\mathrm{sin}\phi d\theta \approx \frac{2\pi}{N_{\theta_i}} \sum_{j=1}^{N_{\theta_i}-1} I_\nu(\theta_{i,j},\phi_i) + I_\nu(\theta_{i,j+1},\phi_i). \tag{5.20}$$

Next, the integral over the polar angle, ϕ, is computed analytically between two polar angles assuming a constant azimuthally integrated intensity equal to the average over the polar angle interval:

$$\int_{\phi_i}^{\phi_{i+1}} F_{\theta,\mathrm{SA}}(\phi)\mathrm{cos}\phi\mathrm{sin}\phi d\phi \approx \bar{F}_{\theta,\mathrm{SA}}(\phi_{i+1/2}) \int_{\phi_i}^{\phi_{i+1}} \mathrm{cos}\phi\mathrm{sin}\phi d\phi, \tag{5.21}$$

where $\bar{F}_{\theta,\mathrm{SA}}(\phi_{i+1/2})$ is the average of the azimuthal integrals at polar angles ϕ_i and ϕ_{i+1}:

$$\bar{F}_{\theta,\mathrm{SA}}(\phi_{i+1/2}) \approx \frac{1}{2}\left[F_{\theta,\mathrm{SA}}(\phi_i) + F_{\theta,\mathrm{SA}}(\phi_{i+1})\right]. \tag{5.22}$$

Solving the approximate polar angle integral exactly and inserting into Eqn. (5.18) yields the semi-analytic ray tracing angular flux integration scheme:

$$q_\nu(\vec{x}) \approx \frac{1}{4} \sum_{i=1}^{N_\phi - 1} \bar{F}_{\theta,\mathrm{SA}}(\phi_{i+1/2}) \left(\cos(2\phi_i) - \cos(2\phi_{i+1})\right). \tag{5.23}$$

The modified scheme was found to provide convergence to within 1% of highly refined solutions with ray counts as small as 50, as opposed to 400-500 in the case of the naive scheme which discretizes the $\cos\phi\sin\phi$ term. Both schemes achieve second-order accuracy with angular resolution, though the semi-analytic scheme shifts the error down drastically.

5.4. THE P$_1$ APPROXIMATION

The P$_1$ approximation is a technique for solving the PDE form of the RTE using spherical harmonics to represent the angular dependence of the intensity. The PDE form of the RTE is written as follows (dropping ν subscripts for brevity):

$$\hat{s} \cdot \nabla I(\vec{x}, \hat{s}) + (\kappa + \sigma) I(\vec{x}, \hat{s}) = j + \frac{\sigma}{4\pi} \int_{4\pi} I(\hat{s}') \Phi(\hat{s} \cdot \hat{s}') d\Omega'. \tag{5.24}$$

In Eqn. (5.24), $\hat{s}$ is a unit vector for the line of sight direction, while $\hat{s}'$ is an incoming line of sight direction corresponding to the differential solid angle $d\Omega'$. Eqn. (5.24) is equivalent to Eqn. (5.4) except that the derivative of intensity is now a gradient of intensity. This form of the PDE is thus solved simultaneously across space for a given line of sight direction, $\hat{s}$. In the non-scattering case, Eqn. (5.24) can be solved for individual line of sight directions as there is no coupling between differing lines of sight. For the scattering case, however, the coupling introduced by the in-scattering term complicates the solution process. A number of techniques exist for solving this coupled system, but the two most common are the discrete ordinates method (DOM), and the spherical harmonics method [15, 16]. In DOM techniques, a discrete set of ray orientations are selected and the intensity field for each direction is solved. The in-scattering term as well as radiative flux are computed as a quadrature of the intensity over all lines of sight in the system [15]. A variant of the technique, the finite angle method [68], replaces the quadrature with control volumes over space and direction. DOM-type methods can treat complicated radiation scenarios without added complexity, including detailed scattering phase functions that arise from Lorentz-Mie theory, though Modest and Mazumder [15] remark that a phenomenon called the ray-effect can occur. The ray-effect is a solution deficiency in which emission from distant regions is represented poorly by coarse angular discretizations, leading to visible and unphysical oscillations in the flux throughout the domain. Furthermore, for highly scattering media DOM-type methods can become expensive due to the strong coupling between different directions introduced through the in-scattering term [15].

Spherical harmonics methods utilize an expansion of the Intensity as a series of spherical harmonics basis functions:

$$I(\vec{x}, \hat{s}) = \sum_{l=0}^{\infty} \sum_{m=-l}^{l} I_l^m(\vec{x}) Y_l^m(\hat{s}), \tag{5.25}$$

where $Y_l^m(\hat{s})$ are spherical harmonics, which satisfy Laplace's equation in spherical coordinates [15]. This expansion, when used with Eqn. (5.24) results in an infinite number of coupled, elliptic PDEs. In practice, the intensity expansion is truncted to a maximum of N, which yields $(N+1)^2$ coupled PDEs. A spherical harmonics approximation of order N is referred to as the P_N method. As the number of equations and required boundary conditions expands rapidly with increasing N, it is rare that anything higher than P_3 is used except in one-dimensional problems. The most commonly used form, however, is the P_1 approximation due to its cost and simplicity. When truncated to $N = 1$, the intensity can be represented as a function of only coordinates of space [15]:

$$I(\vec{x}, \hat{s}) \approx a(\vec{x}) + \mathbf{b}(\vec{x}) \cdot \hat{s}. \tag{5.26}$$

Modest and Mazumder [15] show that when used in the definition of the incident radiation at a point,

$$G(\vec{(x)}) = \int_{4\pi} I(\vec{x}, \hat{s}) d\Omega \approx 4\pi a(\vec{x}), \tag{5.27}$$

and the radiative flux at a point,

$$\mathbf{q}(\vec{x}) = \int_{4\pi} I(\vec{x}, \hat{s}) \hat{s} d\Omega \approx \frac{4\pi}{3} \mathbf{b}(\vec{x}), \tag{5.28}$$

the intensity at a point can be represented as follows:

$$I(\vec{x}, \hat{s}) = \frac{1}{4\pi} \left[G(\vec{x}) + 3\mathbf{q}(\vec{x}) \cdot \hat{s} \right]. \tag{5.29}$$

Using Eqns. (5.27-5.29) in Eqn. (5.24) and performing some manipulation, a Helmholtz equation for the incident radiation can be derived [15]:

$$\nabla \cdot \left(\frac{3}{3\beta - g\sigma} \nabla G \right) = -3(4\pi j - \kappa G). \tag{5.30}$$

Quantities of interest, such as the radiative flux and divergence of radiative flux are computed as functions of the solution variable, G. The gradient of the solution variable, G, which is the incident radiation at a point, can be related to the radiative flux as follows:

$$\mathbf{q}(\vec{x}) = \frac{-1}{3\beta - g\sigma} \nabla G, \tag{5.31}$$

while the divergence of radiative flux is written:

$$\nabla \cdot \mathbf{q}(\vec{x}) = j - \kappa G. \tag{5.32}$$

On the domain boundaries, it is necessary to specify the radiative intensity entering the domain. Of the various boundary conditions possible, Marshak's boundary, which is most commonly employed in practice [15], is used in the current study. Marshak's boundary specifies that the normal gradient of the incident radiation on the boundary is balanced by the difference of the incident radiation and radiative intensity emitted by the surface:

$$\frac{\epsilon - 2}{\epsilon} \frac{2}{3\beta - g\sigma} \hat{n} \cdot \nabla G + G = 4\pi I_b(T_{\text{wall}}). \tag{5.33}$$

In Eqn. (5.33), ϵ is the surface emissivity, while $I_b(T_{\text{wall}})$ is the Planck black-body function evaluated at the surface temperature.

Eqn. (5.30) demonstrates the major advantage of the P_1 approximation, which is the full determination of the radiation field using a single elliptic PDE. It is important to note however that the P_1 approximation is not perfect in all scenarios. Modest and Mazumder [15] remark that for problems involving optically thick hot participating media, the P_1 approximation can fail to recover the optically thick limit. Additionally the P_1 approximation can be inaccurate in scenarios with highly directional radiation sources propagating through an optically thin medium, such as collimated radiation [15]. Similarly, distant emission sources in optically thin scenarios can be represented inaccurately due to low directional resolution of the intensity field. Andrienko and Surzhikov [69] demonstrate that reasonable accuracy can be obtained for spacecraft radiative heating problems as long as a minimum absorption coefficient is enforced through the domain for numerical stability. Hartung and Hassan [70] also show good agreement with state of the art techniques when applying the P_1 method to shock-layer radiation transport.

5.5. IMPLEMENTATION AND VERIFICATION OF THE P$_1$ RADIATION SOLVER

In the current work, the primary radiation transport tool is a continuum radiation solver based on the P$_1$ approximation. The P$_1$ radiation solver was implemented within HyperSolve [54]. For the P$_1$ radiation solver, Eqn. 5.30, is discretized using the edge-based finite volume method similar to the continuum particle solver described in Section 4. In this section, some implementation details for the P$_1$ radiation solver are given, such as equation normalization and discretizatin, after which solver verification efforts are presented.

5.5.1. Normalization. For numerical stability, it is necessary to normalize the equation due to the form of the pseudo-diffusion coefficient which appears in Eqn. (5.30):

$$\frac{3}{3\beta - g\sigma}. \tag{5.34}$$

For the non-scattering case ($\sigma = 0$), it is clear that for absorption coefficient magnitude can grow quite large for small values of β. Hartung and Hassan [70] remark that due to the large disparities in the values of the absorption and emission across the spectrum, numerical conditioning can vary wildly for different frequencies. Hartung and Hassan [70] proposed a transformation of the incident intensity, G, by dividing by the product of the average values of spectral absorption and emission coefficients through the domain:

$$\Gamma = \frac{G}{\bar{j}_\nu \bar{\kappa}_\nu}. \tag{5.35}$$

The average values of the spectral absorption and emission coefficients in the domain are defined [70] as:

$$\bar{\kappa}_\nu = \frac{1}{N_{\mathrm{DOF}}} \sum_{i=1}^{N_{\mathrm{DOF}}} \kappa_\nu(\vec{x}_i) \tag{5.36a}$$

$$\bar{j}_\nu = \frac{1}{N_{\mathrm{DOF}}} \sum_{i=1}^{N_{\mathrm{DOF}}} j_\nu(\vec{x}_i) \tag{5.36b}$$

From here out the frequency dependence of Eqn. (5.36) is assumed and frequency subscripts are dropped. Multiplying G in Eqn. (5.30) by $\bar{\kappa}/\bar{\kappa}$, and both sides of the PDE are multiplied by the average emission, $\bar{j}$. After simplifying, the following transformed PDE is found:

$$\nabla \cdot \left(\frac{3\bar{\kappa}}{3\beta - g\sigma} \nabla \cdot \Gamma \right) = -3 \left(4\pi \frac{j}{\bar{j}} - \kappa\bar{\kappa}\Gamma \right). \tag{5.37}$$

5.5.2. Discretization. To discretize Eqn. (5.30) using the finite volume method, it is necessary to transform the PDE to an integral form. Integrating Eqn. (5.30) over a volume, $\mathcal{V}$, and applying Gauss' Divergence theorem, the integral form is written:

$$\int_S \frac{3}{3\beta - g\sigma} \nabla G \cdot d\mathbf{S} - 3 \int_{\mathcal{V}} 4\pi j - \kappa G d\mathcal{V} = 0 \tag{5.38}$$

As the problem is elliptic and linear, a central scheme is applied to compute the flux at each interface. The intensity value at a face is simply the average of the two nodes which share the interface:

$$G_{\text{face}} = \frac{1}{2} \left(G_L + G_R \right), \tag{5.39}$$

where G_L and G_R are the intensity values on the 'left' and 'right' nodes sharing the face. Solution reconstuction is performed using a quadratically accurate least squares (QLSQ) gradient.

5.5.3. Method of Manufactured Solutions Verification. To verify that design order of accuracy is achieved by the P_1 radiation solver, the method of manufactured solutions (MMS) was utilized. MMS is a technique for generating pseudo-exact solutions to PDEs on arbitrary domains or when exact solutions are not available. The MMS process works by beginning with an assumed, or manufactured, solution to a PDE, and computing the residual based on it. As the manufactured solution does not necessarily satisfy the PDE, a non-zero residual is obtained. The negative of this non-zero residual is then imposed as an additional source term to the solver, such that in the limit of discretization the manufactured solution will be obtained numerically. By comparing against the exact manufacured solution, the discretization error and observed order of accuracy of the solver can be directly measured. Many, though not all, implementation errors in the solver can be detected by comparing the observed order of accuracy to the design order. Well designed manufactured solutions will be functions which cannot be represented exactly by the discretization, and which result in an MMS source contribution for every term in the PDE. For the P_1 approximation, the following manufactured solution was used:

$$G_{\mathrm{MMS}} = 7xyz + 8x^2yz + 9xy^2z + 10xyz^2. \tag{5.40}$$

When substituted into Eqn. (5.30), the following MMS source function is obtained:

$$\begin{aligned} S_{\mathrm{MMS}} &= 3\left[4\pi j - \kappa(7xyz + 8x^2yz + 9xy^2z + 10xyz^2)\right] \\ &+ \frac{1}{\kappa}(20xy + 18xz + 16yz). \end{aligned} \tag{5.41}$$

Injection of Eqn. (5.41) as a source term for the solver then results in a numerical approximation to Eqn. (5.40) and a means to measure the discretization error on the given mesh as discussed above. To limit the test to the interior discretization, the boundary values are set to the MMS solution using Eqn. (5.40) as a dirichlet condition.

MMS was performed on a cube domain with the minimum and maximum values along each coordinate are 0 and 1, respectively. Grids of sizes 5 × 5 × 5, 10 × 10 × 10, 20 × 20 × 20, and 40 × 40 × 40 were used, with each hexahedral cell being split into tetrahedra. A linear least squares (LLSQ) variable reconstruction was used, which should yield a design order of accuracy of 2 on tetrahedral meshes. Figure 5.5 demonstrates that the radiation solver recovers the manufactured solution given by Eqn. (5.40) at the design order of accuracy. It is important to note that MMS is a powerful tool, but not able to detect all problems. The Marshak boundary, given by Eqn. (5.33), is not able to be tested using the Manufactured solution given by Eqn. (5.40).

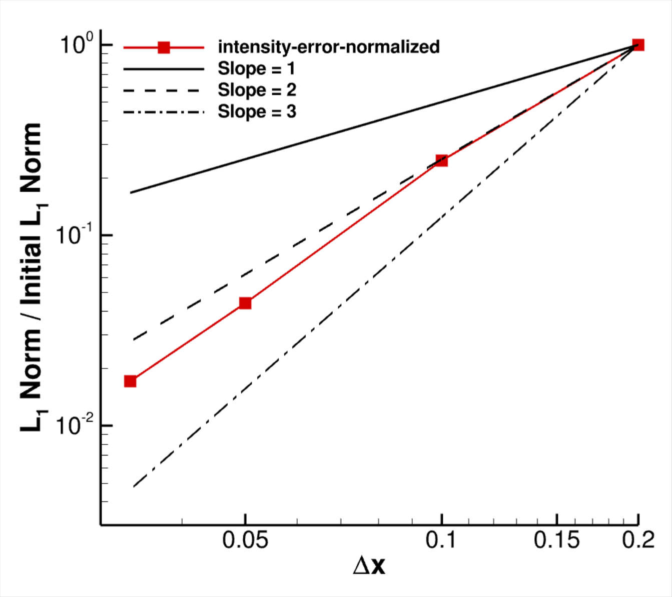

Figure 5.5. Normalized L_1 error history with grid refinement for the MMS verification.

5.5.4. Verification: Plane-Parallel Isothermal Medium. For this case, the radiation transport between two infinite parallel plates with an constant property isothermal medium was solved using the P_1 radiation solver. As this scenario yields a one-dimensional solution, both the Marshak and symmetry boundary conditions are tested. The exact solution to Eqn. (5.30) for this case is presented by [15]: The expression for the incident intensity, G, is given as:

$$G(\tau) = 4\sigma T^4 - 4\left(T^4 - T_w^4\right)\left[\frac{\cosh\gamma\tau}{\cosh\frac{1}{2}\gamma\tau_L + 2\sqrt{\frac{1-\omega}{3-A_1\omega}}\sinh\frac{1}{2}\gamma\tau_L}\right], \tag{5.42}$$

where τ is the optical thickness at a point between the plates, and tau_L is half the optical thickness between the plates spaced a distance L apart, and γ is defined as follows:

$$\gamma = \sqrt{(1-\omega)(3-A_1\omega)} \tag{5.43}$$

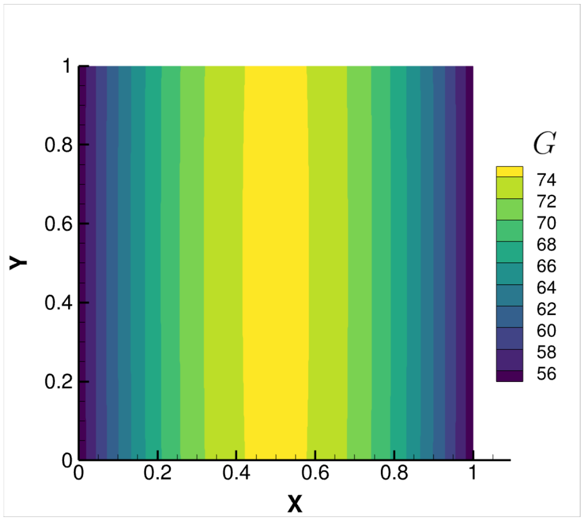

Figure 5.6. Contours of incident intensity, G, between parallel plates for an isothermal medium of temperature, T.

It is important to note that Eqn. (5.42) is an exact solution to Eqn. (5.30), but not necessarily Eqn. (5.4) as the P_1 approximation truncates the spherical harmonics expansion of the intensity. Modest and Mazumder [15] demonstrate that when compared to the exact solution of Eqn. (5.4) for this case, the P_1 approximation agrees well in the optically thin limit ($\tau \longrightarrow 0$) but disagrees in the optically thick limit ($\tau \longrightarrow \infty$).

Using an absorption and emission coefficient value of 1 and 10, respectively, Figure 5.6 shows the incident intensity, G, solution computed using the radiation solver. The MMS verification demonstrated second-order accuracy in the interior scheme, but when using the Marshak boundary condition the error becomes dominated by the boundary. Using a linearly accurate gradient results in a reduction to first order globally due to the direct presence of the gradient in Eqn. (5.33). Instead, for this case a quadratically accurate least squares (QLSQ) gradient was used to maintain second-order accuracy due to the appearance of the gradient in the Marshak boundary condition.

5.5.5. Comparison with the Tangent Slab Technique. It is important to note that for the scattering radiation problems of interest in the current study, only the difference between the scattering and non-scattering solution is desired. By taking the difference

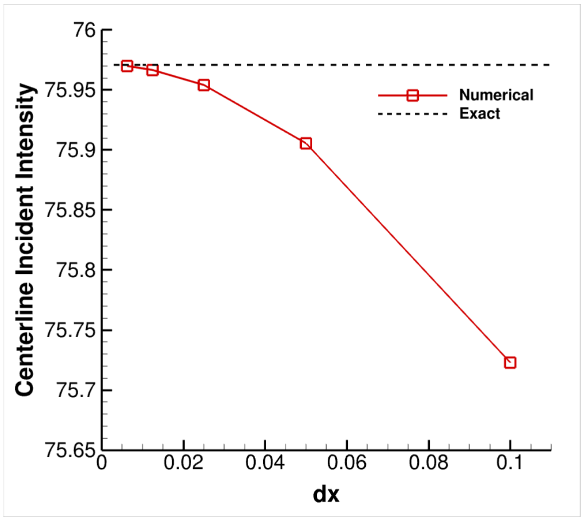

Figure 5.7. Comparison of the radiation solver with Eqn. (5.42) evaluated at the midpoint between the plates.

between the scattering and non-scattering solution, an estimate of the impact of scattering is yielded. Still, the P_1 radiation solver was compared to a reference technique for gas-only radiation transport in order to determine the agreement at conditions relevant to the current study. The reference technique used to compare the P_1 radiation solver is the tangent slab technique. The tangent slab technique is a method for computing three dimensional radiation transport approximately by simplifying the problem to a series of one dimensional plane-parallel radiation problems. To compute the radiative heat flux at a point on a surface, the flow field is sampled along the line normal to the body to produce the properties for a plane-parallel radiation problem. The plane-parallel assumption allows the radiation transport to be solved pseudo-analytically for varying optical properties within the plane layer. The technique and the derivation of expressions for radiative heat flux are described in Refs. [71, 72]. The tangent slab technique is commonly used in hypersonic atmospheric entry heating problems as it is computationaly inexpensive and accurate in the vehicle forebody region [65]. The heat flux at a surface point using the tangent slab technique is expressed as:

$$q_{w,\mathrm{rad}} = 2\pi \int_0^{s_{\max}} j(z) \frac{d}{d\tau} \left\{ E_3 \left[\tau(z) - \tau(s) \right] \right\} dz, \tag{5.44}$$

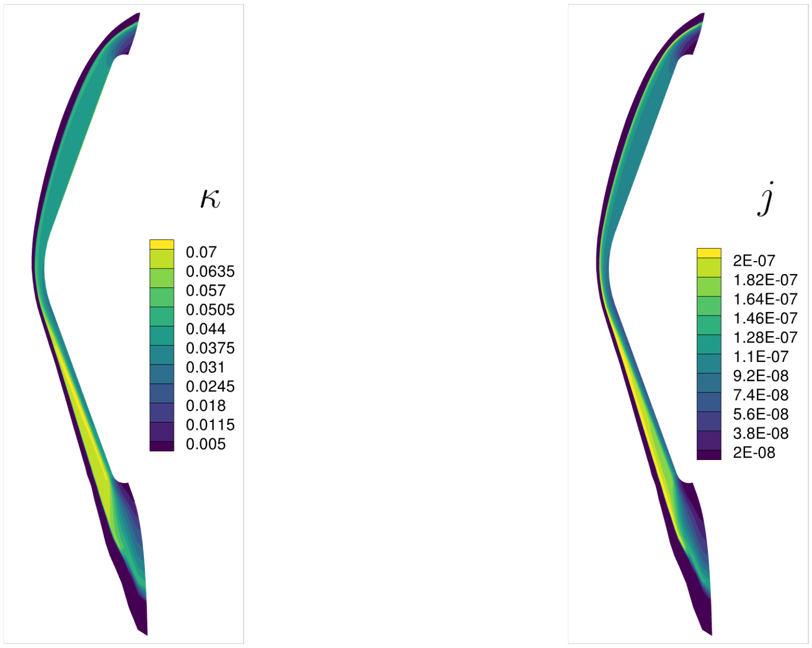

(a) Absorption (cm^{-1})

(b) Emission ($\mathrm{erg\ s^{-1}\ cm^{-3}\ sr^{-1}\ Hz^{-1}}$)

Figure 5.8. Optical coefficients at wavenumber of 2200 cm^{-1} along the symmetry plane of the Mars 2020 shock layer.

where z is the distance along the surface normal vector, $j(z)$ is the emission coefficient, and $E_3(x)$ is the third order exponential integral. Recall that τ is the optical thickness defined by Eqn. (5.5). The tangent slab technique is implemented by first sampling the gas solution or optical coefficients along a line normal to a surface location, and then computing the radiative heat flux using Eqn. (5.44).

As a testcase, the Mars 2020 82 second trajectory point is considered [73]. Spectral optical coefficients are computed with the HARA radiation code [74] and used in both the P_1 radiation solver and the tangent slab technique. Figure 5.8 shows the optical coefficients at a wavenumber of 2200 cm^{-1} for this case. The normalized heat flux computed with both P_1 approximation and tangent slab approaches is compared in Figure 5.9. Both solutions were normalized by the tangent slab solution at the vehicle nose. The P_1 approximation solution was found to overpredict the tangent slab solution, with the largest overprediction occuring at the spherical nose cap portion of the surface. Over much of the surface, the

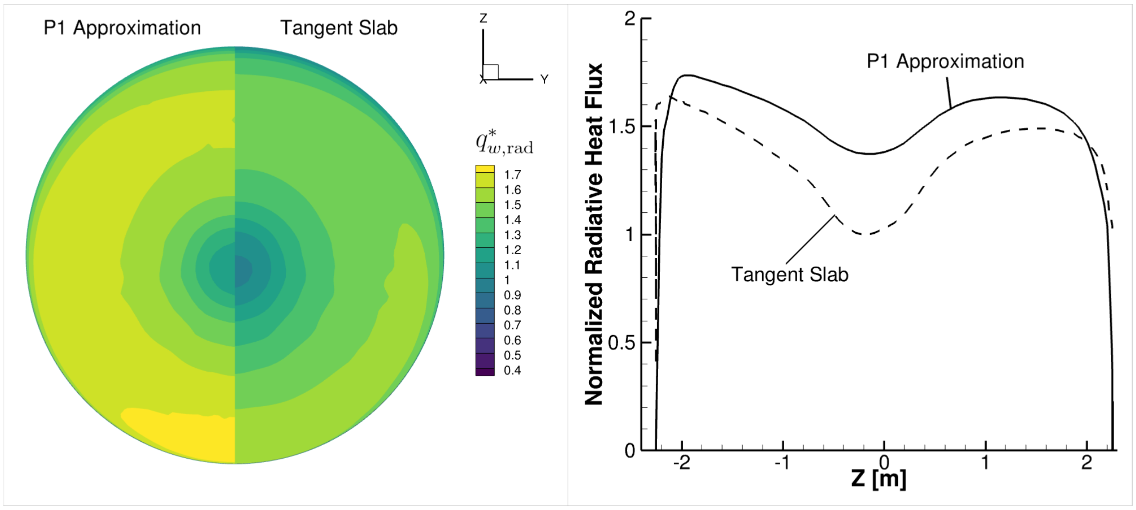

(a) Surface Contours (b) Symmetry Plane

Figure 5.9. Comparison of the P_1 approximation and tangent slab results for the Mars 2020 case.

P_1 approximation solution agrees with the tangent slab solution to within 20%, indicating that the technique is suitable for use in the current work. As a constant intensity boundary condition was imposed on the artificial outflow boundary separating the forebody from the wake region, the radiative heating deviates more rapidly from the tangent slab solution at the edge of the shoulder. Figure 5.10 shows the percent relative error between the solutions. To assess the average error over the surface without the outflow boundary affecting the results, a weighted average error was computed. The weighted average is computed as:

$$\bar{q}_{w,v} = \frac{\int_S q_{w,v} E \, dS}{\int_S q_{w,v} \, dS} \tag{5.45}$$

where E is the percent relative error in the solutions. The weighted average of the percent relative error over the surface is 8.85%.

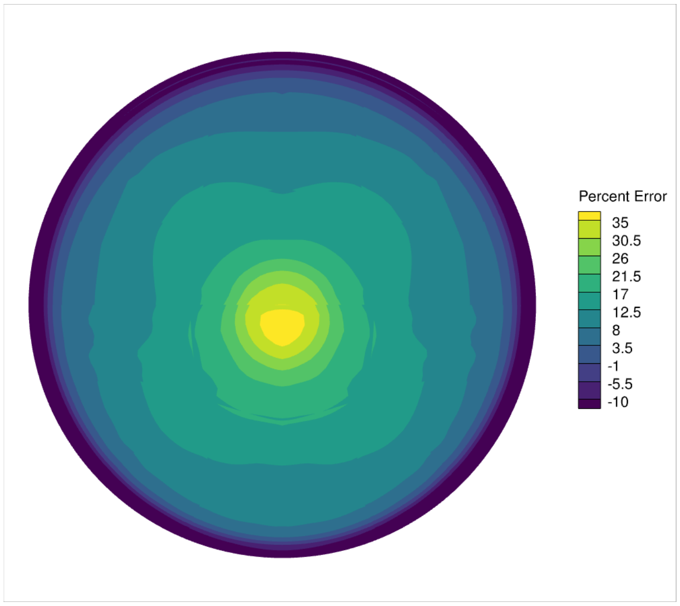

Figure 5.10. Relative percent difference between the P_1 approximation and tangent slab solutions.

6. RESULTS AND DISCUSSION

In this chapter, the results of the dissertation are presented in three sections. In Sec. 6.1, the TCV method is applied to the prediction of surface erosion in dusty Mars entry. The TCV results are verified against Monte Carlo solutions, and the convergence properties of both methods are demonstrated. After determining the optimal particle sample count for the TCV method, the erosion for a vehicle at angle of attack is predicted for a full trajectory and uncertainty quanitifcation techniques are applied to the problem. In Sec. 6.2, the volumetric TCV method extended to two-way coupled analysis is applied to a series of verification cases. The approach is then validated against a dusty shock tube experiment and then applied to a Mars entry case to determine the degree of coupling in flight through global dust storm conditions. Lastly, in Sec. 6.3, a survey of gas-particle radiative interaction mechanisms is studied to investigate the effect of dust conditions on the radiative heating experienced by vehicles is presented. The effects of black-body radiation by shock-heated particles and scattering of gas-phase radiation are studied for Mars entry, while the potential of emission augmentation by haze particle vaporization in Titan entry is investigated.

6.1. SURFACE EROSION PREDICTION IN MARS ENTRY

In this section, analysis of surface erosion due to dust impacts in Mars entry is presented. A Lagrangian particle solver was used with both the TCV and MC methods to predict erosion rates in Mars entry during a global dust storm scenario. Verification of the TCV method is presented, in addition to comparison with results from literature. The cumulative surface erosion on a representative Mars entry vehicle at varying angle of attack is presented, as well uncertainty quantification and global nonlinear sensitivity analysis.

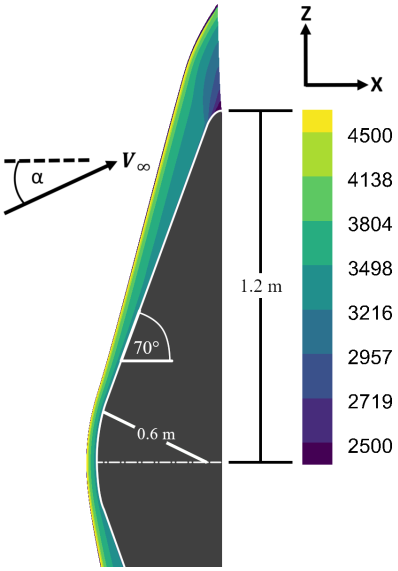

Figure 6.1. Schiaparelli capsule forebody geometry and an example shock-layer temperature (K) solution at the conditions for trajectory point 4 given in Table 6.1.

6.1.1. Description of the Problem.

To determine the efficiency of the TCV method, the technique was applied to a representative Mars entry problem from the literature. The ExoMars case of Palmer et al. [10] was selected for comparison with the results of the developed methodology. Figure 6.1 demonstrates the ExoMars Schiaparelli vehicle geometry used in this analysis. Table 6.1 lists the trajectory conditions considered in the current work, which are based on Refs. [10, 75]. Similar to Ref. [10], the dust conditions were based on the July 2007 global dust storm measured by the Mars Reconnaissance Orbiter (MRO) [10, 76] [1].

The gas phase was modeled with the NASA LAURA CFD solver [34, 78] using a two-temperature thermochemical non-equilibrium model consisting of 8 species: CO_2, N_2, CO, NO, O_2, C, N, O. The atmospheric composition was assumed to be 97% CO_2, and 3% N_2 without dependence on altitude. A laminar steady flow assumption was made with a fully-catalytic no-slip wall, with surface temperatures described by enforcing a radiative adiabatic wall condition. A grid consisting of approximately 5×10^5 cells was used for the

---

[1] The exact conditions considered in this study are contained in MRO Dataset ‘2007071800_DDR’ [76, 77]

Table 6.1. Listing of flight conditions for the trajectory points given by Gulhan et al. [75] and Palmer et al. [10].

Altitude [km]	ρ_∞ [kg/m^3]	U$_\infty$ [m/s]	T$_\infty$ [K]	α [deg]
50.0	1.755x10^{-4}	5500.6	171.8	7.2
45.0	2.944x10^{-4}	5185.0	175.0	7.2
40.0	4.825x10^{-4}	4689.0	182.4	7.2
35.0	7.717x10^{-4}	4016.9	186.3	7.2
30.0	1.322x10^{-3}	2913.7	190.1	6.0
28.2	1.542x10^{-3}	2595.4	191.6	5.8
25.5	1.979x10^{-3}	2013.8	195.4	5.0
23.1	2.440x10^{-3}	1570.6	199.1	4.2
20.9	2.962x10^{-3}	1236.9	202.3	3.0
18.9	3.478x10^{-3}	1001.9	205.8	3.0

ExoMars forebody geometry with an O-H topology in the nose region, and a convergence study was performed previously to ensure that the CFD solution was sufficiently resolved [46].

6.1.2. Determination of the Surface Particle Impact Rate. As mentioned in Section 3, the freestream particle encounter rate is necessary for the determination of the surface impact rate. To compute the particle encounter rate, information about the size distribution of the particle phase, $n(r_p)$, is needed. In this study, the modified gamma distribution presented by Toon et al. [60] was used to describe the dust environment for Mars. As discussed by Palmer et al. [10], it was assumed that this distribution is constant with altitude and only the total quantity of dust varied. The distribution is written as

$$n(r_p) = Cr_p^2 \exp\left[-4(r_p/r_m)^{1/2}\right], \tag{6.1}$$

where r_p is the radius of a particle in μm. The free parameters, C, and r$_m$, are tuning parameters which are used to adjust the total number of particles and most frequent particle size to observations, respectively. From the size distribution function, it is possible to define the mass fraction function of the particles:

$$X(r_p) = \frac{m_p(r_p)n(r_p)}{\int_0^\infty m_p(r_p)n(r_p)dr_p}, \tag{6.2}$$

where $m_p(r_p)$ is the mass of a particle of radius r_p. While the particle mass can be treated generally, particles were assumed to be spherical in the current work, ρ_p, allowing for the following expression for particle mass to be used:

$$m_p(r_p) = \frac{4}{3}\pi\rho_p r_p^3. \tag{6.3}$$

Substituting Eqn. (6.3) in to Eqn. (6.2) results in the following:

$$X(r_p) = \frac{r_p^3 n(r_p)}{\int_0^\infty r_p^3 n(r_p)dr_p} = \frac{r_p^5 \exp\left[-4(r_p/r_m)^{1/2}\right]}{\int_0^\infty r_p^5 \exp\left[-4(r_p/r_m)^{1/2}\right]dr_p}. \tag{6.4}$$

Substituting Eqn. (6.1) in to Eqn. (6.4) and representing the denomenator integral as the total mass parameter, T_M, the following expression results:

$$X(r_p) = \frac{r_p^5}{T_M} exp\left[-4(r_p/r_m)^{1/2}\right], \tag{6.5}$$

For the assumed size distribution of Eqn. (6.1), the total mass parameter was evaluated exactly [79], resulting in the simple function of modal radius given in Eqn. (6.6). The mass fraction function for various modal radii is shown in Figure 6.2, using Eqns. (6.5) and (6.6).

$$T_M = \frac{155925 r_m^6}{32768} \approx 4.758453 r_m^6. \tag{6.6}$$

As suggested by Palmer et al. [10], the mass mixing ratio, q, was used to relate the densities of the gas and particle phases. The mass mixing ratio is defined as:

$$q = \frac{\int_0^\infty m_p(r_p)n(r_p)dr_p}{\rho_\infty}. \tag{6.7}$$

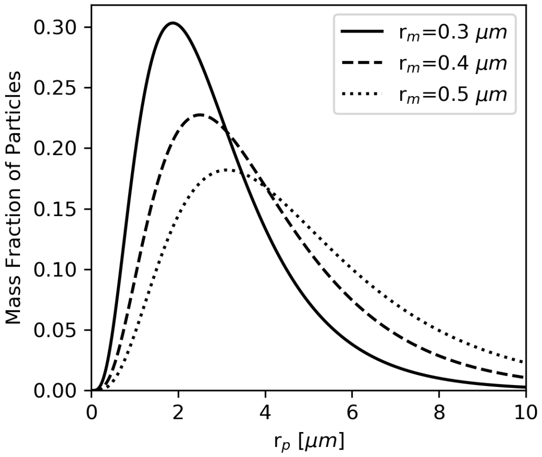

Figure 6.2. Mass fraction functions for various modal radii, r$_m$.

By integrating the mass of gas encountered by a unit of area over a range of time, t, the number of particles encountered per unit area over that range of time is found. Assuming no variation of the particle composition or size distribution with altitude, the differential number of particles encountered from time t to $t + dt$ is found by integrating the particle phase density by mass of an individual particle, weighted by the mass fraction function:

$$\Delta N_\infty(r_p) = \frac{qX(r_p)}{m_p(r_p)} \int_t^{t+\Delta t} \rho_\infty V_\infty dt. \tag{6.8}$$

Assuming the flow to be quasi-steady, the freestream conditions can be moved out of the integral and solved:

$$\Delta N_\infty(r_p) = \frac{qX(r_p)\rho_\infty V_\infty}{m_p(r_p)} \Delta t. \tag{6.9}$$

Dividing by Δt and taking the limit as $\Delta t \rightarrow 0$ results in the rate of particles of radius r_p encountered per unit area upstream of the shock layer:

$$\dot{N}_\infty(r_p) = \frac{d}{dt}\left[N_\infty(r_p)\right] = \frac{qX(r_p)\rho_\infty V_\infty}{m_p(r_p)}. \tag{6.10}$$

Mathematically, Eqn. (6.10) is equivalent to the product of Eqn. (6.1) and the flight velocity, V_∞, though the unknown constant, C, must be determined. Equation (6.10) is advantageous as it is in terms of easily measured quantities like the flight conditions and mass loading ratio, q. By setting Eqn. (6.10) equal to the product of Eqn. (6.1) and V_∞, it can be shown that C can be expressed using similar quantities:

$$C = \frac{3q\rho_\infty}{4\pi T_M \rho_p}. \tag{6.11}$$

As an aside, the modified gamma distribution in Eqn. (6.5) can be represented with generalized shape parameters:

$$X(r_p) = \frac{r_p^{3+\alpha}}{T_M} \exp\left[-\left(\frac{\alpha}{\gamma}\right)\left(\frac{r_p}{r_m}\right)^\gamma\right], \tag{6.12}$$

allowing the shape of the distribution to be tailored to measurements. Tomasko et al. [80] compare a collection of shape parameters from various sources and discuss their relevance to measurements from the Mars Pathfinder vehicle. Similar to above, the total mass parameter, T_M, can be computed analytically for a given modal radius, r_m, as follows:

$$T_M = r_m^{4+\alpha} \left[\frac{\Gamma(\frac{4+\alpha}{\gamma})}{\gamma\left(\frac{\alpha}{\gamma}\right)^{\frac{4+\alpha}{\gamma}}}\right], \tag{6.13}$$

where Γ is the gamma function.

6.1.3. Surface Erosion Modeling. To compute surface erosion over the surface, the dilation factor for each TCV was first computed for a given particle radius, r_p, using the methodology described in Sec. 3.2. The surface impact rate was computed by multiplying the dilation factorby the particle encounter rate, $\dot{N}_\infty(r_p)$, given in Eqn. (6.10).

The crater volume resulting from a single particle impact was modeled using the correlation developed for Norcoat-Liege, which is the TPS material used on the ExoMars Schiaparelli vehicle [81]. The crater model is given as follows:

$$\text{Ꝟ}_c = \frac{2}{3}\pi\cos(\theta)\left[0.00028\rho_p^{0.62}d_p^{1.04867}v_p^{0.667}\right]^3, \tag{6.14}$$

where $\cos\theta$ is a term which accounts for the effect of sequential impacts where material may have already been removed. The angle factor, θ, was given a value of 45° following the discussion in [10]. The total erosion at a location, $\dot{Z}_T$, is found multiplying Eqn. (6.14) by the impact particle flux, $\dot{N}(r_p)$, and integrating over all particles sizes:

$$\dot{Z}_T = \int_0^\infty \dot{Z}(r_p)dr_p = \int_0^\infty \dot{N}(r_P)\text{Ꝟ}_c(r_p)dr_p. \tag{6.15}$$

As no analytical function for the recession rate is available in practice, the integration over all particle sizes in Eqn. (6.15) must be performed numerically. Various approaches for this integration have been found in the literature, such as binning and the trapezoidal rule. In the binning approach, a finite interval of the particle radius is selected and split into sub-intervals, after which the average particle size on the interval is used to evaluate the erosion. The sum of these averages weighted by the fraction of particles that fall within that sub-interval is used to approximate the integral [10]. For the trapezoidal rule approach, the integral is approximated by assuming a piecewise linear representation of the function and integrating exactly:

$$\int_a^b f(x)dx \approx \frac{1}{2}\sum_{k=1}^{N}\left(x_k - x_{k-1}\right)\left(f(x_{k-1}) + f(x_k)\right). \tag{6.16}$$

For the work related to dust erosion studies in this dissertation, trapezoidal integration was used by considerting a total of 50 radii in the range of 0.75 to 10 microns.

6.1.4. Surface Erosion Prediction with a Monte Carlo Approach. As a contrast to the TCV method, with the Monte Carlo approach, surface erosion solution requires the simulation of a large number of particles and the accumulation of their effects over each cell of a surface grid. The Monte Carlo (MC) approach starts with initializing a large number of particles with random position on the freestream boundary of the CFD domain. Each of these particles is traced through the shock layer, and their impact crater volume is computed based on their conditions at impact, if applicable. These crater volumes are summed over each face of a surface grid, and subsequently divided by the face area and a physical time corresponding to the total number of particles simulated and the upstream dust and gas environment. For the initialization step, a 'seed volume', ($\forall_{seed}$) is defined based on a given time (t_{seed}), the flight velocity (V_∞) and the bounding area (A_b) of the vehicle in the flow direction:

$$\forall_{seed} = t_{seed} V_\infty A_b. \tag{6.17}$$

The number of particles simulated, N_{MC}, corresponding to the chosen time range, t_{seed}, is then found by multiplying the seed volume by the number density of a monodisperse cloud of particles with radius r_p:

$$N_{MC} = \frac{3q\rho_\infty \forall_{seed}}{4\pi\rho_p r_p^3}. \tag{6.18}$$

This number of particles is rounded to the nearest integer value. After simulating each particle and computing its crater volume with Eqn. (6.14), the erosion on each surface grid face, $\dot{Z}_f(r_p)$, can be computed by summing the crater volume of the subset of particles which impacted in that surface grid face, and then dividing by the corresponding face area, A_f, and seed time:

$$\dot{Z}_f(r_p) = \frac{X(r_p)}{A_f t_{seed}} \sum_{n=1}^{N_{MC}} \forall_{c_n}. \tag{6.19}$$

Like in the TCV method, the total recession rate is computed by integrating Eqn. (6.19) using trapezoidal integration with the mass fraction, $X(r_p)$, acting as a weighting function. This procedure, while conceptually simple and straightforward to implement, was found to be computationally expensive as a large number of particle samples were required to converge to a smooth solution.

6.1.5. Uncertainty Quantification. Uncertainty and global nonlinear sensitivity analyses of the effect of Mars dust on TPS erosion in this study were performed using point collocation non-intrusive polynomial chaos (NIPC). NIPC has been shown to accurately propagate mixed (aleatory and epistemic) uncertainty through many types of computational models, including hypersonic flows [82, 83, 84], high-fidelity ray traced radiation [84], and robust aerodynamic optimization [85]. With the PCE approach, a response variable, α^* (quantity of interest such as erosion at a location), can be represented as a product of deterministic, α, and stochastic, Ψ, components for each mode, i, considered. The PCE is an infinite series, but a truncated solution is solved in practice:

$$\alpha^* \left(\vec{x}, \vec{\xi}\right) \approx \sum_{i=0}^{P} \alpha_i(\vec{x}) \Psi_i(\vec{\xi}), \tag{6.20}$$

where $\vec{x}$ is a vector of deterministic variables (including location and solution parameters) while $\vec{\xi}$ is a vector of stochastic variables. With the point collocation NIPC approach, a linear system is formed where the stochastic basis functions, Ψ_i, evaluated at various stochastic variable vectors, $\vec{\xi}$, is multiplied by a vector of unknown coefficients, α_i, and set equal to the response variables evaluated at each stochastic variable vector. For a PCE of order p with n uncertain variables, $(P + 1)$ modes are present in the system. At a minimum, the number of samples, N_s, required for NIPC is equal to the number of modes. For a well behaved PCE response surface, N_s is increased by multiplying by an oversampling ratio, OSR, greater than 1:

$$N_s = OSR(P + 1) = OSR\frac{(n + p)!}{n!p!}. \tag{6.21}$$

Epistemic uncertainties are propagated through a PCE by defining the basis functions, Ψ, as Legendre polynomials. The output epistemic interval is calculated by finding the minimum and maximum of the stochastic response surface by Monte Carlo sampling. For this study, all uncertain variables were considered to be epistemic.

Nonlinear global sensitivity analysis was performed with PCE by integration of the stochastic response surface using analysis of variance (ANOVA) decomposition to partition the observed output variation by variable, and then dividing by the total variation to find their total Sobol indices, which are a measure of how much of the total variation is due to that variable [86]. The i^{th} total Sobol index is defined as the ratio of the sum of all partial variances containing variable i and the total variance of the system [86]:

$$S_{T_i} = \sum_{L_i} \frac{D_{i_1,\ldots,i_s}}{D}; \; L_i = \{(i_1, \ldots, i_s) : \exists\, k, 1 \leq k \leq s, i_k = i\}\,. \tag{6.22}$$

These Sobol indices can then be ranked to determine which variables the solution is most sensitive to. Both the uncertainty quantification and sensitivity analysis can be performed either on integrated output variables, or on pointwise variables such as the surface erosion, which can give uncertainty and sensitivity distribution of the pointwise variable in a region of interest (e.g., TPS surface) [87].

6.1.6. Monte Carlo Results and Sample Size Convergence Study.

A convergence study was performed to determine the minimum number of particles necessary to provide an acceptable surface erosion prediction with the Monte Carlo method described in Section 6.1.3. To increase the convergence rate of the MC solution, a low-discrepancy sequence known as the Halton sequence [88] was used as opposed to a pseudo-random number generator. This drastically reduced the sample counts necessary for convergence to a smooth solution as compared with pseudo-random sampling. To further reduce sample counts required, the coarsest grid level's surface representation was used for the Monte Carlo solution, as this averages impacts over larger areas and reduces solution noise for a

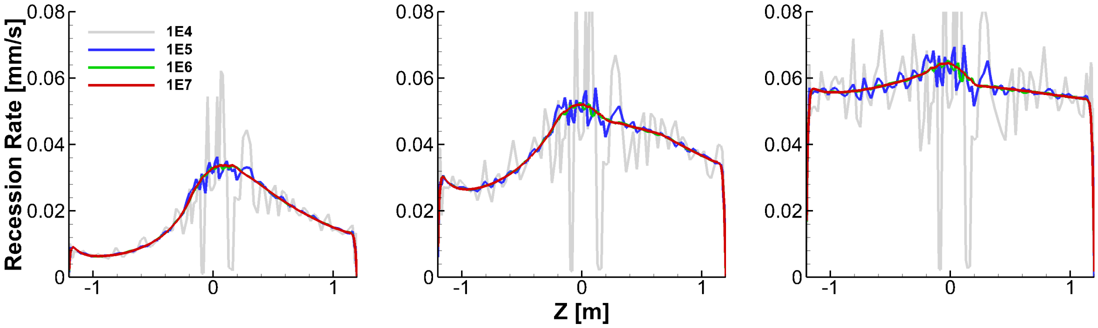

(a) $1\mu m$ (b) $2\mu m$ (c) $5\mu m$

Figure 6.3. Convergence of Monte Carlo erosion solution along the vehicle midplane for representative particle radii and sample sizes at the conditions for trajectory point 4 given in Table 6.1.

given sample set at the cost of lower resolution. These techniques provide the smoothest erosion distribution without using more complicated techniques like importance sampling or de-noising using filters or smoothing kernels. The convergence was studied for 35 km trajectory point with three representative particle radii, 1.0, 2.0, and 5.0 μm, which were chosen as they cover the range in which most of the particle phase mass is concentrated with reasonable modal radii, r_m. In Figure 6.3 the solution along the vehicle's midplane are shown for the particle radii mentioned previously, with increasing total particle counts: 10^4, 10^5, 10^6, 10^7. Note that Figure 6.3 demonstrates the recession rate assuming monodisperse particle phases, using different particle radii for each figure. These results are not integrated over particle radii using Eqn. (6.15), but are presented to demonstrate the convergence behavior for different particle sizes. From the results, it is clear that away from the vehicle's nose, a minimum of 10^6 particles begin to provide a smooth distribution, but due to the refined cells in the nose region a minimum of 10^7 particles becomes necessary.

6.1.7. Verification of the TCV Method. To verify the implementation of the TCV approach described in Section 3, the results of this method were compared to those obtained with the Monte Carlo approach. A convergence study was performed to determine the required number of particles required to obtain a converged solution. For both methods,

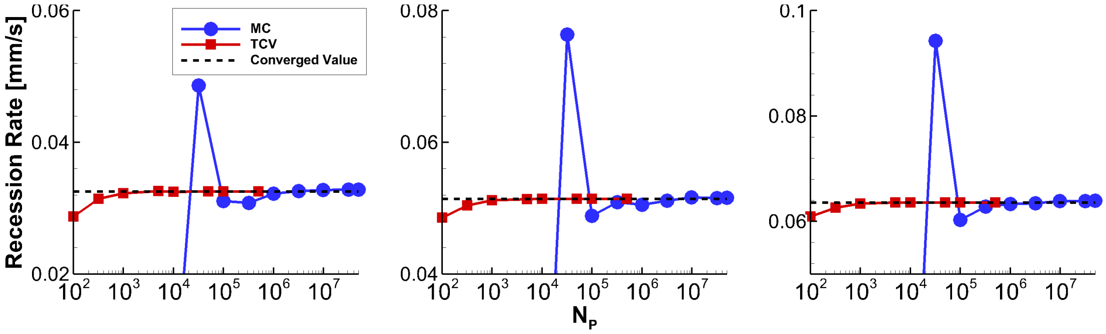

(a) 1μm (b) 2μm (c) 5μm

Figure 6.4. Convergence of MC and TCV recession rate solutions at the vehicle nose for representative particle radii as a function of sample size at the conditions for trajectory point 4 given in Table 6.1.

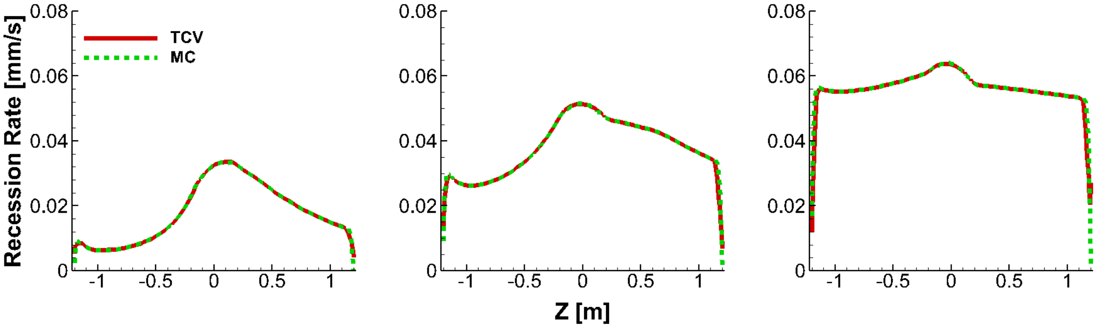

(a) 1μm (b) 2μm (c) 5μm

Figure 6.5. Comparison of converged MC and TCV method surface erosion rates along the vehicle mid plane at trajectory point 4 from Table 6.1. Solutions obtained using 5x10^3 particles for the TCV method and 10^7 for MC.

particles are initialized upstream of the CFD domain with uniform spatial density over the same area for consistency. The TCV particles were initialized on a regular grid. Figure 6.4 shows the convergence of the stagnation point recession rate solution at the 35 km trajectory point (where the highest recession rate was observed) obtained with both the TCV method and Monte Carlo approach. The TCV method was found to reach an acceptable level of convergence at approximately 10^3 particles, while the MC solution exhibited comparable convergence at approximately $10^{6.5}$ particles. At these sample sizes, both methods converge 2 significant figures of the erosion solution.

Using the nose recession rate as a measure of the convergence yields an acceptable estimate of the optimal particle count for each method, but a slightly larger count was used to ensure the solution reached the same level of convergence over the entire TPS surface for both methods. For Monte Carlo a sample size of 10^7 was used as this provides a smoother distribution of erosion over the TPS including the nose region where the recession rate is highest. For the TCV approach, due to the higher curvature of the TPS at the shoulder and uniform upstream spatial density of particles, a sample size of 5000 particles was found to give a uniformly acceptable solution. A comparison of the recession rate solution by each method for the 35 km trajectory point using these sample sizes is given in Figure 6.5. These results demonstrate that for a practical scenario, the TCV method is able to obtain a solution of comparable accuracy to MC using over 3 orders of magnitude fewer particle samples.

6.1.8. Full Trajectory Surface Erosion. The most important quantity to report for dust-induced surface erosion is the cumulative recession experienced by the vehicle TPS over a trajectory. Palmer et al. [10] performed this analysis for the nose of the vehicle and displayed the recession over time. For the current study, the recession history was computed over the full vehicle surface and sampled at the vehicle nose to compare with the reference solution as shown in Figure 6.6. Despite using different gas and particles phase solvers, as well erosion solution approaches, the recession at the vehicle nose predicted in the current work agrees quite well with the results of Palmer et al. [10], with only a 5% difference by the end of the trajectory.

Figure 6.12 demonstrates that the recession over the surface of the TPS is nonuniform due to the angle of attack sustained through the trajectory. The resulting shape of the recession distribution is similar to that of the recession rate at the peak erosion trajectory point. Based on the inclination of the vehicle surface to the flow using the convention shown in Figure 6.1, where the lower part of the forebody (Z<0) is more normal to the freestream velocity vector, intuition might lead to the conclusion that this region should experience the highest surface recession with a distribution similar to that seen in Figure 6.5c. In reality

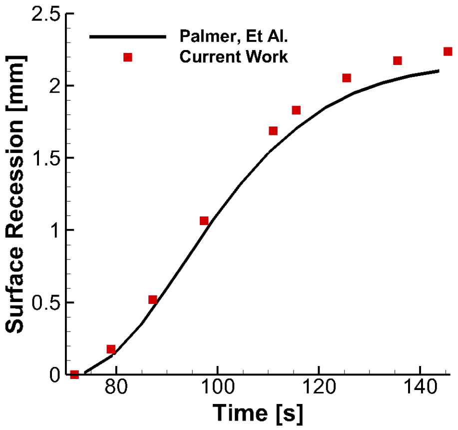

Figure 6.6. Surface recession [mm] over time at the vehicle nose due to particle impacts.

however this region exhibited a lower recession than the upper part of the forebody (Z>0) generally, with a distribution much closer to that seen in Figure 6.5b. The reasoning for this reduction in recession compared with the intuitively expected result is that the shock-layer is thickest in the lower region (Z<0), which increases the residence time of the particles in the shock layer under aerodynamic drag and heating leading to a decrease in the impact velocity and the mass. This can be explained by observing the velocity and degree of evaporation at impact for various particle radii, as seen in Figure 6.8. In the region where the shock layer is thinnest (approximately the stagnation point), the particles lose the least velocity and experience the least evaporation, leading to increased impact cratering and subsequently dust erosion. Figure 6.8b also demonstrates that evaporation only becomes significant for particles of radii 1 μm and smaller, and therefore has little impact to the overall erosion solution at their contribution is small due to the mass fraction distribution as shown in Figure 6.2.

6.1.9. Uncertainty and Sensitivity Analyses.

Following the verification and demonstration of the TCV method on the ExoMars problem reported in the literature, it was also utilized in an uncertainty quantification and sensitivity analysis study for the same case. For the UQ study, the 35 km trajectory point of Table 6.1 was used as this point is near the peak of the erosion rate experienced by the vehicle. The output quantity of interest for

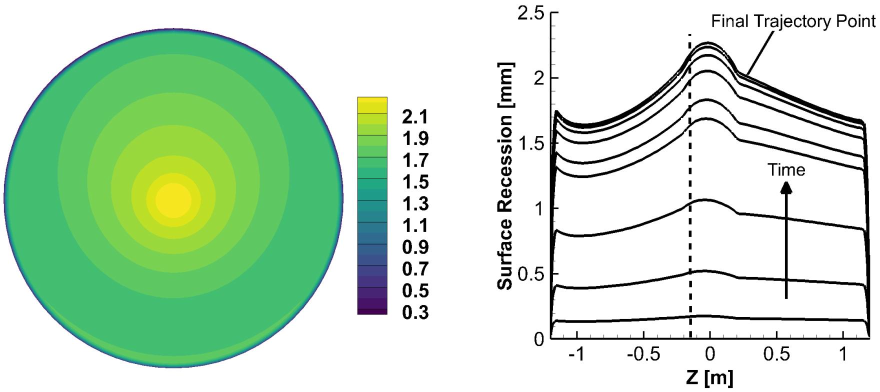

(a) Full TPS surface (b) Symmetry plane

Figure 6.7. Cumulative surface recession [mm] by particle impact over the trajectory shown over the full tps (a) and along the symmetry plane for each trajectory point (b). The approximate location of the stagnation point is denoted by a dashed line in (b).

uncertainty quantification is the surface recession rate due to dust erosion. In this work, only the parametric uncertainty in the particle simulation physical models and freestream particle characterization was studied, whereas the uncertainty in the Norcoat cratering model, Eq. (6.14), was not considered. Although error bars are included in the data used to produce the correlation [81], these errors may include similar uncertainty sources to those considered in this study, such as the impact velocity and size of particles. As the reported error does not isolate these uncertainty sources, simply including the coefficient uncertainty in addition to those we consider in this study could result in double counting of some uncertainty sources. The physical modeling parameters considered as uncertainty sources in this study are given in Table 6.2 along with their associated nominal values and uncertainty intervals.

For this study, all eight uncertainty sources are considered epistemic. Various sources in the literature were investigated to determine the uncertainty ranges for each variable, while the density, specific heat capacity, and latent heat of fusion of the dust material were given representative uncertainty bounds due to lack of specific information about the material composition of the dust particles. These representative bounds were

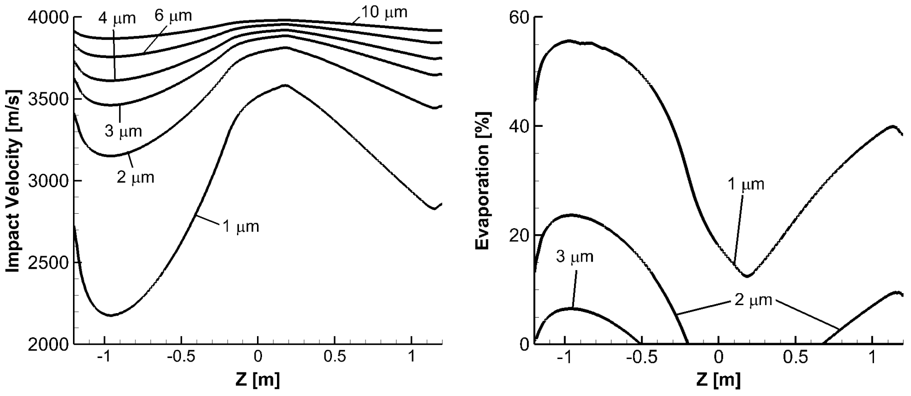

(a) Impact velocity (b) Evaporation

Figure 6.8. Surface impact velocity (a) and degree of evaporation (b) for various particle radii along the vehicle symmetry plane.

chosen as much of the variation seen in the values used for these variables in literature is due to lack of characterization of the true material composition rather than the inherent variability for a specific material. As seen in [60], various materials are proposed to fit the elemental composition observed in spectrograph data, which results in a large variation in the values of density, specific heat capacity and latent heat of fusion. Since using such large bounds would make these variables dominate the sensitivity results unrealistically, a smaller range was used to represent a more realistic level uncertainty were the composition more accurately characterized. For the drag coefficient and Nusselt number, the uncertainty

Table 6.2. List of uncertain parameters for the UQ study at trajectory point 4.

Variable	Description	Nominal	Uncertainty
ρ_m	Dust Material Density [kg/m^3]	2940	±5%
c_{P_p}	Dust Material Specific Heat Capacity [J/kg K]	703. [89]	±5%
δ_{C_D}	Drag coefficient multiplier	1	±15%
δ_{Nu}	Nusselt number multiplier	1	±15%
ζ	Dust Material Latent Heat of Fusion [J/kg K]	8.6x10^6	±5%
$\delta_{T_{vapor}}$	Vaporization temperature multiplier	1	±3%
q	Mass Mixing Ratio	6.26x10^{-5}	±0.75%
r_m	Modal Radius of Dust Size Distribution [μm]	0.4	±0.1 μm

range was based on the error of Henderson's curve fit compared to experimental data [31]. Using Reynold's analogy, it is assumed that the Nusselt number correlation has an equivalent amount of error to drag coefficient. The error in the vaporization temperature model is based on the error observed in Palmer, et al where the correlation is compared with results from the chemical solver code Mutation++ [10]. The uncertainty range for the Mass Mixing Ratio was determined by analyzing the Mars Reconnaissance Orbiter (MRO) data for the month of July 2007 [76]. Measurement error associated with the 35km altitude was collected for each data record and a histogram of the instances was created. The histogram representation of this data indicated that the bulk of the error values were centered around 0.75‰. Lastly, the modal radius of the particle size distribution was given a range of 0.3 to 0.5 μm based on interpretation of the curve fits proposed by Toon et al. [60] and their agreement with measurements taken by the infrared interferometric spectrometer (IRIS) of Mariner 9.

Using the point collocation NIPC approach described in Section 6.1.5, the eight input uncertainties described in Table 6.2 were propagated through the model using a 3^{rd} order PCE response surface with an oversampling ratio of 2, requiring a total of 330 particle phase and TCV surface erosion solutions. Using an OSR greater than 1 prevents over-fitting of the response surface by solving the PCE system with least squares; Hosder et al. [41] showed that for practical problems an OSR of 2 provides good solution quality without an excessively large number of samples required. A 2^{nd} order PCE response surface was also produced with an OSR of 2 which verified that the 3^{rd} order PCE response surface was sufficient.

The nominal solution along the symmetry plane of the vehicle, as well as the epistemic uncertainty bounds are displayed in Figure 6.9. As is seen in Figure 6.9, the epistemic bounds follow the same solution trends observed in Section 6.1.8. Strong parallels with the erosion distribution observed for $2\mu m$ particles in Figure 6.5b are present as the peak of the mass fraction function for particles occurs near this radius.

To determine the major physical modeling parameters contributing to the surface erosion uncertainty, the Sobol indices for each variable were computed. The Sobol indices were then weighted by the epistemic bound of the solution at that point, and normalized by the largest value over the TPS surface. The distribution of normalized weighted Sobol index (NWSI) for each variable along the symmetry plane of the TPS is given in Figure 6.10. The dominant variables are the density of the particle material and modal radius of the size distribution. It is perhaps an unsurprising result that particle density is a large contributor given that the mass of the particle at impact is a direct contributor to the impact cratering model given in Section 6.1.3. The modal radius of the particle size distribution however has a large influence as it shifts the peak of the mass fraction function. The distribution of the uncertainty contributions from these variables differ significantly though, with the effect of particle density correlating strongly with the shock-layer thickness. The effect of modal radius is much more uniform across the TPS however, as it affects the shape of the size distribution uniformly in space. Figure 6.11 shows further how the effect of particle density and modal radius vary over the entirety of the TPS.

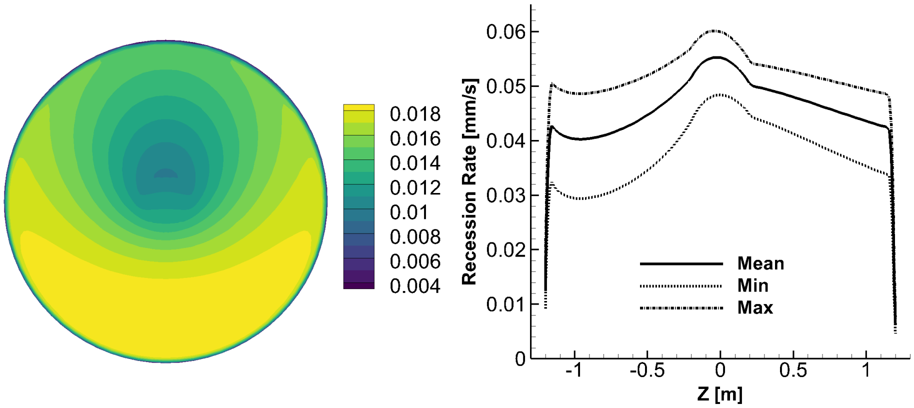

(a) Full TPS surface (b) Symmetry plane

Figure 6.9. Range of output uncertainty in the recession rate [mm/s] at trajectory point 4 over the TPS surface (a) and along the symmetry plane of vehicle (b).

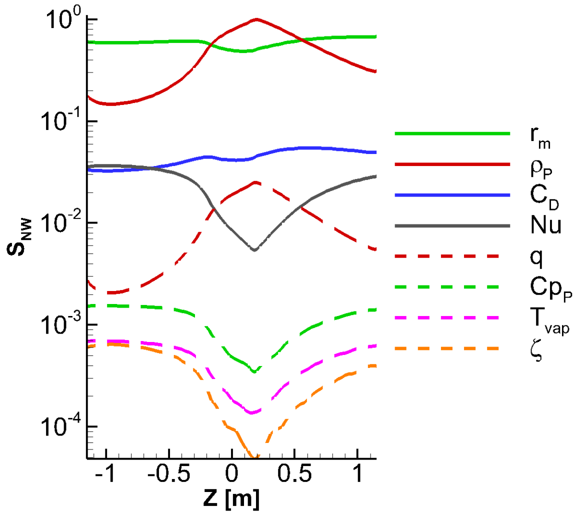

Figure 6.10. Normalized weighted Sobol indices for each uncertain variable along the symmetry plane of the vehicle.

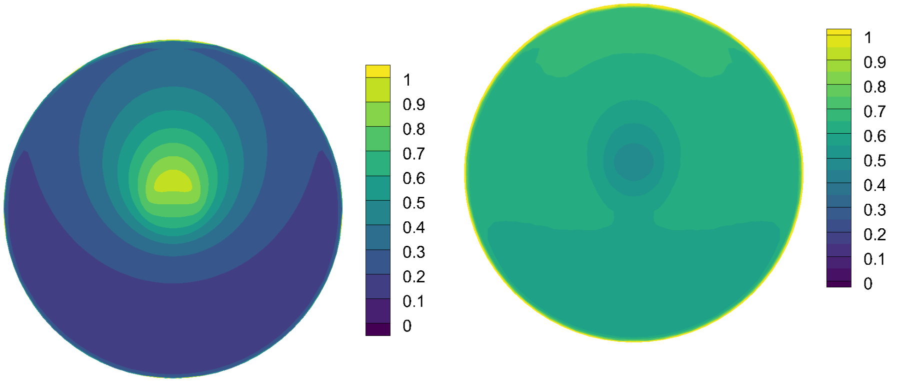

(a) Particle material density, ρ_m

(b) Particle size distribution modal radius, r_m

Figure 6.11. Distribution of normalized weighted Sobol indices over the vehicle surface for the two highest contributing uncertain variables.

Lastly, the normalized weighted Sobol indices are integrated over the surface and averaged with the total surface area to quantify the effect of each variable over the entire TPS surface with a single metric. These metrics, the normalized integrated weighted Sobol indices (NIWSI), are given in Table 6.3, showing that despite particle density having the largest local value of weighted Sobol index, the more uniform distribution for modal radius leads to a larger global effect. Overall, the sensitivity results show the importance

Table 6.3. Normalized integrated weighted Sobol index results.

Variable	NIWSI
r_m	0.6145
ρ_m	0.2918
δ_{CD}	0.0494
δ_{Nu}	0.0303
q	0.0069
C_{P_p}	0.0029
ζ	0.0024
$\delta_{T_{vap}}$	0.0018

of accurate characterization of dust particles (material composition and size) for reducing uncertainty on the surface erosion. As discussed before, the evaporation mechanism has a low impact on the overall erosion solution as only small particles are affected significantly. Because of the low contribution of small particles to overall erosion, the effect of varying the vaporization temperature and latent heat of vaporization is suppressed, as demonstrated in their NWSI distributions in Figure 6.10.

6.2. COUPLING EFFECTS IN AEROTHERMODYNAMIC ENVIRONMENTS

In this section, coupled analysis of particle-laden hypersonic flows is presented. The extended TCV method, described in Section 3.4, was used to efficiently perform two-way coupled solutions using a sparse set of particle samples as opposed to costly Monte Carlo techniques typically used. The section begins background information related to surface heating mechanisms in a two-way coupled context and a predictive factor for the degree of coupling in particle-laden hypersonic blunt body problems. Next, a series of verification cases are presented to benchmark the accuracy of the TCV technique. Later, the technique is applied to an experimental case involving a shock tube with dust introduced to the test section to study heating augmentation. Comparison is made with the MC technique to demonstrate the cost savings and smooth solutions of the TCV approach, similar to the results shown in

Section 6.1. Lastly, the developed methodology is applied to a representative Mars entry scenario to investigate the possibility for coupling effects to result in heating augmentation for a planetary entry.

6.2.1. Surface Heating Mechanisms. There are two main mechanisms for surface heating in two-way coupled dilute gas-particle problems: convective heating which may be modified due to changes in the boundary layer based on the coupled particle phase solution, and collisional heating due to particle impacts on the surface. In this work, heating augmentation refers to the effect of flowfield coupling on the surface heating, while collisional heating will refer solely to that of particle surface impacts. Particles which impact a solid wall will impart a portion of their kinetic energy as thermal energy through dissipative processes. The amount of energy exchanged during an impact is dependent on the materials of the particle and wall, as well as the impact velocity. Ching et al. [40] express the post-collision velocity-vector as function of the incident velocity vector, surface unit normal vector, and coefficients of restitution for the normal and transfer velocity components:

$$\vec{u}_{p+} = -a_n \left(\vec{u}_{p-} \cdot \hat{n}_w\right) \hat{n}_w + a_t \left[\vec{u}_{p-} - \left(\vec{u}_{d-} \cdot \hat{n}_w\right) \hat{n}_w\right], \tag{6.23}$$

where the subscripts '+' and '-' refer to the post and pre-collision states, respectively. The terms a_n and a_t refer to the coefficients of restitution in the normal and tangential directions with respect to the wall unit normal vector. The kinetic energy deficit for particle 'n' is then assumed to transfer to the wall it collided with in the form of thermal energy at the impact location:

$$\Delta KE_n = \frac{m_{p,n}}{2} \left(\left\|\vec{u}_{p,n,+}\right\|^2 - \left\|\vec{u}_{p,n,-}\right\|^2 \right). \tag{6.24}$$

With the TCV method, similar to the surface erosion solution process described in Sec. 6.1.3, the total collisional heat flux over the region bounded by the 'i^{th} TCV's impact face is the product of the average collisional heat transfer of each of the TCV particles and the particle flux:

$$\dot{Q}_{col,i} = \frac{N_{T,i}}{N_{p,i}A_{I,i}} \sum_{n=1}^{N_{p,i}} \Delta KE_n. \tag{6.25}$$

The cumulative effect of particle impacts results in an additional surface heat flux mechanism. As the current study was primarily concerned with Mars entry scenarios involving vehicles with ablative thermal protection systems (TPS), all particle impacts were assumed to be perfectly inelastic. Inelastic collisions represent embedding of the particles within the TPS surface and the most conservative scenario for collisional heating.

6.2.2. Coupling Potential Factor for Blunt Body Flows. As coupled analyses increase the cost of a solution, a cheap predictor of when coupling may result in a noticeable change in the heat flux for a problem was desireable. A simple factor was developed for predicting when coupling was important for blunt body flows. This factor is the ratio of the shock standoff distance to the particle momentum relaxation distance:

$$f_c = \frac{\Delta_s}{\tau_m}. \tag{6.26}$$

The particle momentum relaxation distance, given in Eqn. (2.38) can be evaluated with the actual drag model being used in the problem, but it is much easier to evaluate with the Stokes' drag coefficient, 24/Re$_p$. This approximation is small and doesn't change the resulting coupling potential factor strongly. Applying Stokes' drag from Eqn. (2.39) results in the following expression for the coupling potential factor:

$$f_c = \frac{9\Delta_s \mu_\infty}{2\rho_p r_p^2}, \tag{6.27}$$

where μ_∞ is the freestream gas viscosity. The shock standoff distance can be estimated with curve fits, such as that for spherical bodies in air by Billig [90]. As an initial pure gas solution was necessary for the coupled solutions in this work, the shock standoff distance was simply measured distance at the vehicle nose or stagnation point of the gas solution.

Table 6.4. Conditions at station 1 for the Rayleigh flow test case, including heat added from stations 1 to 2.

M_1	T_1 (K)	P_1 (Pa)	γ	$q_{1\rightarrow 2}$ (J/kg)
2	298	15000	1.4	10^5

The physical interpretation of the coupling potential factor is that for values approaching or exceeding unity, the particle velocity will equilibrate with the surrounding gas, and fully exchange momentum to the gas phase. Values approaching zero indicate that particles will retain their momentum for much longer and exchange little of it to the gas phase. As will be demonstrated in Sections. 6.2.5 and 6.2.6, this coupling potential factor was able to effectively predict the degree to which the coupled solution in blunt body problems would differ from the pure gas solution with increasing particle mass loading.

6.2.3. Verification of the Extended TCV Method. In the current work, coupled solutions were performed using LAURA as the gas solver and the extended TCV method. First, two analytical one-dimensional verification cases were chosen to ensure that the source term injection and normalization processes were implemented correctly. The first case is a constant area flow with heat addition, which is compared against the Rayleigh flow solution [91]. The second case is a pipe flow with constant friction coefficient, which is compared against the Fanno flow solution [91].

In Rayleigh flow, the fluid is assumed to be frictionless and non-adiabatic [91]. The flow properties are modified solely by the addition of heat, which drives the Mach number towards 1.0 regardless of whether the initial flow is subsonic or supersonic. For a given heat per unit mass added between stations 1 (the inlet) and 2 (the outlet), referred to here as $q_{1\rightarrow 2}$, the total temperature, T_t, at station 2 is:

$$T_{t,2} = T_{t,1}\left(1 + \frac{q_{1\rightarrow 2}}{C_p T_{t,1}}\right). \tag{6.28}$$

Table 6.5. Conditions at station 1 for the Fanno flow test case.

M_1	T_1 (K)	P_1 (Pa)	γ	A (m^2)	C_f
4	200	5000	1.4	0.1	0.02

The Mach number at station 2 is then found by the following:

$$\frac{T_{t,2}}{T_{t,1}} = \left(\frac{1+\gamma M_1^2}{1+\gamma M_2^2}\right)^2 \left(\frac{M_2}{M_1}\right)^2 \left(\frac{1+\frac{\gamma-1}{2}M_2^2}{1+\frac{\gamma-1}{2}M_1^2}\right). \tag{6.29}$$

Solving this numerically for the Mach number at station 2, this can be used to find the static temperature:

$$T_2 = T_1 \left(\frac{1+\gamma M_1^2}{1+\gamma M_2^2}\right)^2 \left(\frac{M_2}{M_1}\right)^2 \tag{6.30}$$

The conditions at station 1 in this test case are given in Table 6.4. Figure 6.12a shows that the static temperature distribution predicted by LAURA exhibits excellent agreement with the analytical solution given by equations 6.28 to 6.30.

In contrast to Rayleigh flow, Fanno flow is an adiabatic one-dimensional problem in which momentum is lost from the flow due to friction at the wall [91]. A constant friction coefficient is specified through the flow which drives it towards a choked condition, much like in the Rayleigh case. In Fanno flow, the properties are a function of distance to the position at which choking occurs. The Fanno function is defined as:

$$f_v = \frac{\gamma+1}{2}\ln\left(\frac{1+\frac{\gamma-1}{2}M^2}{M^2}\right) - \frac{1}{M^2} \tag{6.31}$$

The Fanno function at station 2 is the sum of the function evaluated at the Mach number at station 1 and the total friction force added between the stations:

$$f_{v,2} = f_{v,1} + \gamma C_f \frac{cL}{A}, \tag{6.32}$$

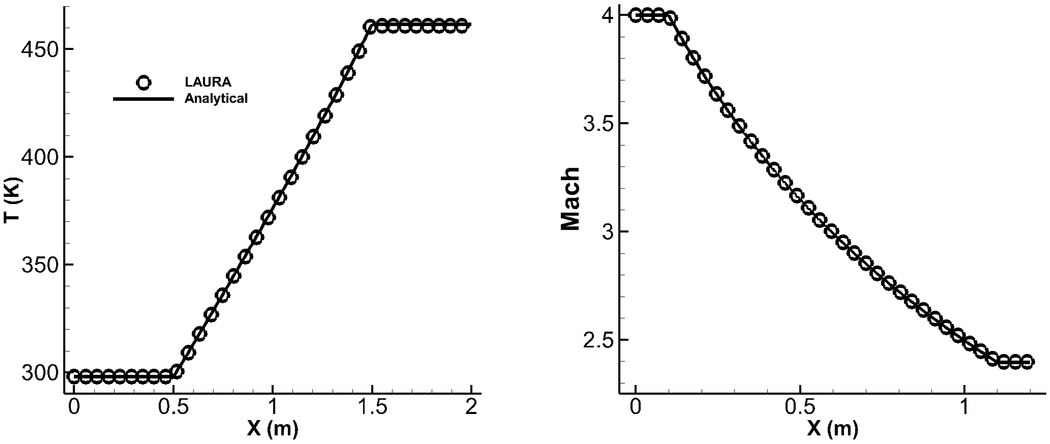

(a) Rayleigh Flow (b) Fanno Flow

Figure 6.12. Quasi-1D flow cases solved with LAURA compared against analytical results.

where c, L, and A are the perimeter, length, and cross sectional area of the pipe, respectively. Equation 6.31 is then solved for the Mach number at station 2 using the value of $f_{v,2}$.

The momentum source term for LAURA is the shear force on each cell, which is:

$$S = \frac{c\Delta x}{2} C_f \rho u^2, \tag{6.33}$$

where Δx is the length of the cell in the flow direction. As the friction coefficient in the Fanno problem is normalized by the local flow properties, the momentum source term is updated occasionally with the latest flow solution, arriving at a final source field after a few cycles. Using the conditions in Table 6.5, the Mach number distribution along the pipe was predicted with LAURA, and again was found to agree well with the analytical solution. Together, these cases verify that the basic coupling process with LAURA was performed correctly.

Table 6.6. Conditions for the dusty supersonic flat plate case.

M_∞	$Re_{\lambda_p,\infty}$	q	Pr	D_p (μm)	ρ_p (kg/m^3)	Tw
1.5	10^4	1	1	1	2700	0.5 T_∞

6.2.4. Heating Augmentation on a Flat Plate in Dusty Supersonic Flow. To verify the two-way coupled solution scheme involving LAURA and the extended TCV method, the dusty laminar supersonic flow over a flat plate case considered by Wang and Glass [18] was studied. This case is a common benchmark [20, 40] as it provides a simple scenario in which 'analytical' solutions in the form of asymptotic boundary-layer profiles can be compared with, allowing for verification of the entire two-way coupled gas-particle solver suite. The case was solved in nondimensional form according to Ref. [18], with the length scale based on the momentum relaxation distance of the particle phase. For this case, the particle Nusselt number was held constant at 2, and the drag coefficient was specified by Stokes' drag formula:

$$C_{D,\text{Stokes}} = \frac{24}{Re_p}. \tag{6.34}$$

The resulting momentum relaxation time, τ_m, is given in Eqn. (2.39). Multiplying this time by the freestream velocity results in the momentum relaxation length scale,

$$\lambda_p = \tau_m U_\infty = \frac{2\rho_p r_p^2 U_\infty}{9\mu_g}. \tag{6.35}$$

The case conditions are given in Table 6.6, including the Reynolds number of the dusty gas flow, $\text{Re}_{\lambda_p,\infty}$. This is not to be confused with the particle Reynolds number relative to the surrounding gas given in Eqn. (2.21). Rather, this Reynolds number is evaluated based on the freestream gas conditions and the particle momentum relaxation length scale:

$$Re_{\lambda_p,\infty} = \frac{\rho_g U_\infty \lambda_p}{\mu_g}. \tag{6.36}$$

Wang and Glass [18] solved the problem of dusty flow over a semi-infinite flat plate by separating the plate into 3 regions: the large slip region near the leading edge, the small slip region far downstream, and the moderate slip region between the leading edge and downstream regions [18]. They present asymptotic solutions for the large and small slip

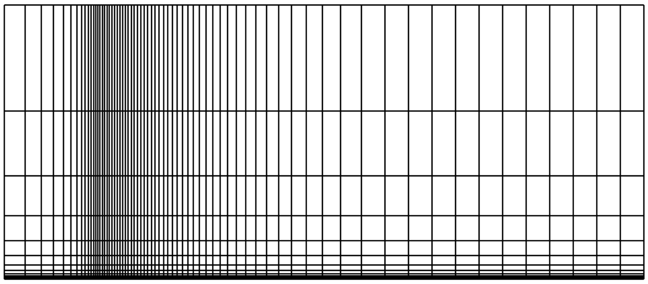

Figure 6.13. Computational grid used in the flat plate case. Every 4^{th} point is shown.

regions, and a finite difference solution is made that spans the regions. In the present work, the fluid domain was sized to capture primarily the large slip region, as this is the region of flow in which the largest velocity nonequilibrium between the phases is present. The large slip region spans approximately from 0 to 20% of the momentum relaxation scale, λ_p.

The grid used in this study was adapted from the NASA Langley Research Center Turbulence Modeling Resource [92] by scaling to an appropriate length scale in the various directions and extrusion in the flow transverse direction to make a 3D grid with a single cell thickness necessary for LAURA. The grid, which is shown in Figure 6.13, was split in the flow direction at the plate leading edge, and an inviscid wall boundary was applied at the wall face ahead of the leading edge. An isothermal no-slip wall boundary condition was specified on the wall face for the remainder of the cells in the flow direction. The total grid dimensions were 272x96 cells (flow direction and wall-normal direction, respectively), and a version of the grid coarsened by a factor of 2 in each direction was used to assess the grid independence of the solution. The grid convergence index (GCI) of the fine grid was computed assuming an order of accuracy of 1 and factor of safety of 3, as suggested by Roache [93] to be conservative. With the exception of the leading edge singulary, in which the GCI spikes slightly, the fine grid GCI of the heat flux was found to be less than 1.5% at each point along the plate.

For the particle phase solution, particles were seeded at the inflow domain with clustering such that the spacing and growth rate of the interparticle distances was similar to the gas-phase grid. A total of 100 TCV probe particles were used, arranged in a contiguous configuration. Increasing the particle count beyond 100 had no meaningful impact on the solution, and was comparable to the cell count in the wall-normal direction. Starting from a converged pure gas solution, a total of 5 loose-coupling cycles of 10000 iterations between calls to the particle phase solver were performed until the final converged two-way coupled solution was obtained.

Figure 6.14 presents the results of this case with the current approach at a position of $0.105\lambda_p$ units downstream of the plate leading edge. Figure 6.14a shows a comparison between the present solution and the large-slip asymptotic solution of Ref. [18]. The weak leading-edge shock altered the boundary layer edge values downstream slightly, which can be seen in the slightly reduced velocity at similarity parameter (η) values above four approximately. Despite this, the wall gradient and boundary layer thickness were accurately predicted. The same was true for the temperature profile, which is confirmed in Figure 6.14b due to the excellent agreement in convective heat flux to the wall for both dusty and pure-gas conditions. Overall, this case confirms that the extended TCV method and gas-particle solver suite were implemented correctly and can recover the correct solution under the physical modeling assumptions described previously.

Figure 6.15 demonstrates the final source field of the converged two-way coupled solution, with Figure 6.15a showing the distribution of x-momentum source near the plate, while Figure 6.15b shows the profile of x-momentum and energy source in the wall normal direction at the same location along the plate as Figure 6.14a. Here, it can be seen that the source field produced by the TCV method was smooth and free of numerical noise or artifacts, even in the lowest parts of the boundary layer, as can be seen in Figure 6.15b.

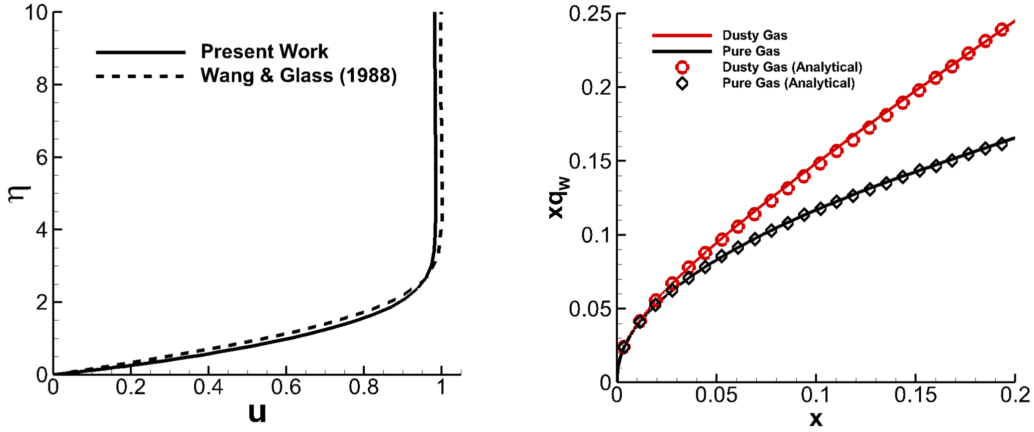

(a) Tangential velocity profile.

(b) Convective heating distribution.

Figure 6.14. Comparison of the present work with the results of Wang and Glass [18] at the x=0.105 station.

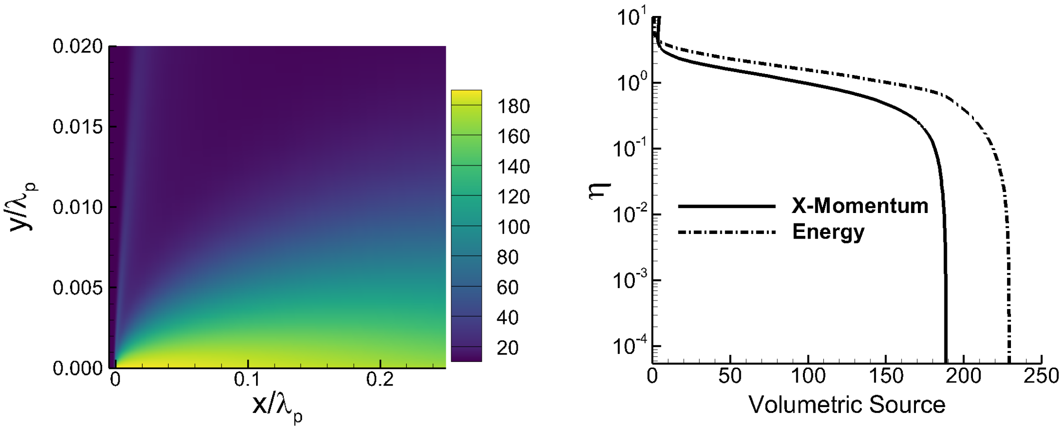

(a) X-momentum volumetric source field over the plate.

(b) Profile of x-momentum and energy volumetric source in wall-normal direction.

Figure 6.15. Converged x-momentum volumetric source field and profiles of x-momentum and energy volumetric sources at x=0.105.

6.2.5. Heating Augmentation to Blunt Bodies. With the general approach verified, the next case studied was the experimental campaign by Vasilevskii and Osiptsov [94]. In this scenario, a shock tube was loaded with particulate of various materials and sizes with spherical test articles of various radii. The aim of the study was to measure the change in heating to a blunt body in high-speed flows due to particulate presence and to compare with correlations and previous analytical works. For the present work, the 6 mm nose radius

Table 6.7. Test section conditions for the experimental case of Vasilevskii and Osiptsov [94].

M_∞	$P_{t,\infty}$ (bar)	$T_{t,\infty}$ (K)	R_n (mm)	T_{wall} (K)	D_p (μm)	ρ_p (kg/m^3)
6.1	17.5	570	6	300	0.19	2264

case with silica particles introduced to Mach 6.1 air flow was selected for comparison. Test section conditions for this case are given in Table 6.7. The mass loading ratio was varied from 1 to 8% to observe the trend in heating augmentation due to increasing dust content.

This problem was treated with an axisymmetric flow assumption, with the primary focus being the stagnation point region. This was due both to lack of off-stagnation heating data and the assumption of no reflected particles, which only affects the downstream region appreciably. In the experiment particles are presumed to have lost the majority of their kinetic energy through the shock layer and impacted the surface with a low speed. Upon impact, the particles are presumed to have been reflected and were advected downstream near the wall. Neglecting these reflected particles may result in a slight overprediction of the source terms in the near-wall region starting at approximately the 10 to 20 degree angular position on the sphere as reflected particles would be advected downstream, pulling momentum from the flow near the wall. At the stagnation point, this effect can be neglected.

As particles no longer contacted the surface of the sphere past approximately the 45° angular position on the sphere, neighboring TCV probe particles in this region have radidly changing trajectories, which resulted in exaggerated sub-TCV volumes and underpredicted source terms unless a larger probe count was taken to refine the solution. To simplify the analysis slightly, noncontiguous TCVs were used as described in Sec. 3.3. Pairs of very closely separated particles were seeded over the inflow, and TCVs were only formed from these pairs. The TCVs were not connected with each other as in previous analyses, but instead gave a highly refined solution along the path of their mean trajectories. Interpolation was performed between sub-TCV centroids to resample the TCV solution to the gas phase grid. A total of 300 TCV probe particles arranged in 150 noncontiguous TCVs were used to solve the source fields in each loose-coupling cycle. The particles forming each TCV were spaced 10^{-6} meters apart at the upstream seed location, as this resulted in particle trajectory pairs that remained nearby each other downstream of their seed location. Increasing the particle count beyond 300 resulted in no meaningful difference in the solution.

The gas phase grid consisted of 120 cells in the tangential direction and 96 cells in the wall normal direction, with clustering at both the shock and boundary layer. Using the same order of accuracy and safety factor as in the flat plate case, the GCI for the fine grid was computed with a grid coarsened by a factor of 2. The GCI for the heat flux was less than 1.5% over the entire sphere surface, and less than 0.5% at the stagnation point. Collisional heating was neglected due to the extremely low impact velocity of particles over the surface of the sphere. A total of 3 loose-coupling cycles of 15,000 iterations were performed.

Figure 6.16 shows the velocity and temperature of particles along the stagnation streamline. The particles lost the majority of their initial momentum before impacting the surface, and experienced a moderate increase in temperature. Figure 6.17 shows the temperature distribution of the stagnation streamline for both pure gas and dust loaded conditions, where it can be seen that the thickness of the shock layer, as well as peak temperature were modified slightly. A reduction in the shock layer thickness of approximately 2.9% is observed in Figure 6.17. Compared with the pure gas condition, the dusty gas temperature is higher toward the body, indicating that the coupling effect is cumulative and related to particle residence time and momentum loss.

Figure 6.18 shows the ratio of dust-augmented to pure-gas stagnation heat flux as a function of mass loading ratio, comparing the current work to measurements and a theoretical maximum curve from Ref. [94]. The results indicate that the current approach agrees quite well with experiment up to moderately high loading, such as the 3% condition given in Ref. [94], and that a significant coupling effect occurs due to the large percentage of momentum exchange from the particles. At extremely high loading, however, the current

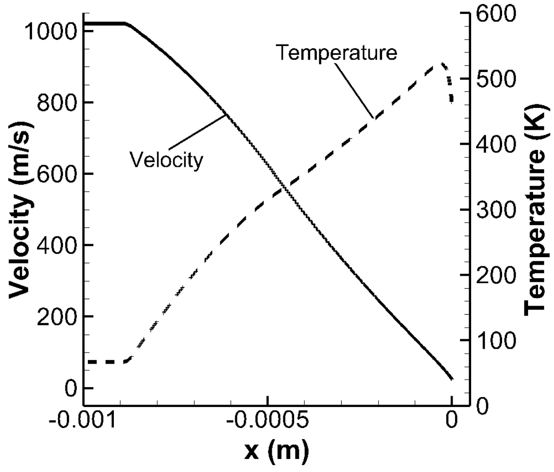

Figure 6.16. Particle velocity and temperature along the stagnation streamline.

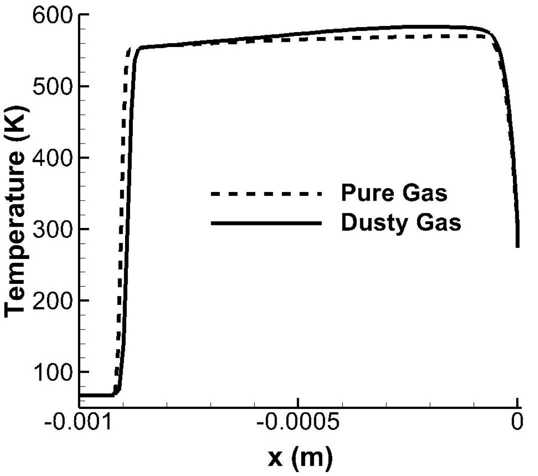

Figure 6.17. Stagnation streamline temperature profile for pure gas and 4% dust loading conditions.

approach underpredicts reported experimental values by approximately 15 to 30%, similar to the predictions by Osiptsov et al. [94]. As the particles reduced to a low velocity relative to the freestream condition near the surface of the sphere, the local number density increased proportionally to the ratio of freestream to local velocity of particles. This local increase in particle number density near the stagnation point of the sphere may push the case to a regime in which volume filtering of the gas phase governing equations becomes necessary. This may cause disagreement for methods which assume a dilute particle phase, such as the current work. Similar to discussion in Ref. [94], other factors may be the nonspherical nature of particles that has been neglected, and the technique by which particle size has been measured. Particles are assumed to have a single mean size, given in Table 6.7, so error in this mean size and neglecting polydispersity may have affected agreement. No error estimates are provided with the experimental results, which may be large at high loading as evident from the increased scatter in reported results. Ching et al. [40] demonstrated that the choice of drag model impacts the heating augmentation prediction significantly. As particles lose the bulk of their momentum in the shock layer, the overall coupling effect

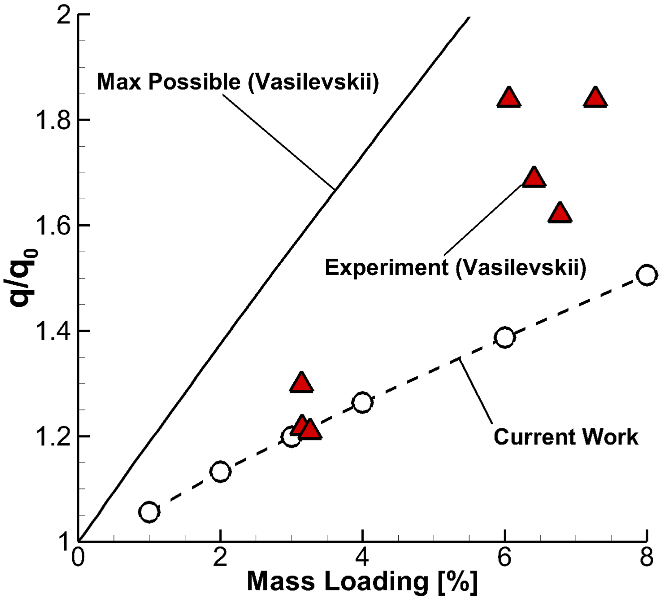

Figure 6.18. Stagnation point heating augmentation compared with max possible heating augmentation and experiment by Vasilevskii and Osiptsov [94].

between the phases is sensitive to the drag force on the particles. This case demonstrates the effectiveness of the coupling potential factor given by Eqn. (6.27), as a value of 0.87 was predicted from this case, indicating strong scaling of the coupling effect with increasing particle mass loading.

Overall, this case demonstrates the effectiveness of the current approach for particle counts as low as 300 as compared with Monte Carlo techniques. Though not demonstrated in this work, some limited investigation with a reference Monte Carlo approach showed that for this case several hundred thousand to millions of particles were needed to achieve source fields of equivalent quality to the TCV approach, which was consistent with particle counts reported by Ching et al. [95]. An example MC source field computed with 100,000 total particles was compared with the TCV approach in Figure 6.19, where it can be seen that considerable numerical noise was still present in the MC solution particularly in the boundary layer region. At particle counts of 1 million or higher, the noise in the MC solution began to be negligible.

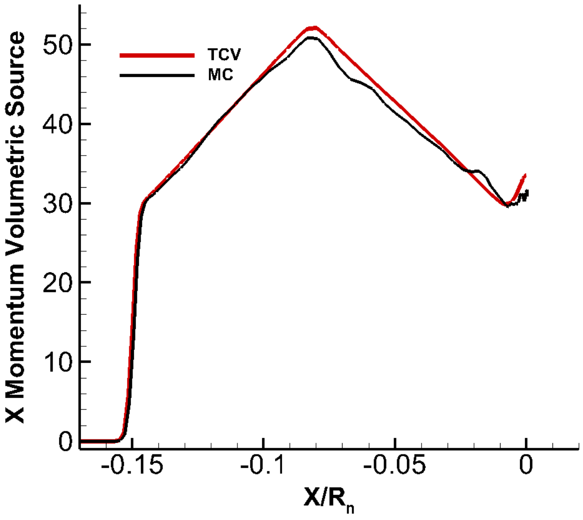

Figure 6.19. Comparison of the nondimensional volumetric source field between the TCV approach and a steady-state Monte Carlo solution.

6.2.6. Heating and Erosion Augmentation in a Mars Entry Scenario. With successful comparisons between the current work and various test cases, the TCV method and gas-particle solver suite were used to predict the heating and erosion augmentation for the ExoMars case studied in Sec. 6.1. The 45 km altitude trajectory point given in Table 6.1 was chosen as the freestream condition, but at zero angle of attack. This trajectory point was chosen as it is near the peak convective heating rate, but sufficiently low to have an appreciable amount of dust loading. The gas phase was again modeled using a two-temperature thermochemical nonequilibrium gas model consisting of the following 8 species: CO_2, N_2, CO, NO, O_2, C, N, O. The freestream was assumed to have gas mass fractions of 97% CO_2 and 3% N_2. The flow was assumed to be laminar, with a fully-catalytic no-slip wall for the vehicle surface. The surface temperature was modeled with a radiative adiabatic wall temperature. Similar to previous works on this case, the July 2007 global dust storm was used to determine a representative highly loaded dust condition, with a dust mass loading, q, of approximately 0.0136% [10] determined using data from the Mars

Reconnaissance Orbiter (MRO) [76]. Figure 6.1 shows a representative temperature field for this case and the vehicle geometry. Further details of the case and vehicle geometry are found in Refs. [10, 35, 75].

In the previous cases, particle vaporization was not likely due to relatively low flight speeds. In this case however, vaporization can occur for smaller particles due to the high relative Mach numbers for particles and gas phase temperature within the shock layer. While vaporization was treated for the particle tracing, the vaporization products were neglected in the gas phase in this study. A further simplification made was to use a single representative particle size based on the mass fraction distribution. Based on the modified gamma size distribution proposed by Toon et al. [60] with a modal radius of 0.35 microns, the peak of the mass fraction occured near a radius of 2.5 microns.

Similar to the Vasilevskii case, an axisymmetric assumption was used to simplify the solution process. The computational grid used for this case had 120 cells in the tangential direction and 64 in the wall-normal direction, with clustering at the shock and boundary layer regions. The grid used the same dimensions as the grid used in Ref. [35], which was shown to be sufficiently fine. Similar to the previous case, a total of 300 particles arranged in 150 noncontiguous TCVs were used to produce the source fields in each loose-coupling cycle. The upstream spacing between the particles in each TCV was 10^{-6} meters. A total of 3 loose-coupling cycles of 20,000 iterations were performed. Again, particles were assumed to collide inelastically with the surface, and worst case collisional heating was computed as described in Sec. 6.2.1. No interparticle collisions were treated, which were shown by Sahai et al. [13] to have a very small impact on the collisional heating to the surface at low mass loading values. At extreme levels of dust loading, collisions between particles can result in a blockage effect which reduces this heating mechanism.

Figure 6.20 shows the heat flux over the vehicle surface for dusty and pure-gas baseline conditions, with measured loading from MRO data in Figure 6.20a and exaggerated loading in Figure 6.20b. In both figures, the red line corresponds to the full two-way coupled

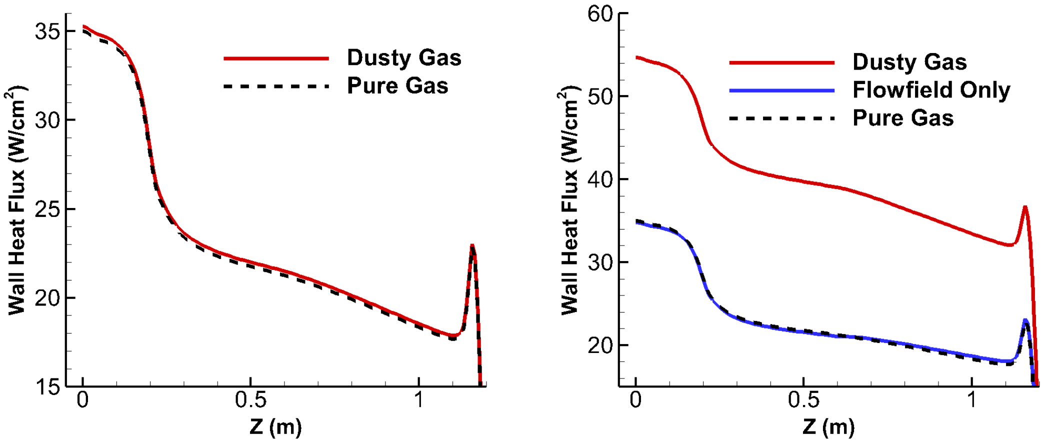

(a) $q = 0.014\%$ (b) $q = 1\%$

Figure 6.20. Heat flux over the vehicle surface for pure and dusty gas conditions.

solution including collisional heating, while the blue line excludes collisional heating. For realistic loading conditions the overall augmentation was small, with the stagnation point value being increased by 0.27 W/cm^2 (0.77%). The change in convective heating due to two-way coupling was much smaller than the effect of collisional heating, and therefore negligible. Increasing the mass loading to 1%, or approximately 71 times the baseline value, resulted in a much larger increase in heating. This increase was again largely due to collisional heating, with the stagnation point value being increased by 19.7 W/cm^2 (56.3%). The change in convective heating due to two-way coupling was noticeable but still negligible. It was important to note however that under the assumption of a monodisperse dust phase with 2.5 micron radii particles the convective heating at the stagnation point experienced a reduction of 0.2 W/cm^2 at a mass loading of 1%. The reasoning for this slight reduction in convective heating is the high relative Mach number of particles in the shock layer, which resulted in significant thermal eneregy exchange from the gas to the particles.

Figure 6.21 shows the volumetric source for x-momentum and energy along the stagnation streamline. Upon crossing the shockwave, strong drag and heating was imparted to the particles due to the supersonic relative velocity of the particles with respect to the

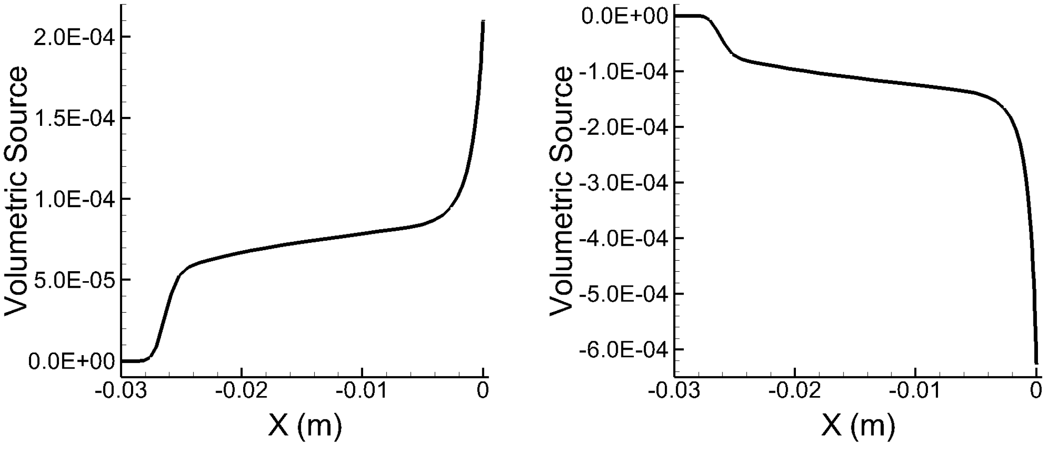

(a) X-momentum

(b) Energy

Figure 6.21. Volumetric source distribution along the stagnation streamline.

surrounding gas. The particles imparted work on the flowfield, increasing the momentum in the flight direction, but energy was pulled from the gas by the strong heating sustained by the particle. This heating was much larger in magnitude than the work imparted by the particles, resulting in an overall decrease in energy in the gas phase. These trends, which are amplified in the boundary layer region due to the locally increased relative velocity between the particles and surrounding gas, had a somewhat counteracting effect for convective heating. Boundary layer thickness was decreased by the momentum addition, but boundary-layer edge temperature was reduced. Figure 6.22 shows that the source field had little spatial variation in the stagnation region. Ultimately, this case demonstrated that the effect of two-way coupling was dependent on the thickness of the shock-layer with respect to the particle momentum relaxation distance. Even for high dust loading values, when the shock layer thickness is much smaller than the particle momentum relaxation distance, two-way coupling will have little effect on the flowfield and convective heating. This is consistent with the predicted coupling potential factor of 0.011 for this case.

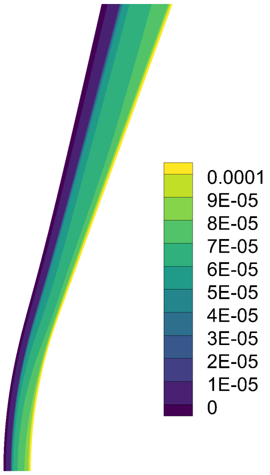

Figure 6.22. Volumetric source field for x-momentum in the stagnation region.

Figure 6.23 gives the surface recession rate distribution due to particle impacts, for both the baseline and exaggerated dust loading conditions. At extreme dust loadings such as 1%, the recession rate by dust impact is over one-order of magnitude larger than the thermo-chemical ablation rate observed over Mars entry vehicles at similar conditions [10]. The effect of two-way coupling is even smaller on surface erosion predictions, with the solutions for one and two-way coupling not demonstrating any significant distinction. Even for high dust loading the effect is negligible, as the shock layer parameters like velocity and temperature are only slightly changed. Figure 6.24 shows the percentage increase in recession rate by particle impact by the two-way coupled solution as compared with one-way coupling.

6.3. RADIATION INTERACTION BETWEEN PARTICLES AND HIGH TEMPERATURE SHOCK-LAYERS

In this section, the interaction between the particle phase and gas radiation is studied. For Mars entry, two mechanisms are studied: scattering of gas radiative emission, and radiative emission by shock-heated particles. Dust particles may scatter radiation from the gas phase, affecting the intensity field through in- and out-scattering terms in Eqn. (5.4).

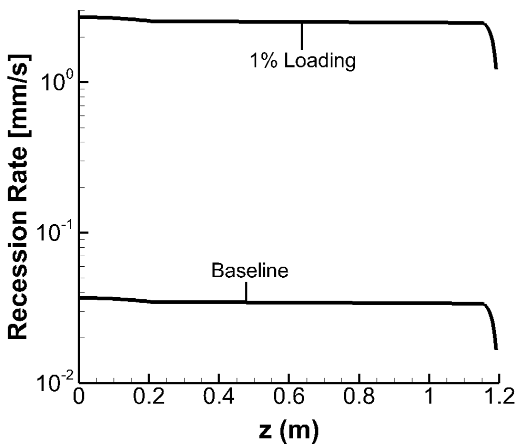

Figure 6.23. Surface recession rate for baseline and 1% loading conditions.

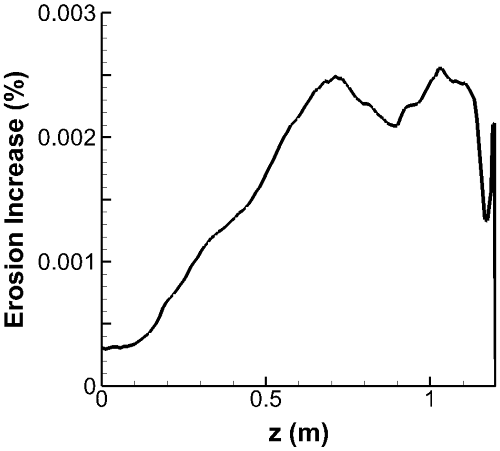

Figure 6.24. Increase in erosion at 1% loading when considering two-way coupling as compared with one-way coupled results.

Additionally, as small dust particles are heated to temperatures in excess of 3000 K [10, 35], emission can occur from the particle phase. Lastly, the potential for particulate vaporization products to affect gas phase emission is studied for Titan entry. As the Titan atmosphere contains a carbon-rich haze material [96, 97], vaporization of these particles can introduce more carbon into the flow and allow for increased emission.

The remainder of this section is presented as follows: In Section 6.3.1, analysis of the augmentation of radiative heat flux in Mars entry due to scattering by dust particles is presented, after which Section 6.3.4 presents an analysis of black-body radiative emission by shock-heated dust particles. Lastly, Section 6.3.5 presents analysis of the potential for Titan Haze particulate vaporization to influence gas radiative emission by introduction of additional carbon into the flow.

6.3.1. Description of the Problem. To determine the relative impact of radiation scattering in Mars entry scenarios, the scattering RTE is solved using the P_1 approximation using scattering coefficients derived from a continuum particle phase solution and Lorentz-

Table 6.8. Trajectory conditions for the Mars 2020 entry [73].

Time (s)	U_∞ (m/s)	ρ_∞ (kg/m^3)	T_∞ (K)	α (deg)
42.69	5387.60	1.10×10^{-5}	159.30	-15.78
60.61	5301.78	1.41×10^{-4}	156.42	-15.73
69.15	5079.60	3.90×10^{-4}	169.70	-15.77
73.99	4854.00	6.61×10^{-4}	175.41	-15.71
76.76	4681.40	8.80×10^{-4}	174.90	-16.42
82.00	4280.86	1.41×10^{-3}	177.85	-16.26
88.40	3630.81	2.17×10^{-3}	185.18	-16.74
90.00	3470.46	2.35×10^{-3}	186.50	-16.66
92.67	3210.88	2.64×10^{-3}	188.79	-16.86
99.65	2605.09	3.35×10^{-3}	190.95	-17.14
105.02	2229.64	3.71×10^{-3}	193.97	-17.38
115.28	1710.00	4.15×10^{-3}	194.60	-17.93
130.09	1261.13	4.30×10^{-3}	194.61	-18.38

Mie theory. Comparisons between the scattering and non-scattering solutions of the P_1 radiation solver will be used to determine the degree of augmentation likely to occur in a dust storm scenario.

For this problem, the entry trajectory of the Mars 2020 vehicle is studied due to the moderate entry velocity and vehicle size. The nominal dust conditions studied in this problem are based again on the July 2007 global dust storm measurements [10, 35], because these conditions represent a severe scenario. The trajectory points of interested are selected by observing the surface radiative heat flux and the freestream dust particle number density over the course of the trajectory and selecting points where both values are high. Table 6.8 gives the conditions for the Mars 2020 trajectry [73]. Each trajectory point was simulated using LAURA coupled with the HARA radiation tool to determine the time range in which the radiative heat flux pulse occurs. Figure 6.25a shows the surface radiative heat flux at two points on the vehicle forebody surface. The radiative heat flux history in Figure 6.25a indicates that the peak of the radiation pulse occurs between 88.40 to 92.67 seconds. Comparing these times in the trajectory with the effective freestream particle number density based on the July 2007 storm conditions, shown in Figure 6.25b, indicates

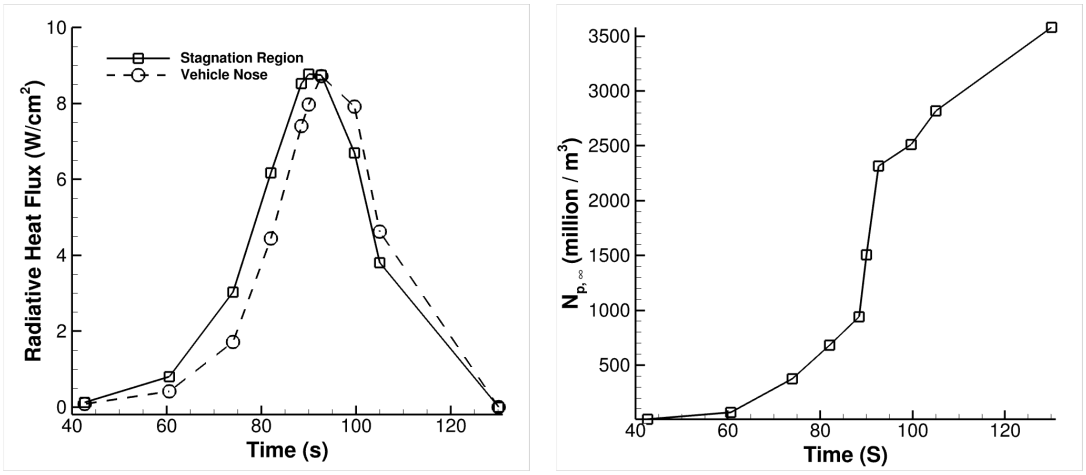

(a) Radiative heating.

(b) Freestream particle number density.

Figure 6.25. Radiative heating at various forebody surface points (left) and effective freestream particle number density (right) over the Mars 2020 trajectory given in Table 6.8.

that later times are more likely to have scattering impact by inspection of Eqn. (5.11), where the number density directly controls the strength of the scattering and absorption coefficients. As the 99.65 seconds point has both high particle loading and moderate radiative heat flux relative to the heat flux pulse, this trajectory point is the subject of study as well.

For each of the considered trajectory points in this study, the gas solution was performed using LAURA. A two-temperature, 10-species Mars gas model (CO_2, CO, N_2, O_2, NO, C_2, CN, C, N, O) was used in the current study. The flow was assumed to be turbulent, and the SA-Catris turblence model was employed [92, 98]. Two multi-block structured grids were used; one limited to the vehicle forebody, and another containing the wake region. For each grid, all blocks have cell dimensions of 12x12x64 (streamwise, transverse, and body normal directions, respectively). The forebody grid contains 48 blocks for a total of 442,368 cells. The wake grid contains 192 blocks for a total of 1,769,472 cells. The LAURA grid adaptation algorithm was used to cluster cells near shocks and the vehicle surface for each case. Figure 6.26 shows the computational grids used in the current study, with the forebody-only grid consisting of only the orange blocks.

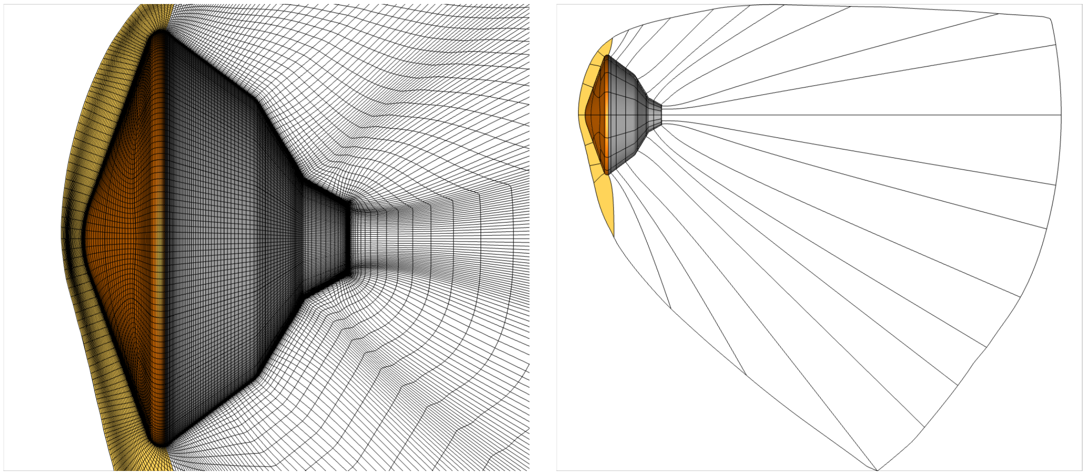

(a) Grid points (y>0 shown).

(b) Topology

Figure 6.26. Computational grids for the Mars 2020 cases. Grid points (left) and block topology (right) are shown, with forebody-only grid consisting of only the orange blocks.

The particle phase solution for each trajectory point was produced using the continuum particle phase methodology described in Section 4. As discussed in Sec. 6.1, Martian dust is polydisperse in nature and it is necessary to treat the size distribution of particles appropriately. To minimize the overall cost of the analysis, a quadrature scheme was used to integrate quantities over the particle size distribution. The quadrature scheme was derived by manipulating the modified gamma function particle size distribution commonly used for Mars dust problems such that it followed the form of generalized Gauss-Laguerre quadrature [99]:

$$F = \int_0^\infty y^\alpha e^{-y} f(y) dy. \tag{6.37}$$

where $f(y)$ is a general function. The quadrature points are the roots of the associated Laguerre polynomials, $L_n^\beta(x)$. Some transformation was necessary to fit the model integral when applied to a function weighted by the mass fraction function, Eqn. (6.5), such as follows:

$$F = \int_0^\infty f(r_p) \frac{r_p^5}{T_M} \exp\left[-\frac{\alpha}{\gamma}\left(\frac{r_p}{r_m}\right)^\gamma\right] dr_p, \tag{6.38}$$

By replacing the argument of the exponential function in Eqn. (6.38) with the following parameter:

$$y = \frac{\alpha}{\gamma}\left(\frac{r_p}{r_m}\right)^{\gamma}, \tag{6.39}$$

the integral was transformed to:

$$F = \frac{r_m^{4+\alpha}}{\alpha T_M}\left(\frac{\gamma}{\alpha}\right)^{\frac{4+\alpha-\gamma}{\gamma}} \int_0^{\infty} y^{\frac{4+\alpha-\gamma}{\gamma}} \exp\left(-y\right) f(y) dy. \tag{6.40}$$

The integral was then approximated using Gauss-Laguerre quadrature:

$$F \approx \sum_{i=1}^{n} W_i f(r_i), \tag{6.41}$$

where w_i and x_i are the transformed quadrature weights and evaluation radii, respectively. The evaluation radii, r_i, are the inverse of the tranformation variable, y:

$$r_i = r_m\left(\frac{\gamma y_i}{\alpha}\right)^{\frac{1}{\gamma}}, \tag{6.42}$$

while the transformed quadrature weights are as follows:

$$W_i = \left[\frac{r_m^{4+\alpha}}{\alpha T_M}\left(\frac{\gamma}{\alpha}\right)\right]^{\frac{4+\alpha-\gamma}{\gamma}} \left[\frac{\Gamma(n+\delta+1) y_i}{n!(n+1)^2\left[L_{n+1}^{\delta}(y_i)\right]^2}\right], \tag{6.43}$$

where δ is equal to the following:

$$\delta = \frac{4+\alpha-\gamma}{\gamma} \tag{6.44}$$

For a given number of quadrature points, n, the values y_i are the roots of the associate Laguerre polynomial of order n, L_n^{δ}. A useful result of this quadrature scheme was found to be that for a single quadrature point, the radius at which the entire integral is best approximated by a single particle size can be computed analytically as a function of

Table 6.9. Quadrature evaluation radii and associated weights for n=5.

r_i (μm)	w_i (m/s)
0.80761905065360	0.0865925109268390
2.16819134154875	0.4783572994724601
4.69372909431763	0.3792800917209281
9.27163724957803	0.0548508086656207
18.0588232639020	0.0009192892143021

the parameters of the distribution. The optimized single point evaluation radius was found to be the following:

$$r_{\text{opt}} = r_m \left(\frac{4+\alpha}{\alpha}\right)^{\frac{1}{\gamma}}. \tag{6.45}$$

To determine the number of quadrature points to use, the freestream scattering coefficient was computed using various distribution assumptions. The scattering coefficient was computed with Eqn. (5.11) based on the freestream particle number density conditions for a representative trajectory condition assuming a modal radius of 0.35μm for the particle size distribution. Figure 6.27 shows that assuming a constant distribution based on the mass-averaged particle radius severely underpredicts the reference spectrum, which was computed with trapezoidal integration over a total of 1000 radii. Instead, the Mars gamma distribution quadrature rule recovers the reference solution much more accurately with only 5 radii considered. While increasing the quadrature point count to 10 improves the solution further, 5 points was found to be sufficiently accurate while minimizing the number of independent particle solutions necessary. Accurate treatment of the distribution is particularly important within the shock layer as the number density of small particles can rise multiple orders of magnitude, causing the size distribution to vary strongly from the freestream. In the current study, the 5 point quadrature integration rule, given by Eqn. (6.41), is utilized with the evaluation radii and weights given in Table 6.9 to integrate any quanities weighted by the particle size distribution.

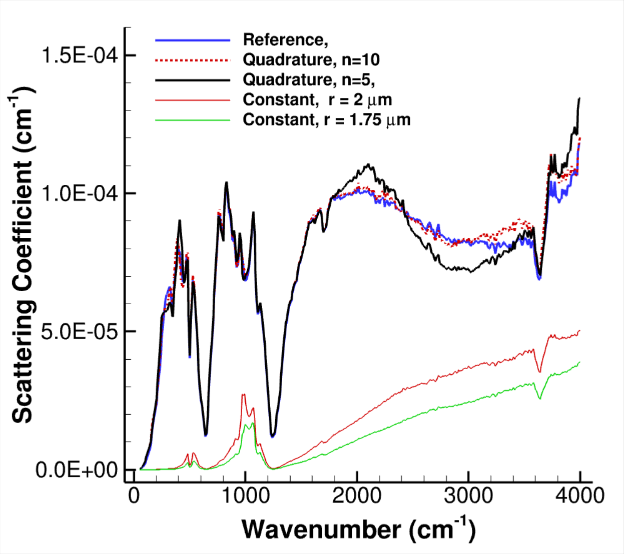

Figure 6.27. Scattering coefficient for Mars dust assuming a modal radius of 0.35 μm. Comparison of various distribution models with a reference solution.

For each trajectory point considered, the continuum particle phase solver was used to treat the evaluation radii in Table 6.9 individually. For each radius, the particle phase is assumed monodisperse, with the density of the phase consisting of only particles of the given radius. The density is the product of the gas density and the mass mixing ratio, β. After simulating each radius, quantities which are integrated over all particle radii weighted by the particle size distribution are computed using the quadrature rule described above. Table 6.10 gives the freestream particle phase mass mixing ratio and density used for each case considered in the current study.

Table 6.10. Freestream particle phase mass density for cases considered in this study.

Time (s)	$\rho_{p,\infty}$ (kg/m^3)	β
88.40	1.5148×10^{-7}	6.9808×10^{-5}
90.00	1.6409×10^{-7}	6.9827×10^{-5}
92.67	1.8449×10^{-7}	6.9884×10^{-5}
99.65	2.3411×10^{-7}	6.9884×10^{-5}

Table 6.11. Maximum number density ratios observed for each trajectory point and particle size.

Trajectory Time (s)	0.81 μm	2.17 μm	4.69 μm	9.27 μm	18.1 μm
88.40	96.6	5.47	1.72	1.27	1.13
90.00	54.7	6.94	1.79	1.29	1.14
92.67	51.7	13.3	1.93	1.33	1.16
99.65	25.7	176.3	2.31	1.41	1.19

Figure 6.28 shows two particle phase number density solutions for the 99.65 second trajectory point, in which the ratio of the number density field to the freestream number density is shown for the shock layer symmetry plane and vehicle forebody surface. Generally, the number density is highest in the stagnation region where particles slow down significantly due to high shock-layer thickness, while on the leeside surface the particle number density is much lower as particles retain more of their momentum. These features vary significantly with the particle size as can be seen in Figure 6.28. Table 6.11 lists the maximum number density in the domain for each number density and trajectory condition considered. The relationship between number density and momentum loss in the shock-layer is illustrated further in Figure 6.29a, where small particles were observed to pack in together due to their fast momentum loss. Computing the distribution weighted average number density using the quadrature technique described above yields the solid curve in Figure 6.29a. The distribution weighted average number density is not used directly in analysis, but is useful in determining the relative impact of various radii and trajectory points on the scattering coefficients to be presented after. Figure 6.29b compares the distribution weighted average number density along the same line for various trajectory points, showing that the number density profiles are largely comparable through the duration of the heat pulse.

6.3.2. Scattering Optical Properties. As the P_1 radiation solver requires each wavenumber to be considired in isolation, it was important to focus analysis on the most imporant regions of emission. To determine the key emitting wavenumbers for the Mars

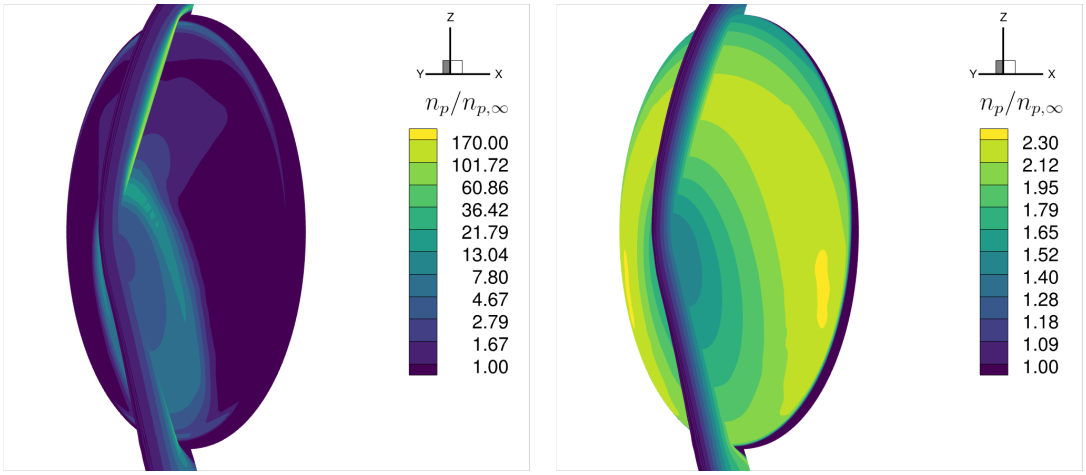

(a) 2.17 μm.

(b) 4.69 μm.

Figure 6.28. Particle number density ratio to freestream on the symmetry plane of the domain and the vehicle surface for 2.17 μm (left) and 4.69 μm (right) particles for the 99.65 second trajectory point.

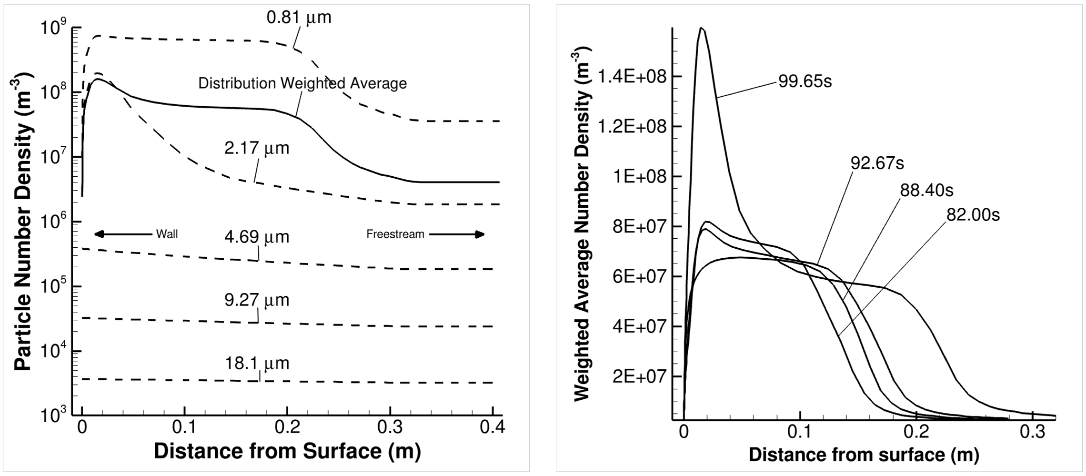

(a) 99.65 seconds.

(b) All trajectory points.

Figure 6.29. Comparison of number densities along a line sample normal to the vehicle surface in the stagnation region. Comparison of individual radii for the 99.65 second trajectory point (left) and comparison of weighted average number density at each trajectory point (right).

entry enviroments. Figure 6.30 shows the emission spectra for the 90s trajectory point, sampled at a location near the normal portion of the vehicle's bow shock. By inspection, the emission peaks strongly at a wavenumber of approximately 2200 cm^{-1}, with much

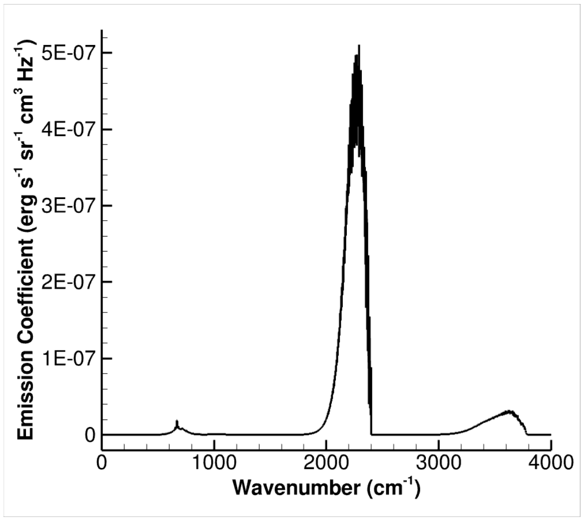

Figure 6.30. Emission spectra of the Mars 2020 90s trajectory point at a location near the normal portion of the bow shock.

weaker peaks at approximately 3600 and 675 cm^{-1}. As the emission for this case is quite narrowly focused near 2200 cm^{-1} and no significant variation in scattering optical properties occurs over the band, this wavenumber will be focused on in isolation.

To perform the scattering radiation analysis, the scattering coefficient, particle phase absorption coefficient, and phase function information are necessary. Following the discussion in Section 5.2, the results of Lorentz-Mie theory are used to compute these quantities from the particle phase by leveraging the spherical particle assumption. For each discrete radius simulated according to the previous discussion, the scattering and absorption efficiency factors are computed using Eqn (5.6a) and scaled by the cross sectional area and number density of the particles for that radius. Then, the quadrature rule described above is used to integrate the mass-fraction weighted integral of the radially-dependent coefficients. Figure 6.31 shows the variation of the scattering optical coefficients, σ_{sca}, σ_{ext}, and κ_p, based on a representative freestream condition using the 5 point quadrature rule described above. The scattering optical properties for the representative condition shown in Fig-

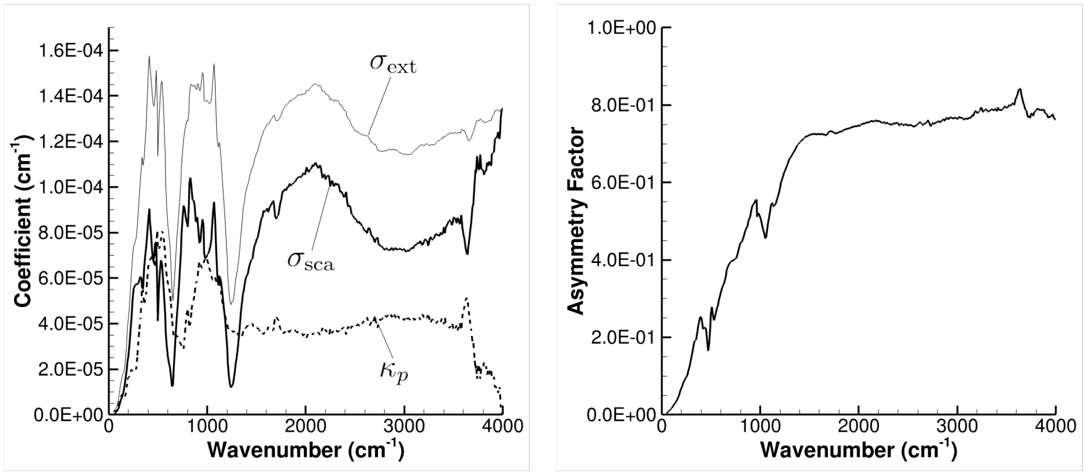

(a) Scattering, absorption, and extinction.

(b) Asymmetry factor.

Figure 6.31. Scattering optical properties (left) and asymmetry factor (right) for Mars dust assuming a modal radius of 0.35 μm, integrated using the 5 point quadrature rule.

ure 6.31 indicate that at the wavenumber of interest, 2200 cm^{-1}, the particle phase is weakly absorbing relative to its scattering potential, and scatters 72% in the forward direction as indicated by Figure 6.31b.

For scattering radiative transport, the scattering albedo is often used as a nondimensional measure of the relative magnitude of the scattering coefficient to the total loss, or extinction, coefficient:

$$\omega = \frac{\sigma}{\beta} = \frac{\sigma}{\kappa_g + \kappa_p + \sigma}, \tag{6.46}$$

where σ, κ_g, and κ_p are the scattering, gas phase absorption, and particle phase absorption coefficients, respectively. For a purely scattering medium ($\kappa_g = \kappa_p = 0$), the albedo would have a value of one, while a value of zero implies a purely absorbing medium. Except for shadow regions behind a vehicle, everywhere in the domain has a non-zero scattering coefficient. As the scattering coefficient increases linearly with particle number density, it reaches a maximum within the shock layer due to particles losing velocity due to drag. Despite the scattering coefficient being higher within the shock layer, the scattering albedo is reduced in this region due to the sharp rise in gas phase absorption coefficient for

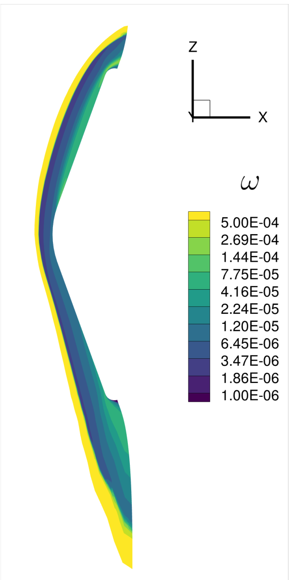

Figure 6.32. Scattering albedo on the symmetry plane for the 99.65 second trajectory point of Mars 2020.

conditions of interest. For example, because the high temperature gas absorbs strongly at the wavenumber of 2200 cm^{-1}, the albedo is dominated by the gas absorption. Figure 6.32 demonstrates the albedo for the 99.65 second trajectory point along the symmetry plane of the forebody shock layer, showing that much of the shock layer has an albedo value multiple orders of magnitude smaller than the freestream. The albedo rises near the stagnation region of the vehicle surface and vehicle shoulders due to the high number density of small particles (radii of less than $2\mu m$), but reaching still a fraction of the freestream value. Figure 6.33 compares the scattering albedo, ω, along line samples normal to the vehicle suface in the stagnation region. The profiles indicate that the albedo profile is largely consistent over the trajectory points considered in the current work, with the 99.65 seconds trajectory point having a much higher relative albedo level near the surface.

6.3.3. Radiative Heat Flux Augmentation by Scattering. Using the scattering properties presented in the previous section, the radiative heat flux was computed using the P$_1$ radiation solver first for the gas phase in isolation, and next with the scattering terms included. The change in this heat flux is referred to here as the radiative heat flux

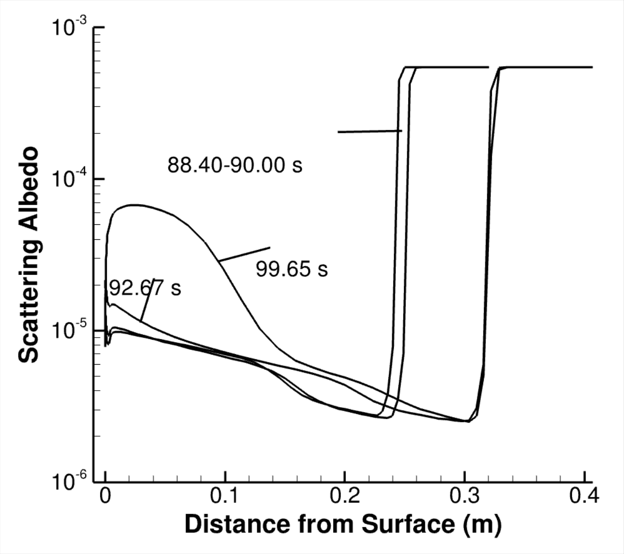

Figure 6.33. Scattering albedo profiles along a surface-normal line in the stagnation region compared between trajectory points.

augmentation. Figure 6.34 compares the radiative heat flux augmentation by scattering at nominal dust loading conditions on the symmetry plane of the vehicle. The primary result is that the maximum augmentation level is negligibly small. Additionally, the profiles in Figure 6.34 do not correlate closely with the profiles of the gas radiative heat flux or freestream particle number density histories given in Figure 6.25, which indicates that the scattering augmentation predicted with the present assumptions is very localized in space. This is further supported by observation of the ratio of particle number density compared to the freestream condition at the vehicle surface for 2.17 μm radius particle at the 99.65 second trajectory point in Figure 6.28a correlates closely with the augmentation for this trajectory point. Augmentation is much higher near the stagnation region where the particle number density is high just away from the surface.

While the nominal dust loading results indicate that radiative heat flux augmentation due to scattering is negligible, it is important to note that some uncertainty in the dust presence exists for lower altitudes. As the Mars reconnaissance orbiter is not able to measure all the way to the surface during storm conditions, the dust loading is extrapolated

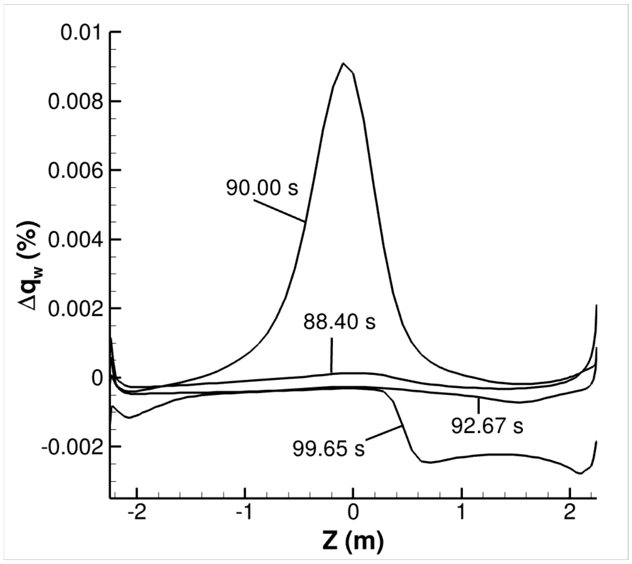

Figure 6.34. Relative change in surface radiative heating due to scattering with nominal dust content for the considered cases, sampled along the symmetry plane of the vehicle.

from the last measurement down to the surface using the Conrath equation [10]. In the case of the July 2007 global storm, measurements are only available down to 37.5 km [10]. The portion of the trajectory considered in this study occurs at an altitude of approximately 16 to 18 km, which is significantly lower than the measurement cutoff for the MRO data. As potentially high uncertainty exists in the dust loading profile at these altitudes, the behavior of the augmentation with dust loading is of interest in the current study. A detailed investigation of the uncertainty in low altitude dust loading is outside the scope of the current study. Instead, the senstivity of the current results with increasing dust loading is studied to assess the likelyhood that uncertainty in dust loading could affect potential radiative heat flux augmentation. To determine this sensitivity, the nominal freestream dust loading value for each condition was multiplied by values of 10 and 100 and the heating augmentation was recomputed. Figure 6.35 shows the symmetry plane profile of heating augmentation by scattering at 100 times the nominal loading for each trajectory point. Figure 6.36 shows the surface contours of augmentation at 100 times nominal dust loading for the 99.65 second trajectory point, which is the highest augmentation observed on the forebody in the

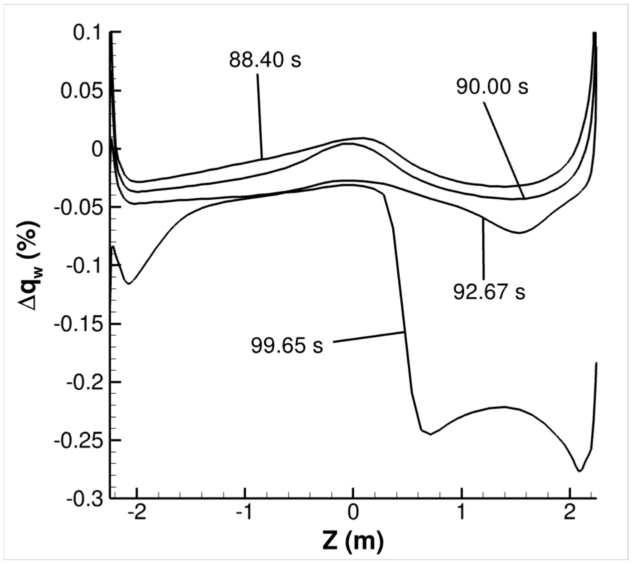

Figure 6.35. Relative change in surface radiative heating with 100×nominal dust content for the considered cases, sampled along the symmetry plane of the vehicle.

current study. Comparison with the nominal loading augmentation profiles in Figure 6.34 shows that increasing the dust content generally results in a reduction of radiative heating, though the trends vary somewhat between the trajectory points. Table 6.12 lists the bounds of radiative heat flux augmentation observed on the vehicle forebody for various loading levels.

Observation of the vehicle wake shows higher albedo levels than the forebody shocklayer due to relatively high particle number density and reduced gas absorption, shown in Figure 6.37 for the 99.65 second trajectory point. Unlike the forebody shock layer, some wake regions have albedo values exceeding the freestream value, indicating much stronger

Table 6.12. Forebody radiative heat flux augmentation bounds for all trajectory points and loading conditions considered.

Loading Level	Augmentation Bounds (%)
Nominal	[-0.0028, 0.0091]
10×Nominal	[-0.0277, 0.0088]
100×Nominal	[-0.2761, 0.0090]

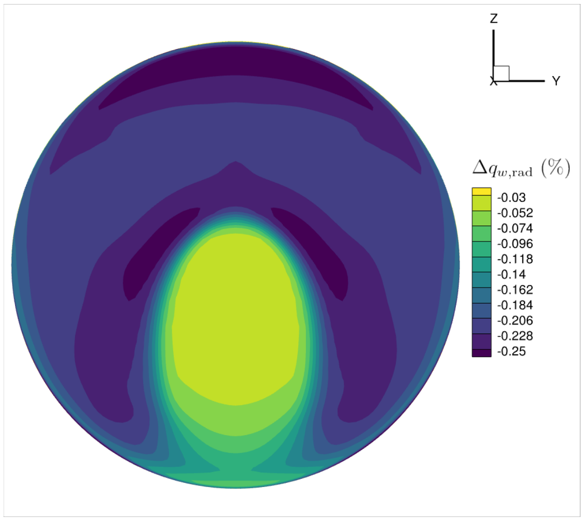

Figure 6.36. Percent augmentation of the surface radiative heating predicted for the 99.65 seconds trajectory point with 100 times nominal dust loading.

local scattering effects than in the forebody region. To determine if these high local albedo regions impact the backshell radiative heating solution, the present methodology was applied to the full vehicle grid including the wake region shown in Figure 6.26b. Under nominal loading conditions, it was found that the 99.65 second trajectory point has much higher augmentation than the earlier points in the trajectory, with comparable augmentation to the forebody results shown before. Figure 6.38 compares the symmetry plane augmentation profile for the nominal dust loading conditions. Similar to the forebody results, augmentation at elevated loading conditions was predicted for vehicle backshell at the 99.65 second trajectory. Similar trends in the augmentation were observed at elevated loading, with bounds summarized in Tab. 6.13. The results indicate that though still small, the predicted augmentation is higher on the backshell using the present methodology but still negligible.

As mentioned in Section 5.4, distant emission sources can be represented inaccurately in the P_1 approximation due to the low number of terms retained in the spherical harmonics expansion of the intensity field. For radiative heat flux augmentation on the backshell, much of the potential influence of scattering originates relatively far from the

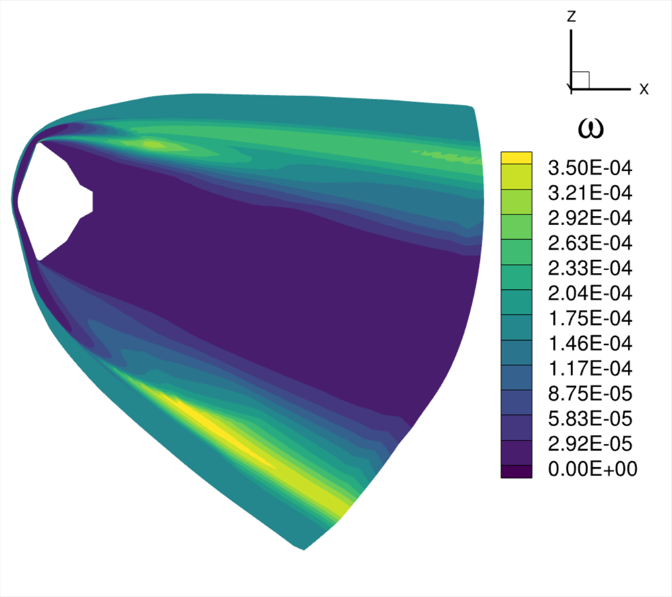

Figure 6.37. Scattering albedo, ω, shown on the symmetry plane for the 99.65 second trajectory point.

vehicle surface as shown in Figure 6.37. To investigate the potential error in backshell radiative heat flux augmentation due to the P_1 approximation, a hybrid P_1-ray-tracing scheme was developed to reduce the error compared with the P_1 approximation on its own. The hybrid P_1-ray-tracing scheme treats the in-scattering integral of the RTE using information from a P_1 radiation solver solution, while all other terms are treated with the ray-tracing result. As the ray-tracing technique solves the RTE along a line of sight pseudo-exactly, these portions of the hybrid-solution will be solved much more accurately than the pure P_1 result. Any error in the P_1 solution will be isolated to the in-scattering integral, causing the

Table 6.13. Backshell radiative heat flux augmentation bounds for all trajectory points and loading conditions considered.

Loading Level	Augmentation Bounds (%)
Nominal	[-0.004, 0.001]
10×Nominal	[-0.039, 0.012]
100×Nominal	[-0.360, 0.115]

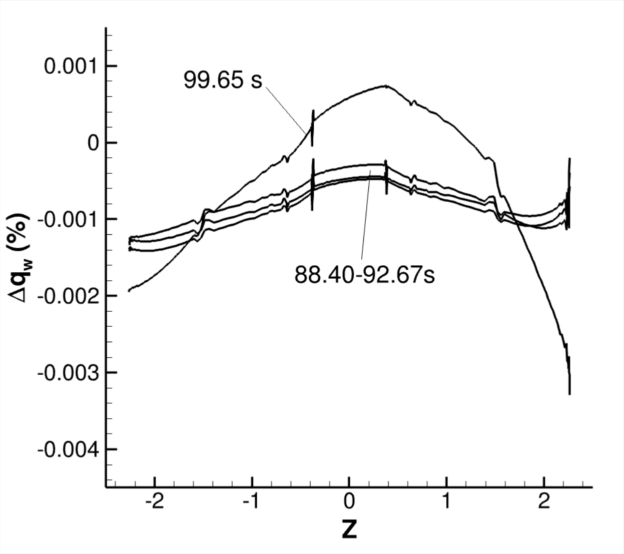

Figure 6.38. Scattering augmentation of backshell surface radiative heating for nominal dust loading.

hybrid P_1-ray-tracing solution to have lower error than the P_1 solution in isolation. Recall the RTE (frequency subscripts are dropped):

$$\frac{\partial}{\partial s} I(s,\Omega) + \{\kappa(s) + \sigma(s)\}\, I(s,\Omega) = j(s) + \frac{\sigma(s)}{4\pi} \int_{4\pi} I(s,\Omega')\Phi(\Omega,\Omega')d\Omega'. \tag{5.4}$$

As the intensity field can be represented as a function of the P_1 radiation solver solution, as shown in Eqn. (5.29), the in-scattering integral on the right hand side of Eqn. (5.4) can be computed. For the hybrid scheme, the in-scattering integral was computed as a source field added to the emission coefficient field. The intensity represented with the P_1 radiation solver solution,

$$I(\vec{x},\hat{s}) = \frac{1}{4\pi}\left[G(\vec{x}) + 3\mathbf{q}(\vec{x}) \cdot \hat{s}\right], \tag{5.29}$$

and scattering phase function, given by Eqn. (5.9), are substituted into the in-scattering integral. Replacing terms which arise that contain the dot product of the line of sight direction, $\hat{s}$, and incident directions, $\hat{s}'$, with the definition of the dot product and simplifying

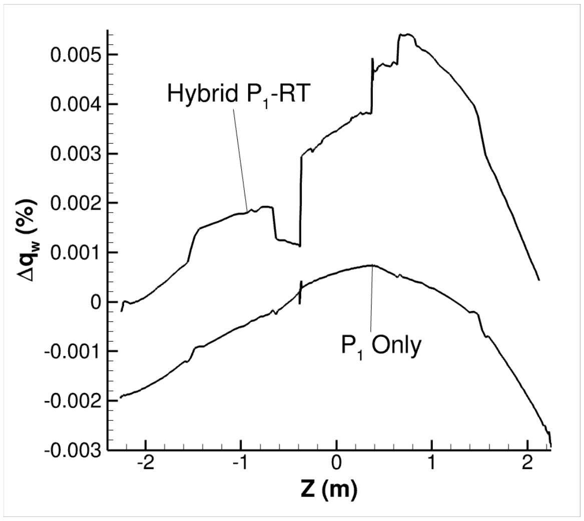

Figure 6.39. Comparison of backshell radiative heat flux augmentation computed with the hybrid P_1-ray-tracing scheme and P_1 radiation solver for the 99.65 second trajectory point for nominal dust loading.

results in the following in-scattering source:

$$S = \frac{\sigma}{16\pi}\left[4G(\hat{x}) + 3g\pi\,\|\vec{q}(\hat{x})\|\right]. \tag{6.47}$$

The ray-tracing methodology described in Section 5.3 was applied to solve the hybrid P_1-ray-tracing scheme and compared with the P_1 radiation solver alone in Figure 6.39. The results show that the redirected intensity scattered towards the backshell was underpredicted with the P_1 approach as the additional intensity was from a distant location. Despite this, the hybrid P_1-ray-tracing solution still predicted a small augmentation. As the hybrid P_1-ray-tracing solution has lower error than the P_1 solution, the results in Figure 6.39 give additional confidence that scattering is unlikely to produce significant augmentation in Mars entry scenarios.

6.3.4. Blackbody Radiation from Shock-Heated Particles in Mars Entry. The next mechanism studied for particle-radiation interaction is blackbody emission from the particle phase. In Mars entry, it has been shown that particles heated within the shock-layer may reach temperatures sufficient to result in vaporization, which can exceed 3000 K [10, 35]. At high temperatures, the blackbody radiation may result in an augmentation source to the surface radiative heat flux. In this section, an analysis of the extent to which the dust presence and temperatures contribute to augmentation by blackbody radiative emission.

To perform this analysis, the gas and particle phase solutions used in the previous section were used. The emission coefficent was computed from each particle phase solution by first assuming that no absorption occurs from the gas phase. This allows the emission to be computed for the entire spectral range, rather than requiring a spectrally resolved emission coefficient. Under this assumption, the emission power from a single particle is found using Stefan-Boltzmann law:

$$\dot{Q}_{b,p} = A_{s,p} \epsilon \sigma T_p^4, \tag{6.48}$$

where $A_{s,p}$ is the particle's surface area, ϵ is the emissivity, and σ is the Stefan-Boltzmann constant. In the current work, the emissivity for each particle is estimated to be 85% [100, 101]. Multiplying by the number density of particles, n_p, and dividing by the total speherical solid angle of 4π results in the emission coefficient:

$$j_{b,p} = \frac{n_p Q_{b,p}}{4\pi} = n_p r_p^2 \epsilon \sigma T_p^4. \tag{6.49}$$

Similar to the scattering optical coefficients in Section 6.3.2, the emission coefficient is integrated over the particle size distribution using the 5 point quadrature rule discussed in the previous section. Figure 6.40 shows the emission coefficient for the 99.65 second trajectory point of the Mars 2020 case assuming nominal dust loading conditions, computed using Eqn. (6.49) and the 5 point quadrature rule. Due to the strong temperature dependence of the emission coefficient, the emission in the forebody region is signficantly higher than in the wake region where particles begin to cool.

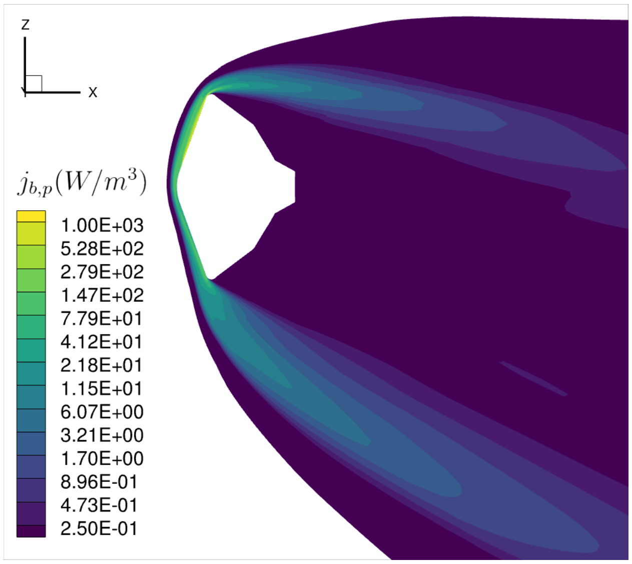

Figure 6.40. Emission coefficient for the 99.65 second trajectory point shown on the symmetry plane of the domain.

Using the ray-tracing methodology described in Section 5.3, the heating to the surface was computed. A total of 10 polar angles and 10 equatorial azimuthal points were used, which equates to a total of 58 approximately uniformly distributed rays samples at each surface location. Figure 6.41 shows the heating profiles for each trajectory point considered in the current study, demonstrating that heat flux due to particle phase blackbody emission is negligible relative to the nominal gas-only radiative heat flux which is O(10) W/cm^2 as shown in Figure 6.25a.

6.3.5. Gas Emission Augmentation by Haze Particle Vaporization in Titan Entry. In recent years, Titan has been a destination of interest for scientific missions, and analysis of entry into the Titan atmosphere has been more common [59]. Similar to Mars and other planetary bodies in the solar system, the Titan atmosphere contains particulates at high altitudes. In the case of Titan, atmospheric haze particles are composed of agglomerated organic monomers [96]. The haze particles form high in the atmosphere and increase in size as they fall toward the surface of Titan [96]. To determine the relationship between the atmospheric density and the haze quantity through the atmosphere, the ratio of haze density

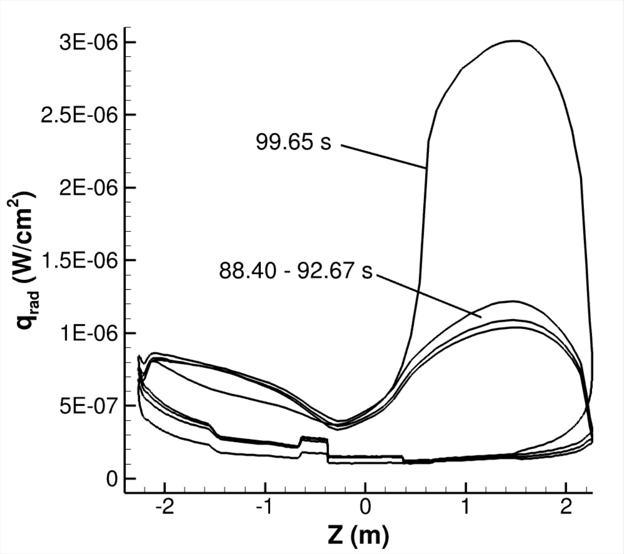

Figure 6.41. Comparison of emission profiles on the vehicle symmetry plane for different trajectory points.

to gas density was computed using the haze model of Ref. [96]. The haze density was computed by assuming spherical particles with a density of 1000 kg/m^3 [96] and computing their mass based on the effective spherical radius profile given in Ref. [96]. Multiplying the mass and number density profile of the haze, and dividing by the density of the gas phase results in the haze particle loading. Using the nominal density profile given in Ref. [102], the haze mass loading was computed. Figure 6.42 shows the mass loading of Haze in Titan's atmosphere as a function of altitude. Through much of the atmosphere, the haze loading ratio was found to be quite small ($\beta << 1\%$), with the exception of a spike of nearly 0.147% at 460 km. As the haze particulates contain between 76 and 92% carbon [97], a comparison against the amount of methane present showed an increase of approximately 10% added carbon in the freestream. Since the haze particles at this atltitude have an equivalent spherical radius of approximtaely 0.4 μm [96], it is likely that the particles will heat up fast enough to vaporize within the shock-layer and increase the amount of carbon present for the formation of strong radiating species [59]. Detailed vaporization modeling for the haze particles is the subject of ongoing study.

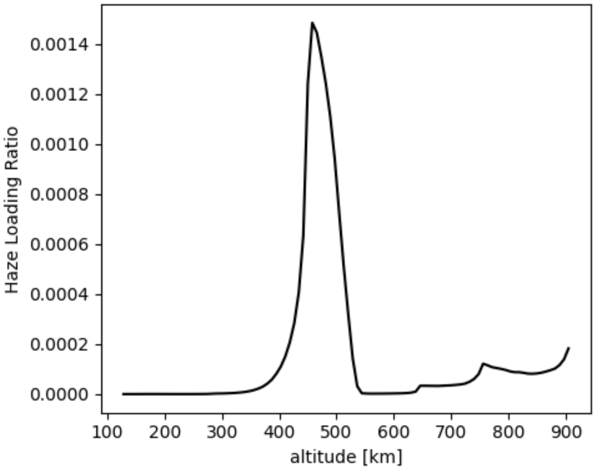

Figure 6.42. Haze mass loading ratio for Titan as a function of altitude.

For this case study, a representative Titan entry vehicle was considered, using conditions representative of a 460 km altitude trajectory point at 7.36 km/s [59]. To study the effect that haze particle vaporization may have on radiative heating, the gas phase was modeled using LAURA. The atmosphere was modeled with a two-temperature thermochemical nonequilibrium gas model consisting of the following species: N, C, H, N_2, CH_4, CH_3, CH_2, CH, H_2, C_2, NH, CN, HCN, CN^+, H^+, N^+, N_2^+, C^+, and e^- [59]. As a preliminary analysis, the haze particles were assumed to fully vaporize due to their small size and the high heating the particles experience in the shock layer. Under this assumption, the freestream density and mass fractions were changed to account for the elemental composition of the fully vaporized haze particulates. The freestream conditions

Table 6.14. Conditions for the 460 km Titan entry case.

V_∞ (m s^{-1})	ρ_∞ (kg m^{-3})	T_∞ (K)
7362.46	8.4824×10^{-6}	165.93

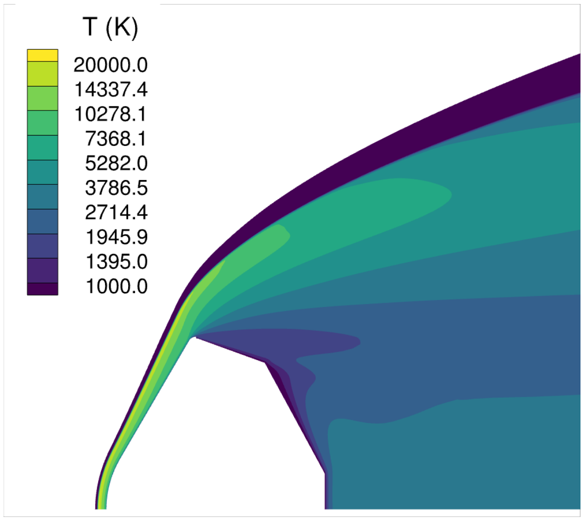

Figure 6.43. Translational temperature field for the nominal Titan 460 km case.

for the nominal and vaporized haze conditions are given in Tables 6.14 and 6.15, where c_i represents the mass fraction of species i imposed in the freestream. The radiation from the gas phase was computed with the HARA radiation code using a tangent slab model [74].

Figure 6.43 shows the translational temperature field for the nominal case, and Figure 6.44 shows the comparison between nominal and haze vaporization radiative heat flux along the symmetry plane of a representative Titan entry vehicle. As seen in Figure 6.44b, near the forebody shoulder an increase of nearly 3% is observed for the haze vaporization case, which is large relative to the quantity of haze in the atmosphere by mass. As this analysis assumes 100% vaporization of the particle phase however, in reality the result would be lower as this represents the upper bound of the augmentation.

Table 6.15. Mass fractions for the 460 km Titan entry case.

Case	c_{N_2}	c_{CH_4}	c_C	c_H	c_N
Nominal	0.9873	0.01270	0	0	0
Vaporized Haze	0.9859	0.01268	1.233×10^{-3}	1.035×10^{-4}	1.307×10^{-4}

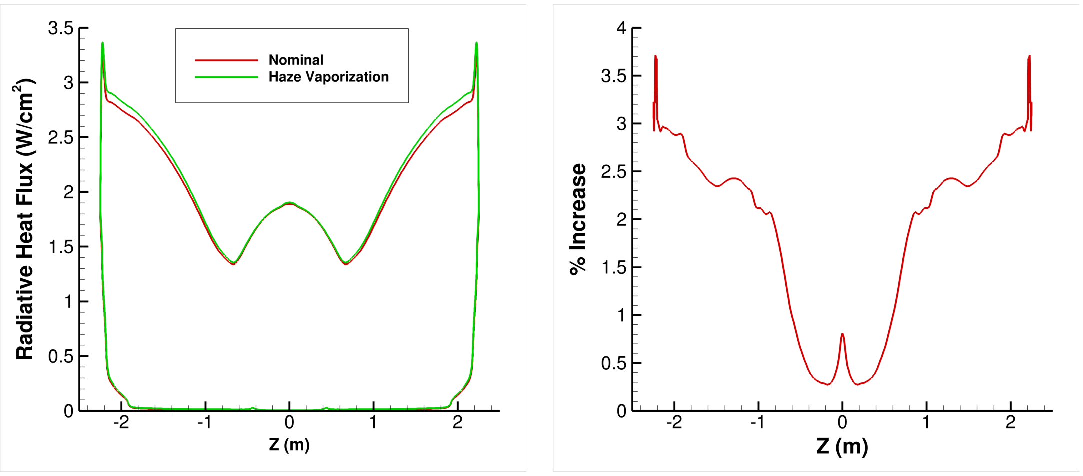

(a) Radiative heat flux.

(b) Increase due to haze.

Figure 6.44. Comparison of symmetry plane radiative heatinge (a) with and without haze vaporization and (b) percentage increase.

To determine the potential for vaporization, a haze particle trajectory was simulated along the stagnation streamline of the flowfield to determine the degree of vaporization which may occur for haze particulates at the 460 km condition. Table 6.16 lists the parameters of the haze particle simulation used in this analysis. Figure 6.45 shows the trajectory history of the stagnation streamline particle, which demonstrates that under the present assumptions, virtually no vaporization occurs. As seen in Figure 6.45c, haze particles maintain the majority of their initial momentum, minimumizing the residence time within the shocklayer. Due to the low gas density at these conditions, the drag a particle experiences is too low to result in long residence times which would lead to higher degree of vaporization. This analysis indicates that despite the large possible relative impact of additional carbon injection in the shock layer, the low vaporization degree releases a minimal

Table 6.16. Parameters used for Lagrangian tracing of Titan haze particles.

r_p (μm)	ρ_p (kg/m^3)	Cp_p (J/kg·K)	ζ (J/kg)	T_{vapor} (K)
0.5	1000	1000	10^6	2000.0

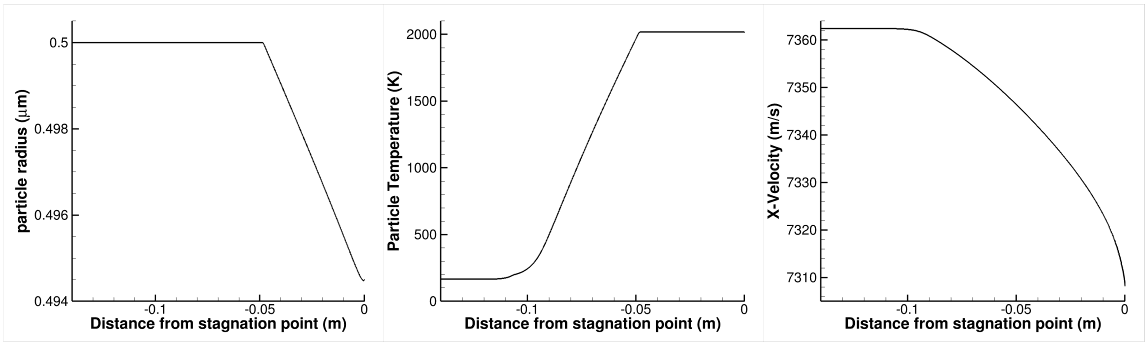

(a) Particle radius. (b) Particle temperature. (c) Particle velocity.

Figure 6.45. Trajectory history for a haze particle along the vehicle stagnation streamline. History of radius (left), temperature (center), and velocity (right).

amount and leads to a low augmentation. This result agrees with the analysis by Nelson [103], where it was shown that haze vaporization radiation products would be moderately, but not strongly detectable via radiometer measurements.

7. CONCLUSIONS AND FUTURE WORK

In this work, a series of computational techniques were developed for the efficient solution of particle-laden hypersonic flows using Lagrangian and Eulerian models with the focus on planetary entry applications. In specific, these methods were applied to the investigation of spacecraft surface erosion, convective and radiative heat flux augmentation due to atmospheric particulate encounter during planetary entry.

For Lagrangian models the TCV method was developed to efficiently integrate quantities of interest including surface erosion by dust impact in Mars entry. The TCV method was applied to a representative Mars entry problem with dust conditions based on a severe global dust storm scenario. Optimal particle samples counts required for the TCV method and MC technique were determined via a parametric study. Compared with MC, the TCV method required 3 orders of magnitude fewer particle samples (a reduction of >99.9%) to achieve an accurate result with no numerical noise. The TCV method was then applied to a representative Mars entry case to predict cumulative surface erosion by dust impact over a full trajectory at angle of attack. The cumulative surface erosion was shown to compare favorability with other works in the literature. The efficiency of the TCV method was further demonstrated by utilizing an NIPC-based UQ method to propagate uncertainties through the particle phase model, which required 330 independent phase solutions. Such an analysis would be infeasible with MC techniques due to the cost required to achieve noise free solutions necessary for NIPC-based UQ methods. The UQ and sensitivity analysis highlighted properties related to the Mars dust composition and size distribution model as important uncertainty contributors for surface erosion.

The TCV method was later extended to efficiently compute two-way coupling source terms using a sparsely sampled set of particles. A series of verification tests were performed which demonstrated that when coupled to a gas solver, the extended TCV method could accurately solve two-way coupled particle-laden hypersonic flow problems. The extended

TCV method was shown to produce nearly perfect agreement with a semi-analytical boundary layer solution for highly dusty supersonic flow over a flat plate. Additionally the developed methodology was shown to agree well with a dusty hypersonic shock tube experiment. Application of the present methodology to a representative Mars entry case showed that two-way coupling effects were negligible in predicting the level of convective heating and surface erosion. A coupling potential factor was developed to predict the strength of coupling for particle laden hypersonic blunt body flows. The coupling factor was shown to correlate strongly with the cases studied.

In addition to the TCV method, a particle phase solver based on an Eulerian model was developed for hypersonic flow problems. The continuum phase solver was verified against and shown to be equivalent to the Lagrangian technique under the same assumptions. The continuum particle phase solver was applied to the Mars 2020 spacecraft entry flowfield to predict the particle number density throughout the domain. Radiation scattering properties for the flowfield were computed using Lorentz-Mie theory based on the particle phase number density information. The scattering properties were integrated over all particle sizes using a highly efficient quadrature scheme for Mars dust size distributions. A radiation solver based on the P_1 spherical harmonics approximation was developed to solve the scattering form of the radiative transport equation. After verification of the P_1 radiation solver using MMS and exact solutions of the P_1 model, the solver was applied to the Mars entry case. The impact of scattering was shown to be small relative to the gas radiative heat flux ($<<1\%$), even at higher than nominal dust loading conditions. Further analysis showed that emission augmentation due to black-body radiation from shock-heated particles and injection of particle vaporization products was negligible. The results indicate that interaction between particles and gas radiation are particularly weak effects for both Mars and Titan entry scenarios studied.

The techniques developed in this work provided valuable insight into the aerothermodynamic interactions between the gas and particle phases for multiple planetary entry missions. The results demonstrated that for planetary entry problems with relevant conditions considered in this work, radiation interaction mechanisms can be safely neglected. The techniques developed in this work are however expected to contribute to other classes of hypersonic particle-laden flow problems such as radiation interaction in solid rocket plumes and coupling effects for Earth atmosperic hypersonic flight vehicles. Future study into Earth atmospheric hypersonic vehicles is warranted as larger scale slender bodies subjected particle-laden environments are likely to have more significant coupling effects than the Mars entry vehicle studied in this work. An aspect of these flight problems which was not studied in the current work is the sensitivity of aerodynamic quantities like lift and drag to particulate presence. Another future work item is to consider the reflection of particles from solid surfaces, which can be important for problems involving dusty wind tunnels or shock tubes as well as lower speed hypersonic flight conditions on slender vehicles. Particle interactions with scramjet flowpaths also warrant study using the techniques developed in this work.

APPENDIX

DIFFERENTIAL LIMIT FORMULATION OF THE TRAJECTORY CONTROL VOLUME METHOD

The noncontiguous form of the TCV method, in which TCVs are formed without sharing particle trajectories between them, can be extended by utilizing a differential limit formulation. In this section, the extension of the TCV method to a pseudo-exact technique, by taking the limit of dilation factor as particle spacing approaches zero, is described. Taking this limit allows the dilation factor to be computed using a single particle trajectory and its gradients with respect to the initial position. The differential limit formulation begins by defining a TCV with a particle, and two fictitious particles perturbed by a small distance, h, in two orthogonal directions, $\hat{e}_1$ and $\hat{e}_2$, as shown in Figure 1.

These fictitious particles, if traced through the domain alongside the real particle, would be perturbed similar to the initial locations, as shown in Figure 1 on the right. Defining the location of a particle as a function of time along the trajectory and initial location as $p(x,t)$, the area of the region swept by the particles at time t is as follows:

$$A(t) = \frac{1}{2}\left\|(p(\vec{x}+h\hat{e}_1,t) - p(\vec{x},t)) \times (p(\vec{x}+h\hat{e}_2,t) - p(\vec{x},t))\right\|, \tag{1}$$

where $\|.\|$ denotes the L_2-norm of a vector. It should be noted that at the initial location, where $t = 0$, the area is $h^2/2$. Computing the dilation factor using these definitions results in the following expression:

$$f_D(t) = \frac{A_U(t)}{A_I(t)} = \left\|\left(\frac{p(\vec{x}+h\hat{e}_1,t) - p(\vec{x},t)}{h}\right) \times \left(\frac{p(\vec{x}+h\hat{e}_2,t) - p(\vec{x},t)}{h}\right)\right\|^{-1} \tag{2}$$

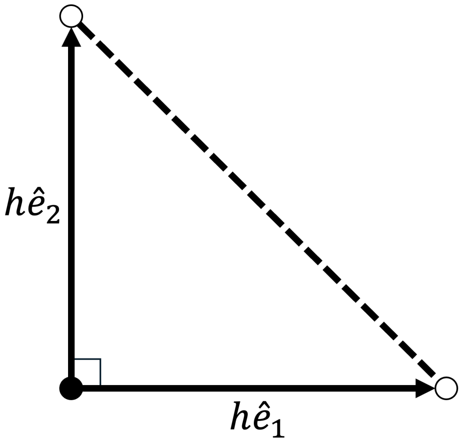

Figure 1. Diagram showing differential TCV formulation.

Taking the limit of this quantity as h approaches zero, and utilizing the definition of the partial derivative yields the differential form of the dilation factor:

$$f_D(t) = \left\| \frac{\partial p(\vec{x},t)}{\partial x_1} \times \frac{\partial p(\vec{x},t)}{\partial x_2} \right\|^{-1} . \tag{3}$$

Eqn. (3) states that the dilation factor is the inverse magnitude of the cross product of the partial derivatives of the location with respect to the two orthogonal vectors oriented to the freestream direction. Using this formulation, any quantity requiring spatial distribution of particles within a region of space such as number density, can be computed using a single particle trajectory. This technique is readily implemented with automatic differentiation, as the added complexity and computational cost are quite small. In addition to requiring a single particle trajectory to get number density-based information, a secondary benefit is that the order of accuracy of these quantities is determined by the numerical scheme used for particle tracing and any spatial interpolation scheme used to sample between particle trajectory positions.

REFERENCES

[1] Karl Hille. The fact and fiction of martian dust storms, 2023. URL https://www.nasa.gov/solar-system/the-fact-and-fiction-of-martian-dust-storms/.

[2] S. Hughes, F. Cheatwood, R. Dillman, H. Wright, J. DelCorso, and A. Calomino. Hypersonic inflatable aerodynamics decelerator (hiad) technology development overview. In *21st AIAA Aerodynamic Decelerator Systems Technology Conference and Overview*, Dublin, Ireland, May 2011. AIAA-2011-2524, https://doi.org/10.2514/6.2011-2524.

[3] T. Polsgrove and A. Dwyer-Cianciolo. Human mars entry, descent and landing architecture study overview. In *2016 AIAA Space Conference*, Long Beach, CA, September 2016. https://doi.org/10.2514/6.2016-5494.

[4] E. Venkatapathy, J. Arnold, I. Fernandez, K.R. Hamm, D. Kinney, B. Laub, A. Makino, M.K. McGuire, K. Peterson, D. Prabhu, D. Empey, I. Dupzyk, L. Huynh, P. Hajela, P. Gage, A.R. Howard, and D. Andrews. Adaptive deployable entry and placement technology (apept): A feasibility study for human missions to mars. In *21st AIAA Aerodynamic Decelerator Systems Technology Conference and Overview*, Dublin, Ireland, May 2011. AIAA-2011-2608, https://doi.org/10.5214/6.2011-2608.

[5] K.H. Peterson, B. Yount, N.R. Schneider, D.K. Prabhu, J.O. Arnold, T.H. Squire, P.F. Wercinski, J.F. Chavez-Garcia, and E. Venkatapathy. Thermal and structural performance of woven carbon cloth for adaptive deployable entry and placement technology. In *22nd AIAA Aerodynamic Decelerator Systems Conference*, Daytona Beach, FL, March 2013. AIAA-2013-1370, https://doi.org/10.2514/6.2013-1370.

[6] G.D. Waldmann and W.G. Reinecke. Particle trajectories, heating, and breakup in hypersonic shock layers. *AIAA Journal*, 9(6):1040–1048, 1971. https://doi.org/10.2514/3.6328.

[7] T.C. Lin and N.A. Thyson. Ice-crystal/shock-layer interaction in hypersonic flight. *AIAA Journal*, 15(10):1511–1514, 1977. https://doi.org/10.2514/3.7446.

[8] P. Papadopoulos, M. Tauber, and I. Chang. Heatshield erosion in a dusty martian atmosphere. *Journal of Spacecraft and Rockets*, 30(2):140–151, April 1993. https://doi.org/10.2514/3.11522.

[9] G. Palmer, Chen Y.K., P. Papadopoulos, and M. Tauber. Reassessment of effect of dust erosion on heatshield of mars entry vehicle. *Journal of Spacecraft and Rockets*, 37(6):747–752, December 2000. https://doi.org/10.2514/2.3646.

[10] G. Palmer, E. Ching, I. Matthias, Allofs D., and A. Gulhan. Modeling heat-shield erosion due to dust particle impacts for martian entries. *Journal of Spacecraft and Rockets*, 57(5):857–875, September 2020. https://doi.org/10.2514/1.A34744.

[11] E. Ching, M. Barnhardt, and M. Ihme. Sensitivity of hypersonic dusty flows to physical modeling of the particle phase. *Journal of Spacecraft and Rockets*, 58(3): 653–667, May 2021. https://doi.org/10.2514/1.A34810.

[12] M. Kroells, A. Sahai, and T. Schwartzentruber. Sensitivity study of dust-induced surface erosion during martian planetary entry. In *AIAA Scitech 2022 Forum*, 2022.

[13] A. Sahai and G. Palmer. Variable-fidelity euler-lagrange framework for simulating particle-laden high-speed flows. *AIAA Journal*, 2022.

[14] M. Mirzaei, A. Shadaram, and M. Shahyar. Numerical simulation of supersonic gas-particle flow using eulerian-eulerian approach. In *14th AIAA/AHI Space Planes and Hypersonic Systems and Technology Conference*, 2006. AIAA 2006-7944, https://doi.org/10.2514/6.2006-7944.

[15] M.F. Modest and S. Mazumder. *Radiative Heat Transfer*. Academic Press, San Diego, CA, 4^{th} edition, 2022.

[16] J.R. Howell, M.P. Menguc, and R. Siegel. *Thermal Radiative Heat Transfer*. CRC Press, Boca Raton, FL, 6^{th} edition, 2015.

[17] L. Dombrovsky, D. Reviznikov, and A. Sposobin. Radiative heat transfer from supersonic flow with suspended particles to a blunt body. *International Journal of Heat and Mass Transfer*, 93:853–861, 2016.

[18] B. Wang and I. Glass. Compressible laminar boundary-layer flows of a dusty gas over a semi-infinite flat plate. *Journal of Fluid Mechanics*, 186:223–241, 1988.

[19] G. Ben-Dor and O. Igra. The effect of dust and water drops on the flow field behind strong normal blast waves. Technical Report ADA148304, U.S. Army, 1983.

[20] R. Padmapriya and K. Reddy. Numerical analysis of dusty hypersonic viscous gas flow over a flat plate. *AIAA Journal*, 39:1313–1319, 2001.

[21] T. Anderson and R. Jackson. Fluid mechanical description of fluidized beds. equations of motion. *Industrial & Engineering Chemistry Fundamentals*, 6(4):527–539, 1967. URL https://doi.org/10.1021/i160024a007.

[22] G. Shallcross, R. Fox, and J. Capecelatro. A volume-filtered description of compressible particle-laden flows. *International Journal of Multiphase Flow*, 122, 2020.

[23] A. Morris, D. Goldstein, P. Varghese, and L. Trafton. Lunar dust transport resulting from single- and four-engine plume impingement. *AIAA Journal*, 54(4), 2016.

[24] M. Gallis, J. Torczynski, and D. Rader. An approach for simulating the transport of spherical particles in a rarefied gas flow via the direct simulation monte carlo method. *Physics of Fluids*, 13(11), 2001.

[25] J. Burt and I. Boyd. Development of a two-way coupled model for two phase rarefied flows. In *42nd AIAA Aerospace Sciences Meeting and Exhibit*, 2004. AIAA-2004-1351.

[26] E. Loth. Compressibility and rarefaction effects on drag of a spherical particle. *AIAA Journal*, 46(9):2219–2228, 2008.

[27] E. Loth, J. Daspit, M. Jeong, T. Nagata, and T. Nonomura. Supersonic and hypersonic drag coefficients for a sphere. *AIAA Journal*, 2021.

[28] J.D. Anderson. *Computational Fluid Dynamics: The Basics With Applications*. McGraw-Hill Education, New York, NY, 1995.

[29] R. Davuluri, H. Zhang, and A. Martin. Numerical study of spallation phenomenon in an arc-jet environment. *Journal of Thermophysics and Heat Transfer*, 30:32–41, 2016.

[30] J. Capecelatro. Modeling high-speed gas-particle flows relevant to spacecraft landings: A review and perspectives.

[31] C.B. Henderson. Drag coefficients of spheres in continuum and rarefied flows. *AIAA Journal*, 14(6):707–708, June 1976. https://doi.org/10.2514/3.61409.

[32] A. Majid, U. Bauder, G. Herdich, and M. Fertig. Two-phase flow solver for hypersonic entry flows in a dusty martian atmosphere. *Journal of Thermophysics and Heat Transfer*, 30(2):418–428, June 2016. https://doi.org/10.2514/1.T4542.

[33] T.W. Fox, C.W. Rackett, and J.A. icholls. Shock wave ignition of magnesium powders. In *Proceedings of the 11th International Symposium on Shock Tubes and Shock Waves*. University of Washington Press, 1977.

[34] P. Gnoffo, R. Gupta, and J. Shinn. Conservation equations and physical models for hypersonic air flows in thermal and chemical nonequilibrium. Technical Report 19890006744, NASA, February 1989.

[35] A. Hinkle, S. Hosder, and C. Johnston. Efficient solution of surface erosion in particle-laden hypersonic flows. *Journal of Spacecraft and Rockets*, 59(6):2114–2128, 2022. https://doi.org/10.2514/1.A35331.

[36] L. Shaefer and B. Fegley. A thermodynamic model of high temperature lava vaporization on io. *Icarus*, 169:216–241, 2004. https://doi.org/10.1016/j.icarus.2003.08.023.

[37] J. Lane, B. Magedson, and M. Rarick. An efficient point in polyhedron algorithm. *Computer Vision, Graphics, and Image Processing*, 26:118–125, 1984.

[38] A. Allievi and R. Bermejo. A generalized particle search–locate algorithm for arbitrary grids. *Journal of Computational Physics*, 132(2):157–166, 1997. doi: https://doi.org/10.1006/jcph.1996.5604.

[39] D. Yoder. Trilinear interpolation, 2003. URL https://www.grc.nasa.gov/WWW/winddocs/utilities/b4wind_guide/trilinear.html.

[40] E. Ching, S. Brill, M. Barnhardt, and M. Ihme. A two-way coupled euler-lagrange method for simulating multiphase flows with discontinuous galerkin schemes on arbitrary curved elements. *Journal of Computational Physics*, 405, 2020.

[41] S. Hosder, R. Walters, and M. Balch. Efficient sampling for non-intrusive polynomial chaos applications with multiple uncertain input variables. In *48th AIAA/ASME/ASCE/AHS/ASC Structures, Structural Dynamics, and Materials Conference*, number AIAA 2007-1939, Honolulu, HI, April 2007. https://doi.org/10.2514/6.2007-1939.

[42] G.A. Ruff and B.M. Berkowitz. Users manual for the nasa lewis ice accretion prediction code (lewice). Technical Report CR-185129, NASA, 1990.

[43] J. Monaghan. Smoothed particle hydrodynamics. *Annual Review of Astronomy and Astrophysics*, 30:543–574, 1992. https://doi.org/10.1146/annurev.aa.30.090192.002551.

[44] D. Wilcox. *Basic Fluid Mechanics*. DCW Industries, La Canada, CA, 2013.

[45] B. Delaunay. Sur la sphere vide. *Bulletin de l'Academie des Sciences de I'URSS, Classe des Sciences Mathematiques et Naturelles*, 6:793–800, 1934.

[46] A. Hinkle, S. Hosders, and C. Johnston. Efficient solution of surface erosion in particle-laden hypersonic flows. In *Ascend 2021*, number AIAA-2021-4229, Las Vegas, NV, 2021. https://doi.org/10.2514/6.2021-4229.

[47] W. Heidrich. Computing the barycentric coordinates of a projected point. *Journal of Graphics Tools*, 10(3):9–12, 2005. https://doi.org/10.1080/2151237X.2005.10129200.

[48] Pauli Virtanen, Ralf Gommers, Travis E. Oliphant, Matt Haberland, Tyler Reddy, David Cournapeau, Evgeni Burovski, Pearu Peterson, Warren Weckesser, Jonathan Bright, Stéfan J. van der Walt, Matthew Brett, Joshua Wilson, K. Jarrod Millman, Nikolay Mayorov, Andrew R. J. Nelson, Eric Jones, Robert Kern, Eric Larson, C J Carey, İlhan Polat, Yu Feng, Eric W. Moore, Jake VanderPlas, Denis Laxalde, Josef Perktold, Robert Cimrman, Ian Henriksen, E. A. Quintero, Charles R. Harris, Anne M. Archibald, Antônio H. Ribeiro, Fabian Pedregosa, Paul van Mulbregt, and SciPy 1.0 Contributors. SciPy 1.0: Fundamental Algorithms for Scientific Computing in Python. *Nature Methods*, 17:261–272, 2020. doi: 10.1038/s41592-019-0686-2.

[49] C.T. Crowe. Vapor-droplet flow equations. Technical Report UCRL-51877, Lawrence Livermore Laboratory, Livermore, CA, 1975.

[50] O. Ejtehadi, R. Mahravan, and I. Sohn. Investigation of shock and a dust cloud interaction in eulerian framework using a newly developed openfoam solver. *International Journal of Multiphase Flow*, 145, 2021.

[51] B. Tian, E.F. Toro, and C.E. Castro. A path-conservative method for a five-equation model of two-phase flow with an hllc-type riemann solver. *Computers & Fluids*, 46: 122–132, 2011.

[52] S. K. Jung and R. S. Myong. A second-order positivity-preserving finite volume upwind scheme for air-mixed droplet flow in atmospheric icing. *Computers and Fluids*, 86(5):459–469, 2013.

[53] E. Masi, O. Simonin, and B. Bedat. The mesoscopic eulerian approach for evaporating droplets interacting with turbulent flows. *Flow, Turbulence and Combustion*, 86:563–583, 2011.

[54] K. Thompson, H. Nishikawa, and E. Padway. Economical third-order methods for accurate surface heating predictions on simplex element meshes. In *AIAA SciTech Forum*, National Harbor, MD, 2023.

[55] K.B. Thompson and M.D. O'Connell. Streamlined convergence acceleration for cfd codes. In *AIAA Aviation Forum*, 2019. AIAA 2019-3709.

[56] A. Harten. High resolution schemes for hyperbolic conservation laws. *Journal of Computational Physics*, 49:357–393, 1983.

[57] K. Perlin. Improving noise. *ACM Transactions on Graphics*, 21:681–682, 2002. doi: https://doi.org/10.1145/566654.566636.

[58] R.N. Gupta, J.M. Yos, R.A. Thompson, and K. Lee. A review of reaction rates and thermodynamic and transport properties for an 11-species air model for chemical and thermal nonequilibrium calculations to 30000 k. Technical Report RP-1232, NASA, 1990.

[59] C. Johnston, T. K. West, and A. M. Brandis. Features of afterbody radiative heating for titan entry. In *AIAA Aviation*, Dallas, TX, 2019.

[60] O.B Toon, J.B. Pollack, and C. Sagan. Physical properties of the particles composing the martian dust storm of 1971-1972. *Icarus*, 30:663–696, 1977. https://doi.org/10.1016/0019-1035(77)90088-4.

[61] M. Querry. Optical constants of minerals and other materials from the millimeter to the ultraviolet. Technical Report CRDEC-CR-88009, U.S. Army Armament Munitions Chemical Command, Chemical Research, Development & Engineering Center, Aberdeen Proving Ground, MD, 1987.

[62] Y. Zel'dovich and Y. Raizer. *Physics of Shock Waves and High-Temperature Hydrodynamic Phenomena*. Dover Publications, Inc., Mineola, NY, 2002.

[63] G. Mie. Contributions on the optics of turbid media, particularly colloidal metal solutions. techreport SAND78-6018, Sandia National Laboraties, July 1978. Translated from 'Annalen der Physik, Series IV, V. 25 (1908) p. 377-445', German.

[64] C. Bohren and D. Huffman. *Absorption and Scattering of Light by Small Particles*. John Wiley & Sons, Ltd, 1998.

[65] C. Johnston and A. Mazaheri. Impact of non-tangent-slab radiative transport on flowfield-radiation coupling. *Journal of Spacecraft and Rockets*, 55(4):899–913, 2018.

[66] J. Bonet and J. Peraire. An alternating digital tree (adt) algorithm for 3d geometric searching and intersection problems. *International Journal for Numerical Methods in Engineering*, 31:1–17, 1991.

[67] A. Mazaheri, C. Johnston, and S. Sefidbakht. Three-dimensional radiation ray-tracing for shock-layer radiative heating simulations. *Journal of Spacecraft and Rockets*, 50 (3):485–493, 2013.

[68] J.C. Chai, H.S. Lee, and S.V. Patankar. Finite volume method for radiation heat transfer. *Journal of Thermophysics and Heat Transfer*, 8(3):419–425, 1994.

[69] D.A. Andrienko and S.T. Surzhikov. P1 approximation applied to the radiative heating of descent spacecraft. *Journal of Spacecraft and Rockets*, 49(6):1088–1098, 2012.

[70] L.C. Hartung and H.A. Hassan. Radiation transport around axisymmetric blunt body vehicles using a modified differential approximation. In *30th Aerospace Sciences Meeting*, 1992. AIAA 92-0119.

[71] R.W. Barnwell. Inviscid radiation shock layers about spheres traveling at hyperbolic speeds in air. Technical Report TR R-311, NASA, 1969.

[72] Chambers L. Predicting radiative heat transfer in thermochemical nonequilibrium flow fields: Theory and user's manual for the loran code. Technical Report TM 4564, NASA, 1994.

[73] T.K. West and C.O. Johnston. Assessment of mars 2020 forebody heating predictions with coupled material response. In *AIAA SciTech 2023 Forum*, 2023. AIAA 2023-0962.

[74] C.O. Johnston, B.R. Hollis, and K. Sutton. Spectrum modeling for air shock-layer radiation at lunar-return conditions. *Journal of Spacecraft and Rockets*, 45(5), 2008.

[75] A. Gulhan, T. Thiele, F. Siebe, R. Kronen, and T. Schlueutker. Aerothermal measurements from the exomars schiaparelli capsule entry. *Journal of Spacecraft and Rockets*, 56(1):68–81, February 2019. https://doi.org/10.2514/1.A34228.

[76] New mexico state university planetray data system, mars reconnaissance orbiter archive, 2021. URL https://atmos.nmsu.edu/data_and_services/atmospheres_data/MARS/aerosols.html.

[77] G. Palmer. Private communication, April 2022.

[78] K. Thompson, B. Hollis, C. Johnston, B. Kleb, Lessard V., and Mazaheri A. Laura users manual: 5.6. Technical Report TM 2020-220566, NASA, 2020.

[79] I.S. Gradshteyn and I.M. Ryzhik. *Table of Integrals, Series, and Products*. Elsevier, 8 edition, 2014.

[80] M. Tomasko, L. Doose, M. Lemmon, P. Smith, and E. Wegryn. Properties of dust in the martian atmosphere from the imager on mars pathfinder. *Journal of Geophysical Research*, 104(E4):8987–9007, 1999.

[81] K. Keller, P. Lindenmaier, E. K. Pfeiffer, B. Esser, A. Gulhan, L. Marraffa, P. Omaly, and M.C. Desjean. Dust particle erosion during mars entry. In *40th International Conference on Environmental Systems*, 2010.

[82] A. Brune, S. Hosder, K. Edquist, and S. Tobin. Thermal protection system response uncertainty of a hypersonic inflatable aerodynamic decelerator. *Journal of Spacecraft and Rockets*, 54(1):141–154, 2017. https://doi.org/10.2514/1.A33732.

[83] T. West and S. Hosder. Uncertainty quantification of hypersonic reentry flows with sparse sampling and stochastic expansions. *Journal of Spacecraft and Rockets*, 52 (2):120–133, 2015. https://doi.org/10.2514/1.A32947.

[84] T. West, C. Johnston, and S. Hosders. Uncertainty and sensitivity analysis of afterbody radiative heating predictions for earth entry. *Journal of Thermophysics and Heat Transfer*, 31(2):294–306, 2017. https://doi.org/10.2514/1.T4948.

[85] A. Vuruskan and S. Hosder. Impact of turbulence models and shape parameterization on robust aerodynamic shape optimization. *AIAA Journal of Aircraft*, 56(3):1099–1115, June 2019. https://doi.org/10.2514/1.C035039.

[86] I. Sobol. Sensitivity analysis for non-linear mathematical models. *Mathematical Modeling & Computational Experiment*, 1:407–414, 1993. Translated from 'Matematicheskoe Modelirovanie, Vo. 2, p.112-118', Russian.

[87] M. Di Stefano, S. Hosders, and R. A. Baurle. Effect of turbulence model uncertainty on scramjet strut injector flow field analysis. *Computers and Fluids*, 229, October 2021. https://doi.org/10.1016/j.compfluid.2021.105104.

[88] J. H. Halton. Algorithm 247: Radical-inverse quasi-random point sequence. *Commun. ACM*, 7(12):701–702, 1964. doi: 10.1145/355588.365104. https://doi.org/10.1145/355588.365104.

[89] M. Alexander. Mars transportation environement definition document. techreport 2001-210935, NASA Marshall Space Flight Center, Alabama, March 2001.

[90] F. Billig. Shock-wave shapes around spherical- and cylindrical-nosed bodies. *Journal of Spacecraft and Rockets*, 4:822–823, 1967.

[91] J.D. Anderson. *Modern Compressible Flow: With Historical Perspective*. Aeronautical and Aerospace Engineering Series. McGraw-Hill Education, 2003. ISBN 9780072424430.

[92] C. Rumsey. Nasa langley turbulence modeling resource. https://turbmodels.larc.nasa.gov/flatplate.html, Mar 2021. Accessed on 5/3/2022.

[93] P. Roache. Perspective: A method for uniform reporting of grid refinement studies. *Journal of Fluids Engineering*, 116:405–413, Sep 1994.

[94] E. Vasilevskii and A. Osiptsov. Heat exchange on the front surface of a blunt body in a high-speed flow containing low-inertia particles. *Journal of Engineering Physics and Thermophysics*, 74(6):1399–1411, 2001.

[95] E. Ching and M. Ihme. Discontinuous galerkin simulations of dusty flows over a full-scale capsule during mars atmospheric entry. In *AIAA Scitech 2021 Forum*, number AIAA-2021-1518, 2021. https://doi.org/10.2514/6.2021-1518.

[96] P. Lavvas, R. V. Yelle, and C. A. Griffith. Titan's vertical aerosol structure at the huygens landing site: Constraints on particle size, density, charge, and refractive index. *Icarus*, 210:832–842, 2010.

[97] C. McKay. Elemental composition, solubility, and optical properties of titan's organic haze. *Planetary and Space Science*, 44(8):741–747, 1995.

[98] S. Catris and B. Aupoix. Density corrections for turbulence models. *Aerospace Science and Technology*, 4:1–11, 2000.

[99] Weisstein. Laguerre-gauss quadrature, 2024. URL https://mathworld.wolfram.com/Laguerre-GaussQuadrature.html.

[100] W. Zhao, Z. Sun, and Z. Alwahabi. Emissivity and absorption function measurements of al2o3 and sic particles at elevated temperature for the utilization in concentrated solar receivers. *Solar Energy*, 207:183–191, 2020.

[101] J. Kalman, N. Glumac, and H. Krier. High-temperature metal oxide spectralemissivities for pyrometry applications. *Journal of Thermophysics and Heat Transfer*, 29 (4):874–879, 2015.

[102] P. Ramsey and J. E. Lyne. Investigation of titan aerogravity assist for capture into orbit about saturn. *Journal of Spacecraft and Rockets*, 43(1):231–233, 2006.

[103] H. Nelson. Feasibility of determining haze properties during high-speed titan entry. *Journal of Thermophysics and Heat Transfer*, 8(3), 1994.

VITA

Andrew Dale Hinkle was born in St. Louis, MO. After graduating from Jackson High School in Jackson, MO in 2009, he began his undergraduate education in engineering technology at Southeast Missouri State University. Upon graduating in 2014 with a Bachelor of Science degree in Engineering Technology, he began his professional career in automotive plastics with Toyoda Gosei North America Corporation. In 2016, Andrew continued his education at Missouri University of Science and Technology. Over the course of his time as an undergraduate at Missouri University of Science and Technology, Andrew completed internships at NASA Langley Research Center in 2018 and 2019. In 2018, he graduated Summa Cum Laude earning a Bachelor of Science degree in Aerospace Engineering. Andrew was then selected for the NASA Space Technology Research Fellowship in 2019. In May 2024 he received his Ph.D. degree in Aerospace Engineering from Missouri University of Science and Technology. Andrew began his career as a Research Aerospace Engineer at NASA Langley Research Center in 2023.